LBL--28170

DE90 007348

MAGNETIC PROPERTIES OF SURFACES AND INTERFACES*

D. C. Chrzan

Department of Physics, University of California, Berkeley,

and

Materials and Chemical Sciences Division,
Lawrence Berkeley Laboratory,
Berkeley, CA 94720

November 1989

*This work was supported in part by the Director, Office of Energy Research, Office of Basic Energy Sciences, Materials Sciences Division of the U. S. Department of Energy under Contract No. DE-AC03-76SF00098.

Magnetic Properties of Surfaces and Interfaces

Daryl C. Chrzan

Abstract

A survey of the magnetic properties of three types of planar defects is presented: a model interface in an Ising antiferromagnet, a model of the surface of an antiferromagnet, and a realistic calculation of the magnetic properties of stacking defects in a bulk ferromagnet. The simplest interface studied is the antiphase boundary in the nearest-neighbor face-centered-cubic Ising antiferromagnet. The properties of this defect are understood by means of the construction and solution of an exactly solvable thermodynamic model which mimics the boundary's properties. The implications for further calculations using the nearest-neighbor face-centered-cubic Ising model are explored. This thesis then examines the effects of introducing a free surface in a real antiferromagnetic semiconductor, EuTe. The complex magnetic structures of the {001} faces of this material, which include spin structures incommensurable with the underlying lattice, are understood in terms of a classical Heisenberg Hamiltonian. Finally, the magnetic properties of {111} stacking faults in nickel are investigated utilizing a self-consistent, layered Korringa-Kohn-Rostoker formalism based on the local-density approximation to density-functional theory. Very simple expressions for the spin polarization and internal energy are developed. The range of behaviors displayed by these three systems is remarkable in its diversity, and yet the underlying mechanisms are all similar. This similarity suggests that many of the tools necessary for understanding the magnetic properties of surfaces and interfaces are readily available.

Table of Contents

Acknowledgements

It is difficult to explicitly acknowledge all the people who have contributed to this thesis. To those who should be mentioned below, but are not, I extend my sincerest gratitude.

I thank my advisor, Professor Leo Falicov, for his guidance, patience, and friendship over these past few years. Working with him has been most enjoyable and rewarding from both a professional and a human perspective.

I thank the other members of the Falicov group, Dr. Ariel Reich, Jim Freericks, Dr. Henrik Svensmark, Amitesh Maiti and Dr. Andreas Giesekus, who provided the stimulating and enjoyable atmosphere in which this research was completed.

I thank Michael Surh, Xuejun Zhu, and the rest of the condensed matter theory group at Berkeley.

Thanks also goes to Dr. James MacLaren, Dr. Antonios Gonis, and Dr. X.-G. Zhang for the computer codes used to conduct the research in chapter IV, and for their insightful and enlightening collaboration.

I thank my parents, who taught me the value and excitement of learning.

Finally, I thank my wife, Julie, whose patience, companionship and love during these graduate school years made the whole experience truly wonderful.

This thesis is dedicated to my wife,
Julie.

Chapter I: Introduction

The properties of magnetic materials have been the subject of study and wonder for over a thousand years.[1] The lodestone appeared in Greek writings about 800 B.C., and the compass was certainly introduced into Europe by the twelfth century A.D. Magnetism was applied technologically long before its underlying mechanism was understood as it took until the twentieth century and the advent of quantum mechanics for the physics to begin to be unraveled. Even today, the complete characterization and understanding of magnetism and related phenomena remains as one of the great challenges to scientists.

The special class of systems studied here consists of planar defects: surfaces, interfaces and antiphase boundaries. While it is important to understand the bulk properties of magnetic materials, it is equally important to understand the effects of planar defects. Many important magnetic devices (e.g. computer disk drives) directly involve surfaces and interfaces of magnetic materials.

The study of planar defects performs another vital function. If a theory, based on experiments which measure bulk properties, accurately reproduces the experimentally observed surface or interface properties, it is highly probable, that the theory is correct. Alternatively, failure to reproduce the observed planar defect behavior suggests an incorrect or incomplete theory. The information gained from this failure generally leads to improvements in the theory of the bulk properties.

Before delving into the details of these defects and their magnetic properties, it is necessary to present a brief introduction to the field of magnetism. There are two important aspects of the magnetism problem: the physical interaction which leads to ferromagnetism or antiferromagnetism, and the thermodynamic properties of magnetic systems. While these aspects are not truly separable, both are sufficiently complex that studies of real systems are often simplified by handling each aspect separately. When appropriate, this thesis will do so as well.

A. Physical Origins of Magnetism

Dirac[2] and Heisenberg[3] independently discovered exchange, the interaction leading to magnetism, in 1926. They argued that because the Pauli exclusion principle keeps two electrons with the same spin spatially separated, the parallel-spin configuration has a lower Coulomb energy than that of electrons in different spin states. At the same time, however, the electrons must have a higher kinetic energy (correlations between electrons must induce more nodes in the wavefunction). In most cases, this increase in kinetic energy outweighs the decrease in Coulomb energy, and the system does not become ferromagnetic. In special circumstances the reverse is true, which results in ferromagnetism. Ferromagnetism originates in the Coulomb force, not the much weaker magnetic dipole-dipole interaction of classical physics and, being an inherently quantum mechanical phenomena, would vanish if $\hbar$ were zero.

The variation in observed magnetic behaviors is noteworthy. The $3d$ transition metals Ni, Co and Fe all display ferromagnetism. The ground state of Cr is an antiferromagnetic spin-density wave. The insulators NiO and MnO are antiferromagnets. The rare-earth metals and their alloys have even more complicated magnetic properties. For example, EuO and EuS are two of the very rare insulating ferromagnets, EuSe is both a ferromagnet and an antiferromagnet (depending on the temperature), and EuTe is antiferromagnetic.

One fundamental process underlies these phenomena, all of which can be understood as manifestations of the various aspects of exchange. The simple model Hamiltonian described below, which explicitly includes exchange, demonstrates this fact. It will allow for the description of magnetic phenomena in the transition metals, the transition-metal compounds and alloys, and the rare-earth metals, compounds and alloys.

Consider a one-electron Hamiltonian defined on a Bravais lattice:

$$H^o = \sum_{i,j} \sum_{\sigma} \sum_{n} t_{ijn} c^{\dagger}_{in\sigma} c_{jn\sigma}$$

where the operator $c^{\dagger}_{in\sigma}$ ($c_{in\sigma}$) creates (destroys) an electron with spin σ in the nth Wannier orbital[4] at site i. The matrix element of the one-particle Hamiltonian, t_{ijn}, includes the kinetic energy and the average effects of the nuclei and all the other electrons. The inclusion of the average effects of all the other electrons results in a self-consistently renormalized band structure.

To study magnetism, however, it is advantageous to calculate some of these averaged terms explicitly, and not include their effects in the renormalized band structure. Doing so may artificially enhance the magnetism of the Hamiltonian, but the Hamiltonian should be a good first approximation to the real system.

The first term singled out for explicit treatment is the direct Coulomb interaction between two electrons, which has the following form:

$$H^c = (1/2) \sum_{i,j} \sum_{n,n'} \sum_{\sigma,\sigma'} V^c_{in,jn'} \, n_{in\sigma} \, n_{jn'\sigma'}$$

where $n_{in\sigma}$ is the number of electrons on site i in the nth Wannier orbital with spin σ, and V^c is the Coulomb-interaction matrix element.

The exchange terms, also treated explicitly, act as a correction to the Coulomb repulsion for two electrons in a triplet state and lowers their energy relative to the singlet state. In this interaction, an electron at site one scatters, via the Coulomb interaction, with an electron at site two, and in the final state the first electron is at site two and the second electron is at site one. The spins do not flip in this process. The Hamiltonian corresponding to this interaction is

$$H^{ex} = \sum_{i,j} \sum_{n,n'} \sum_{\sigma,\sigma'} V^{ex}_{in,jn'} \, c^{\dagger}_{jn'\sigma} \, c^{\dagger}_{in\sigma'} \, c_{jn'\sigma'} \, c_{in\sigma}$$

where

$$V^{ex}_{in,jn'} = 1/2 \int d\mathbf{r} \int d\mathbf{r}' \, \psi^*_{nj}(\mathbf{r}') \, \psi_{n'i}(\mathbf{r}') \, \frac{e^2}{|\mathbf{r} - \mathbf{r}'|} \, \psi^*_{n'i}(\mathbf{r}) \, \psi_{nj}(\mathbf{r}) \quad .$$

H^{ex} can be recast in terms of the number operators, $\mathbf{n}$, and the spin operators, $\mathbf{S}$, by writing out the sum over the spins explicitly and noting that

$$\mathbf{S}^z_{i,n} = 1/2 \, (\mathbf{n}_{in\uparrow} - \mathbf{n}_{in\downarrow}),$$

$$\mathbf{S}^+_{i,n} = \mathbf{c}^\dagger_{in\uparrow} \mathbf{c}_{in\downarrow}$$

and

$$\mathbf{S}^-_{i,n} = \mathbf{c}^\dagger_{in\downarrow} \mathbf{c}_{in\uparrow} \quad .$$

Then

$$H^{ex} = - \sum_{i,j} \sum_{n,n'} J^{nn'}_{ij} \, [\mathbf{S}_{jn'} \cdot \mathbf{S}_{in} + 1/4 \, \mathbf{n}_{jn'} \mathbf{n}_{in}]$$

(Here, the exchange interaction is $J^{nn'}_{ij} = 2 \, V^{ex}_{in,jn'}$.) This form explicitly displays the spin dependence of the Coulomb interaction. The $\mathbf{n}_{in}$ in the last term of this expression is the total occupation, for both up and down spins, of the nth Wannier orbital on the ith site.

For insulators, with more than one orbital per site, the Coulomb term, H^c, and the intra-site exchange (responsible, in atomic physics, for Hund's rules) are the largest terms in the Hamiltonian. Calculations, then, treat these terms exactly; the inter-site exchange and the the hopping terms (H^o minus the effects of the Coulomb term and the exchange terms) are treated using perturbation theory. This approach yields the simple Heisenberg Hamiltonian

$$H^{Heis.} = - \sum_{i,j} J^{eff}_{ij} \, \mathbf{S}_i \cdot \mathbf{S}_j$$

where J^{eff}_{ij} is the effective exchange constant for the interaction between sites i and j

and can have either sign: a positive sign gives a ferromagnetic interaction, a negative sign results in antiferromagnetism. The S_i are the site spin operators, not the spin of a single electron, a feature arising directly from the intra-site Hund's rule coupling.

The Heisenberg Hamiltonian forms the foundation of the modern theory of local-moment magnetism. It has been used with remarkable success to study a variety of systems. The range of behaviors described by this Hamiltonian includes ferromagnetism, antiferromagnetism, and helical or more complicated structures.

In the Heisenberg Hamiltonian, the magnetic electrons are all localized. A wealth of evidence, however, indicates that itinerant, not localized, electrons are responsible for magnetism in the 3*d* transition metals. Perhaps the strongest of the arguments is that the number of Bohr magnetons observed in these systems is generally a non-integer (e.g. Ni is observed to have a moment of 0.606 μ_B, Fe a moment of 2.22 μ_B, and Co a moment of 1.71 μ_B)[5]. The Heisenberg Hamiltonian does not describe itinerant magnetism.

As a first attempt at understanding itinerant ferromagnetism, one can imagine the gradual delocalization of the localized magnetic electrons. It does not seem likely that a small amount of delocalization would destroy the magnetism. The Hamiltonian, $H^o + H^c + H^{ex}$, where H^o no longer contains the averaged effects of the direct Coulomb interaction or the exchange contained in H^{ex}, can still be used to understand these materials, but some modifications must be made. This thesis, however, approaches itinerant magnetism from a different viewpoint.

Since the magnetic electrons are delocalized, the Bloch states of the crystal form a better basis for understanding itinerant magnetism. The following analysis uses the techniques of first quantization; in this form they are applied below to study stacking faults in nickel.

The study of itinerant magnetism begins with the single particle Hamiltonian

$$H_i = -\nabla_i^2 + V(\mathbf{r}_i) + \sum_{j(j\neq i)} \frac{e^2}{|\mathbf{r}_i - \mathbf{r}_j|} \quad .$$

The first two terms are the kinetic energy of the electrons and the potential arising from the ions, respectively. The last term is the pairwise Coulomb interaction (the sum runs over all but the ith electron). Summing over all electrons gives the total Hamiltonian:

$$H = \sum_i H_i - (1/2) \sum_{j,i\ (j\neq i)} \frac{e^2}{|\mathbf{r}_i - \mathbf{r}_j|}$$

(the second term corrects for the double counting of the Coulomb interaction).

In the Hartree-Fock[6] approach, a determinantal product of wavefunctions which are the solution to self-consistent, one-particle-like eigenfunction eigenvalue equation approximates the true solution. The determinantal form insures compatibility with the Pauli exclusion principle. The resulting equations must be solved self-consistently; but the solution includes two types of terms, generally called the direct Coulomb interaction and the exchange interaction.

Unfortunately, the Hartree-Fock solution does not represent the physical situation very well. While explicitly including correlations between spin-aligned electrons by means of the antisymmetrization of the trial wavefunction, the approximation completely neglects correlations between electrons of opposite spin. This neglect leads to an overestimate of the energy of the system, because of the excess Coulomb energy of the uncorrelated electrons. In general, correlating electrons with opposite spin significantly decreases the potential energy of the system, which more than compensates the induced increase in kinetic energy. The difference in energy between the Hartree-Fock approximate energy and the true energy is referred to as the correlation energy.

The shortcomings of the Hartree-Fock solution motivate improvements. Most

commonly, theorists add an extra term representing the exchange and correlation energy to the single-particle Hamiltonian. Slater[7] suggested a term proportional to $\rho(\mathbf{r})^{1/3}$, where $\rho(\mathbf{r})$ is the density of electrons at the point $\mathbf{r}$. In the Hartree-Fock approximation, electrons of the same spin are more separated than electrons of opposite spin, essentially enhancing the repulsion between electrons of the same spin. This enhanced repulsion creates an "exchange-hole" in the density of electrons of the same spin; the deficiency in charge amounts to exactly one electron. The radius of the "exchange-hole" must be on the order of $\rho(\mathbf{r})^{-1/3}$, suggesting that the electrons on the outer edge of the hole feel a potential proportional to $\rho(\mathbf{r})^{1/3}$.

In 1964, Hohenberg and Kohn[8] developed density-functional theory, which justified Slater's methodology, but modified his exchange potential. Hohenberg and Kohn established that the ground-state energy of an electronic system is a unique functional of the electron density. The variational equation describing this dependence is

$$E[\rho(\mathbf{r})] = T[\rho(\mathbf{r})] + e \int \rho(\mathbf{r})\, V(\mathbf{r})\, d^3r$$

$$+ \frac{e^2}{2} \int\int \frac{\rho(\mathbf{r})\, \rho(\mathbf{r}')}{|\mathbf{r} - \mathbf{r}'|} d^3r' d^3r + E_{xc}[\rho(\mathbf{r})] \quad ,$$

where $T[\rho(\mathbf{r})]$ is the kinetic energy associated with the electrons, $V(\mathbf{r})$ the external potential (i.e. arising from the ions in the lattice), the third term represents the electrostatic energy of the electrons, and the fourth term is the exchange-correlation energy functional. The true density of the system is obtained by varying the energy with respect to the electron density with the number of electrons constrained to take the proper value.

The non-local theory described above depends in a complicated way on the electron densities at points $\mathbf{r}$ and $\mathbf{r}'$, making its application very difficult. The simplification most often applied was developed by Kohn and Sham[9,10] and is referred to as the local-density approximation. In this approximation, the exchange-correlation

energy of free-electron gas of density $\rho(\mathbf{r})$ replaces the nonlocal exchange-correlation energy functional. Furthermore, the density, $\rho(\mathbf{r})$, is written as

$$\rho(\mathbf{r}) = \sum_{i}^{N} \psi_i^*(\mathbf{r})\, \psi_i(\mathbf{r}) \quad ,$$

with N, the number of electrons in the system, and $\psi_i(\mathbf{r})$, a single-particle wavefunction.

These assumptions reduce the calculation to the self-consistent solution of a set of one-particle equations:

$$[-\nabla^2 + V(\mathbf{r}) + e^2 \int \frac{\rho(\mathbf{r}')}{|\mathbf{r} - \mathbf{r}'|} d^3r' + V_{xc}(\mathbf{r})]\, \psi_i(\mathbf{r}) = \varepsilon_i\, \psi_i(\mathbf{r})$$

where $V_{xc}(\mathbf{r})$ is the exchange-correlation potential defined as the variational derivative, $\delta E_{xc}/\delta\rho(\mathbf{r})$.

The original formulation of the local-density-approximation to density-functional theory applied to spinless electrons. The formulation was later extended to electrons with spin, which allowed the investigation of magnetic systems.[11] The extension, however, was a non-trivial task, complicated by the fact that a spin density does not uniquely determine a spin-dependent potential. Hohenberg and Kohn's density-functional theory insures, however, that there is still a unique spin density for the ground state. A parametrized form of the exchange-correlation energy facilitates self-consistent band-structure calculations; the calculations below employ a spin-polarized form of the parametrization developed by Hedin and Lundqvist.[12]

In general, the results of local-spin-density-functional theory do not agree with experiment as well as one would like. For example, the experimentally measured 3-*d* bandwidth of nickel is one electron-Volt narrower than the calculated bandwidth. Furthermore, self-consistent local-spin-density-functional methods predict too large an exchange splitting.[13]

The issue is, then, whether or not local-spin-density-functional theory can predict the true behavior of the spin polarization of stacking faults in nickel. While a proof that this may be the case is not available, there are some indications that the local theory does work. For example, it predicts a spin polarization of 0.58 μ_B for nickel, and a spin polarization of 2.15 μ_B for iron.[13] The experimentally determined values are 0.56 μ_B and 2.12 μ_B, respectively. This agreement between the theory and the experiments suggests that the local approximation adequately represents the physical mechanism responsible for the magnitude of the spin polarization in nickel. Furthermore, the stacking-fault studies presented here are aimed at understanding trends of the spin polarization near a stacking fault. In that respect, the absolute values of the spin polarization are not very important, only variations in spin polarization matter. Systematic errors in the calculations may cancel, and the trends may be accurately predicted.

B. Thermodynamic Aspects of Magnetism

The most striking feature of the three-dimensional magnetic systems studied here is that they undergo a phase-transition at a finite temperature, called the critical temperature (in ferromagnets, the Curie point and in antiferromagnets, the Néel temperature). A complete theoretical understanding of phase transitions still eludes theorists, but many promising (relatively) new techniques[14,15] are currently being explored.

Since the difficulty of the phase-transition problem often precludes an exact solution, approximate methods are sought. These approximate methods differ for the itinerant and the localized cases. This thesis will concentrate on understanding the thermodynamics of the localized picture.

As stated above, the Heisenberg Hamiltonian describes localized spins interacting via exchange to a high degree of accuracy. When studying the thermodynamics of spins on a lattice, a further simplification of this Hamiltonian, assuming that the spins

can point only up or down, yields the famous Ising model:

$$H^{Ising} = -\sum_{i,j} J_{ij}\ \sigma_i\ \sigma_j$$

where $\sigma_i = \pm 1$ and J_{ij} is the Ising exchange between sites i and j. The partition function is then written:

$$Z = \sum_{\{\sigma\}} e^{-\beta E(\sigma)}$$

where $\beta = 1/k_B T$ (k_B is Boltzmann's constant, T is the temperature), $\{\sigma\}$ denotes all the possible configurations of the Ising spins, and $E(\sigma)$ is the energy of the system in a particular configuration.

The Ising model approximation reduces the thermodynamics of magnetism to its simplest possible form. Even so, finding the solution to the problem can be very difficult. In fact, exact solutions to the model are known only for one- and two-dimensional systems.

The one-dimensional Ising model, which was actually suggested by Lenz[16], was solved for the case of nearest-neighbor interactions by Ising[17] in 1925. This model, however, does not display a phase transition at a finite temperature.[18]

Lars Onsager[19] calculated the partition function of the two-dimensional Ising ferromagnet with only nearest-neighbor interactions in 1942, and published the result in 1944. Later, in 1948, while at a meeting, Onsager produced the formula for the spontaneous magnetization as a remark during a discussion, but he never published the derivation. (The derivation was later published by Yang.[20])

The importance of Onsager's work can hardly be overstated. The two-dimensional Ising model represented the first exactly solved non-trivial thermodynamic model showing a phase transition. Perhaps the most important function of this solution, outside of its fundamental interest and relationship to "two-dimensional" magnetic

systems, is its use as a test case for approximate methods. By comparing approximate results with the exact solution, the nature of the approximation can be understood.

"Real-world" systems are inherently three-dimensional. There are many methods for approximating the thermodynamic functions of three-dimensional Ising models; each has its advantages and disadvantages. Taken together, they provide a reasonably detailed picture of the exact properties of these systems. There are, however, many fine points that must be understood. Some of these methods are investigated in chapter II.

C. Overview

The systems studied below have one common feature: all involve two-dimensional planar defects interacting with a three-dimensional bulk. Chapter II discusses the properties of {001} antiphase boundaries in the nearest-neighbor face-centered-cubic Ising antiferromagnet (or equivalently, the simple substitutional binary alloy).[21] Chapter III investigates the ground state properties of the surface of a magnetic semiconductor, EuTe.[22] The ground-state magnetic properties of {111} stacking faults in nickel forms the subject matter of chapter IV.[23]

There is another, common bond between these systems. The observed physical phenomena arise directly from competition between (at least) two effects. In the antiferromagnetic Ising model a one-dimensional disorder competes with a two-dimensional internal energy. The magnetic surface structure of EuTe perfectly demonstrates the physics of competing exchange interactions (i.e. nearest-neighbor vs. next-nearest-neighbor exchange). The magnetic properties of the {111} stacking faults are understood in terms of the competition between band-like behavior and magnetic interactions. The physical properties resulting from these various forms of competition are certainly interesting, and often times surprising.

D. References for chapter I

1 For an interesting historical account of the progress in understanding magnetic phenomena see D. C. Mattis, *The Theory of Magnetism I,* (Springer-Verlag, Berlin-Heidelberg-New York-Tokyo, 1988).

2 P. A. M. Dirac, Proc. Roy. Soc. 112A , 661 (1926).

3 W. Heisenberg, *Z. Phys.* 38 , 441 (1926).

4 G. H. Wannier, Phys. Rev. 52 , 191 (1937).

5 C. Kittel, *Introduction to Solid State Physics,* (Wiley, New York, 1986).

6 C. Herring, in *Magnetism, Vol. IV,* edited by G. T. Rado and H. Suhl (Academic, New York, 1966).

7 J. C. Slater, Phys. Rev. 81 , 385 (1951).

8 P. Hohenberg and W. Kohn, Phys. Rev. 136 , B864 (1964).

9 W. Kohn and L. J. Sham, Phys. Rev. 140 , A1133 (1965).

10 L. J. Sham and W. Kohn, Phys. Rev. 145 , 561 (1966).

11 For a review of the density functional formalism see J. Callaway and N. H. March, in *Solid State Physics,* edited by F. Seitz, D. Turnbull, and H. Ehrenreich (Academic, New York, 1984) Vol. 38, p. 135; or R. O. Jones and O. Gunnarsson, Rev. Mod. Phys. 61 , 689 (1989).

12 L. Hedin and B. I. Lundqvist, J. Phys. C: Solid State Phys. 4 , 2064 (1971).

13 C. S. Wang and J. Callaway, Phys. Rev. B 15 , 298 (1977); J. F. Janak and A. R. Williams, Phys. Rev. B 14 , 4199 (1976).

14 K. G. Wilson, Phys. Rev. B 4 , 3174 (1971); Phys. Rev. B 4 , 3184 (1971).

15 M. E. Fisher, Rev. Mod. Phys. 46 , 597 (1974).

16 S. G. Brush, Rev. Mod. Phys. 39 , 883 (1967).

17 E. Ising, *Z. Phys.* 31 , 253 (1925).

18 L. D. Landau and E. M. Lifshitz, *Statistical Physics, Part I,* third edition (Pergamon Press, Oxford, 1980).

19 L. Onsager, Phys. Rev. 65 , 117 (1944).

20 C. N. Yang, Phys. Rev. 85 , 809 (1952).

21 D. C. Chrzan and L. M. Falicov, Phys. Rev. B, 40 , 8194 (1989).

22 D. C. Chrzan and L. M. Falicov, Phys. Rev. Lett. 61 , 1509 (1988); D. C. Chrzan and L. M. Falicov, Phys. Rev. B 39 , 3159 (1989).

23 D. C. Chrzan, L. M. Falicov, J. M. MacLaren, X.-G. Zhang, and A. Gonis, submitted to J. Appl. Phys.

Chapter II : Antiphase Boundaries in an Ising Antiferromagnet

A. Introduction

The true nature of the phase diagram of the face-centered-cubic antiferromagnetic Ising model with only nearest-neighbor interactions, or equivalently the simple binary ordering alloy, has recently been the subject of great debate. Three of the best available methods for calculating the diagram give either conflicting results or are simply not directly applicable. This is particularly alarming as the results of all the methods give good agreement when applied to other systems. The three methods under consideration are 1) low-temperature expansions, 2) the cluster variation method, and 3) Monte Carlo numerical simulations.

The discrepancy[1] centers on the exact location of the triple point (the point defined by the temperature and the magnetic field at which the disordered phase and the two types of ordered phases appearing in the diagram are in equilibrium), and is related to the methods' failure to treat antiphase boundaries (defined below) in a consistent manner. The adequate treatment of antiphase boundaries reconciles the predictions of the three methods. In order to understand how these failures come about, it is necessary to understand something about the three methods.

Low-temperature expansions[2] are extremely useful for obtaining exact information about the low-temperature behavior of the system being studied (low-temperature is defined in terms of the excitation spectrum of the model). The justification of this expansion technique is straightforward. In general, the partition function of an Ising system is given as the sum of $e^{-\beta E}$ over all possible configurations ($\beta = 1/k_B T$, where k_B is Boltzmann's constant and T is the temperature; E is the energy of a configuration -- see chapter I.B). At low temperatures, β becomes very large. Therefore, only terms with very low energy (so that $\beta E \leq 1$) will contribute to the partition function. The low temperature expansion includes only these terms.

Writing down the expansion still requires some work. The derivation of the low temperature expansion for the partition function for an Ising ferromagnet with only nearest-neighbor interactions defined on a simple-cubic lattice of N sites (with periodic boundary conditions) demonstrates the technique. In addition to the Ising interaction described in chapter I, this calculation also includes an externally applied magnetic field, h. The total Hamiltonian is

$$H = -J \sum_{<ij>} \sigma_i \sigma_j - h \sum_i \sigma_i \quad ,$$

where $<ij>$ indicates that the sum includes all nearest-neighbor pairs only.

At zero temperature, the system will have all of its spins pointing in the direction of the magnetic field (the ground state). At a very low, but finite, temperature, some of the spins are flipped. The lowest lying excited states of this model consist of those states where only one spin is flipped and have an energy of $(12J + 2h)$ [$2J$ for each pair of spins aligned antiparallel in the flipped configuration and $2h$ for each spin aligned antiparallel with the magnetic field]. These N configurations contribute $Ne^{-\beta(12J+2h)}$ to the partition function.

The next level of excited states consists of those in which two spins align antiparallel to the magnetic field; the spins can be nearest-neighbors or they can be further apart. In flipping two nearest-neighbor spins, five of the six nearest-neighbor bonds on each site connect a flipped spin to a spin aligned antiparallel to it. Each of these bonds costs $2J$ in energy for a total of $20J$. The interaction with the magnetic field then contributes an energy of $4h$. A total of $3N$ nearest-neighbor pairs in the lattice gives a contribution to the partition function from these excitations of $3Ne^{-\beta(20J+4h)}$. Flipping two spins that are further apart than nearest-neighbors costs double the energy of an isolated spin flip. The calculation of the number of configurations in which two spins, not nearest-neighbors, are flipped proceeds as follows. There are N ways to choose the first site. After choosing the first site, there are

only $(N-7)$ sites left to choose from. The total number of ways to choose the two sites is then $N(N-7)/2$, where the factor of one-half accounts for the double counting of each configuration. Note that the total number of two-site configurations is $N(N-1)/2$ as it should be.

Letting $x = e^{-4\beta J}$ and $y = e^{-2\beta h}$, the low temperature series now appears as

$$Z = 1 + N\, x^3 y + 3N\, x^5 y^2 + N(N-7)/2\, x^6 y^2$$

The expansion can be continued to higher order by considering higher energy excited states (i.e. those with a larger number of flipped spins), although counting the number of configurations soon becomes difficult. (Graphical methods[2,3], similar to those used in the linked-cluster expansion are often used for this task. The difficulties stem from constraints imposed by the topology of the lattice.)

Completion of the calculation requires that the thermodynamic limit be taken. In this limit, one expects, on physical grounds, that

$$Z = (Z_o)^N$$

where $Z_o = e^{-\beta f}$ and f is the Helmholtz free energy per site. (This follows from the extensive property of the Helmholtz free energy.) It is assumed that

$$Z_o = 1 + y\, g_1(x) + y^2 g_2(x) + \ldots.$$

where the $g_i(x)$ are to be determined by comparing the two expressions for Z given above. The comparison gives

$$Z_o = 1 + yx^3 + 3y^2(x^5 - x^6) + O(y^3 x^8).$$

Z_o can then be used to calculate the low-temperature thermodynamic properties of this model.

The above derivation includes at least one implicit assumption: that the internal energy of an excitation scales with the number of flipped spins. In the limit of vanishing magnetic field (or low magnetic field), it is not, however, rigorously correct to assume that all excited states with $(n+1)$ flipped spins are at a higher energy than those with n flipped spins. If no external field is present, the energy of excitation for flipping a cluster of spins scales with its surface area and not its volume. The order of the error in any given expansion can be determined, so this assumption does not pose a fundamental problem.

The expansions do have limitations and difficulties associated with them. For example, their analytic properties imply that the expansions alone cannot make precise predictions about thermodynamic properties near a phase transition. There have been attempts to extend their range of validity to near the transition temperature through the use of Padé approximants, which have met with some success.[4] But overall, the difficulties inherent in predicting the physical properties of a system, at a temperature for which the free energy is non-analytic, from the properties at temperatures for which the free energy is analytic, seem overwhelming.

A more serious problem is that in certain systems (e.g. the nearest-neighbor Ising antiferromagnet defined on a face-centered-cubic lattice field) the ground state is infinitely degenerate. In these situations, it is not clear which of the ground states should be used for the expansion. The seemingly obvious choice of averaging over all ground state configurations is not always the correct approach, as will be discussed below.

The cluster variation method[5] (CVM) represents a variational approach to calculating the thermodynamic properties of a simple spin system. The number of configurations of a system is approximated in terms of the probability of finding clusters of a predetermined size and configuration in the lattice at a specific temperature. The method proceeds through the calculation of a trial Helmholtz free energy (or in an

equivalent but somewhat more useful formulation, a trial grand potential is calculated). Minimization of the trial free energy with respect to the cluster probabilities calculates the best estimate of the true free energy, within that level of approximation, at the specified temperature and magnetic field.

It is a simple task to express the internal energy of an Ising system in terms of cluster probabilities. It is not as simple to calculate the entropy associated with a given set of probabilities. This task is accomplished systematically in CVM. The hierarchical structure of CVM starts with the simple mean-field approximation[6], moves into the Bethe pair approximation[7], and even further into more accurate approximations involving larger clusters, the topology of which depends on the lattice being considered.

As an example of the procedure used to calculate the entropy, the trial free energy of the simple cubic lattice is derived using a nearest-neighbor pair as the largest cluster.[8] There are two types of clusters which enter the calculation: the single-site clusters, and the nearest-neighbor pairs. The single-site probabilities are denoted by $x_+(x_-)$, which refer to the probability of finding an up(down) spin at a site of the lattice. These variables must satisfy the constraint:

$$x_+ + x_- = 1 \quad .$$

The pair probabilities are denoted by $y_{[+,+]}$, $y_{[+,-]} = y_{[-,+]}$, and $y_{[-,-]}$, and must be such that

$$y_{[+,+]} + y_{[+,-]} = x_+$$

$$y_{[-,+]} + y_{[-,-]} = x_- \quad .$$

Here, $y_{[+,+]}$ is the probability of finding a nearest-neighbor pair of spins both pointing in the positive z-direction, etc.

In the first step of the approximation, one calculates the number of ways of arranging the nearest-neighbor pairs, without regard to whether or not the arrangement is physically allowable (the bonds are assumed to be distributed completely at random over the possible bonds in the lattice without concern whether or not all bonds originating from a given site require the same atom to be at that site -- see figure 2.1). In the second step, a correction is applied to the number calculated in the first step. Using these ideas, the number of configurations for the Ising model on a simple-cubic lattice is

$$\# \; conf. = \left\{ \frac{(3N)!}{(3Ny_{[+,+]})!(3Ny_{[+,-]})!(3Ny_{[-,+]})!(3Ny_{[-,-]})!} \right\}$$

$$\times \left\{ \frac{[N!/(x_+N)!(x_-N)!]}{[(6N)!/(6x_+N)!(6x_-N)!]} \right\} ,$$

where N is the total number of sites in the lattice. The second factor on the right (arising from the second step) represents the fraction of the number of configurations of the pair variables [the first factor on the right] which are physically allowable (figure 2.1). The correction factor is calculated simply as the fraction of the total number of ways to arrange zN spins over the N sites of the lattice (where z is the coordination number -- for the simple cubic lattice $z = 6$), with z per site, which have all z spins at each site pointing in the same direction.

Using Sterling's approximation and a simple pairwise expression for the internal energy of the Ising model, the trial free energy per site is written

$$F = 3J(-y_{[+,+]} - y_{[-,-]} + y_{[+,-]} + y_{[-,+]}) - h(x_+ - x_-) - 5k_BT(x_+ \ln x_+ + x_- \ln x_-)$$

$$+ 3k_BT(y_{[+,+]} \ln y_{[+,+]} + y_{[+,-]} \ln y_{[+,-]} + y_{[-,+]} \ln y_{[-,+]} + y_{[-,-]} \ln y_{[-,-]}) \; .$$

Minimization with respect to the site and pair probabilities, subject to the constraints given above, finds the best approximation to the true free energy, in the pair

approximation, at the specified magnetic field and temperature. Information about long-range order, short-range order and all the thermodynamic properties can be obtained from this best estimate.

A similar analysis can be carried out using larger clusters, although the approximation becomes more difficult to perform with increasing cluster size. Unfortunately, rigorous estimates of errors made in using only a finite number of cluster probabilities are not available . In fact, for the face-centered-cubic Ising antiferromagnet with only nearest-neighbor interactions the pair approximation fails completely, predicting that the system will never become ordered. Even for the four-site approximation to this system, the absolute CVM minimum underestimates the free energy of segregation[9], and a local minimum in the trial free energy must be used to obtain meaningful results. The use of larger clusters eliminates this problem, but the calculation rapidly becomes prohibitively expensive.

As in the low-temperature expansions, CVM includes implicit approximations and assumptions. Most notably, all possible ordered phases are not investigated because the choice of the maximum-sized cluster predetermines which ordered phases are possible. It is therefore necessary to know which phases appear in the phase diagram *before* the calculation is begun. In addition, there are certain types of disorder which cannot be handled within the formalism of CVM. The antiphase boundaries discussed below are one example.[10]

Monte Carlo numerical simulations are a third approach to solving the Ising model in three dimensions. The properties of a large cluster of spins ($\approx$ 15000 with periodic boundary conditions) are computed statistically.

These simulations begin with the choice of an initial configuration, usually either a completely random or completely ordered state. A site (or group of sites) is chosen at random and the spin (or spins) is (are) flipped with a probability defined by

$$p = \begin{cases} e^{-\beta\Delta E} & \Delta E > 0 \\ 1 & \Delta E < 0 \end{cases}$$

where ΔE is the change in internal energy associated with flipping the spin (or cluster of spins). The flipping process is continued until equilibrium is reached, and the thermodynamic properties of the system are then extracted from the final equilibrium configuration.

In principle, this method should produce the exact thermodynamics of the periodic cluster being investigated, although the computer time necessary to do so grows rapidly with cluster size. It is thought that the thermodynamics of the finite-sized cluster adequately represents the thermodynamics of the infinite system. Therein lies the fundamental difficulty of the Monte Carlo approach. It is well known that finite-sized systems can never show a phase transition; the free energy is always analytic. However, as the size of the cluster used in simulations increases, the temperature regions at which the non-analyticities appear in the infinite system will begin to show a "tendency" towards non-analytic behavior. The observation of this "tendency" is the foundation of the usefulness of the Monte Carlo approach.

Computers are now fast enough, and the methods efficient enough, to perform calculations on very large systems for which the "tendency" towards non-analyticity is clear. In addition, Monte Carlo studies do not require prior knowledge of the phase diagram. In fact, the studies are believed to produce the most accurate calculations of the thermodynamic properties of the three-dimensional Ising model.

Like the other methods, Monte Carlo techniques do have drawbacks. While it is not necessary to have prior knowledge of the phase diagram, this lack of information can make interpretation of the results difficult. In addition, a rigorous technique for for correctly inferring the thermodynamics of infinite-sized systems from those calculated for finite-sized systems does not exist. In fact, finite-sized clusters allow excita-

tions which are not present in the infinite-sized systems. These excitations have serious implications for how one calculates the true thermodynamic properties of the infinite system, as demonstrated below.

A remarkable similarity exists between the simple ordering substitutional binary alloy and the antiferromagnetic Ising model in the presence of a magnetic field. Hence most of the literature on the antiferromagnetic Ising model defined on an *fcc* lattice appears in the context of alloys. An A-B binary alloy can be mapped onto the Ising model: an atom of type A (B) is equivalent to an up (down) spin. The chemical potential difference between atoms of different types is equivalent to an external magnetic field. The energy is then written:

$$E = \sum_{ij} J_{ij}\ \sigma_i \sigma_j - h \sum_i \sigma_i$$

where σ_i is an Ising spin at site i which can take on the values ± 1, J_{ij} is the interaction energy between spins at sites i and j, and h is the external magnetic field. (The particular model under consideration in the following is defined in an *fcc* lattice and such that $J_{ij} = J > 0$ (i.e. antiferromagnetic exchange) for i and j nearest-neighbors, and $J_{ij} = 0$ for all other pairs).

Real alloys are significantly more complex than the simple Ising model analogy.[11,12] In particular, many body effects[13], atomic-size,[14] and Fermi-surface[15,16] properties are all expected to play important roles in determining the true phase stability. It is unlikely that these effects can all be reduced to pairwise interactions. The Ising model, however, does provide a good starting point for understanding the thermodynamic properties of alloys, and the model can be made more realistic by successive inclusion of some of the neglected effects. A clear understanding of the Ising model's phase diagram will indicate which properties of the alloy are a direct result of configurational terms, and which stem from electronic terms.

Thus far, approximate methods have resulted in a widely accepted topology[1] for the phase diagram of the nearest-neighbor *fcc* Ising antiferromagnet, but some discrepancies still remain. There are three types of phases present in the phase diagram: the disordered phase, the $L1_0$ (AB) phase, and the $L1_2$ (A_3B) phase (see figure 2.2). The *fcc* lattice can be decomposed into four interpenetrating simple-cubic sublattices. The three phases can then be understood in terms of the concentrations of up and down spins on each sublattice. In the disordered phase, all of the sublattices have equal concentrations of up spins. In the $L1_0$ phase, there are two groups of two sublattices which have different concentrations. In the $L1_2$ phase, the sublattices are divided so that three of them are equivalent to each other (i.e. have the same concentrations of up spins) and different from the fourth.

The thermodynamic calculations reported in literature for this Ising system fall into three categories: small cluster variational techniques, numerical simulations, and low- and high-temperature expansions. The results of the different methods are often compared among themselves, for consistency, and also compared with experimental results believed to reflect Ising-like behavior (e.g. the Cu-Au alloys).

One early small-cluster calculation on the *fcc* binary alloy was due to Shockley[6], who calculated the Cu-Au phase diagram using a mean-field approach. The agreement with the experimentally known Cu-Au phase diagram was not satisfactory: the calculated phase diagram was topologically different from that of the experiments. The following years brought the development and application of the quasi-chemical method[17], and later the cluster variation method[5,18–20] (CVM). The latter led to qualitatively good agreement with the experimentally determined phase diagrams, and the agreement with experiment was improved even further with the inclusion of "many-body" effects[21]. In addition, CVM results produced the currently accepted topology of the nearest-neighbor *fcc* Ising antiferromagnet's phase diagram.

The initial Monte Carlo results of Binder[22] and Phani *et al.*[23] for the *fcc* Ising antiferromagnet with only nearest-neighbor interactions disagreed with those of CVM, which necessitated reexamination of both results.[24–27] As mentioned above, the conflict centered on the exact location of the triple-point [the point where the disordered, the $L1_0$, and the $L1_2$ phases are in equilibrium]. While the calculated transition temperatures of the stoichiometric compounds were not too different (the Monte Carlo calculations gave slightly lower transition temperature for all compositions of the alloy), Binder's Monte Carlo results placed the triple-point at $T = 0$, and CVM placed the triple-point temperature at a nonzero value, of the order of the pair-interaction energy.[5,17–19]

One source of this discrepancy arises from the frustration present in the *fcc* lattice. The frustration may lead to the appearance of {001} antiphase boundaries, which are explicitly excluded in CVM, and difficult to interpret in Monte Carlo studies. A {001} antiphase boundary in the $h = 0$, $T = 0$ case is depicted in figure 2.3, using a description similar to Kikuchi and Sato's.[28] The configurations of the four possible (001) planes for the perfectly ordered case are shown. Each dark symbol (either square or circle) represents an up spin (Cu atom), and the lighter symbols represent down spins (Au atom). The $L1_0$ phase is constructed by stacking the planes in one of four configurations: (...AaAaAaAa...), (...AbAbAbAb...), (...BaBaBaBa...) or (...BbBbBbBb...). An antiphase boundary is introduced by a slip of one half of the lattice by $[a/2, a/2, 0]$ where a is the cubic lattice spacing. This is the equivalent of going from (...AaAaAaAa...)-type stacking to (...AaAaBbBb...)-type stacking. (In the definition of antiphase boundary used here, it extends throughout the entire crystal; domains separated by antiphase boundaries are not considered). The dashed boxes in the figure contain one nearest-neighbor tetrahedron of the face-centered-cubic lattice, with two atoms from each of the planes. Each of these tetrahedra has two up spins and two down spins, the minimal energy configuration, for both Ba and Bb stacking

order. This is also true for Aa and Ab stacking. It therefore costs no energy to stack the planes in a random order (...ZzZzZzZz...) where each Z (z) is a plane of type A (a) or B (b). The system has an infinitely degenerate ground state. An infinitesimal next-nearest-neighbor interaction, however, removes this degeneracy.

Antiphase boundaries are present in the Monte Carlo calculations[25–27], as revealed by studies of the triple point region. The presence of antiphase boundaries in the Monte Carlo results raises important issues. In Binder's calculations, one antiphase boundary would result in a state with no long-range order, but, physically the system still has a large degree of long-range order, at least in two dimensions, and is very different from the random, disordered configuration. With a more precise definition of order (which accounts for the long-range order still present in the antiphased state), the Monte Carlo calculations yield a nonzero triple-point temperature.[25–27] The puzzle is not completely solved, however, for the triple-point temperature in the Monte Carlo results is roughly two-thirds of the triple-point temperature predicted by the best available CVM results.[1] In addition, the transition temperatures predicted by the Monte Carlo methods are still consistently lower than those of CVM.

It is not yet clear whether or not antiphase boundaries appear in the true phase diagram of the nearest-neighbor *fcc* Ising antiferromagnet. There are reasons to expect that the boundaries might be present. Antiphase boundaries cost no energy, but there is an entropy associated with their presence. In the thermodynamic limit, the free energy is of order n^3 [where n^3 is the number of spins (atoms) in the system], and the contribution from antiphase boundaries is of order n, hence negligible.

This argument suggests that the antiphase boundaries are present even as $T \rightarrow 0$, but do not affect the thermodynamic properties of the system. Clearly, the system with antiphase boundaries is considerably different from the system without them (e.g. the x-ray diffraction pattern of the system with antiphase boundaries is considerably different than that of the system without antiphase boundaries), regardless of their

influence on the free energy, which makes it important to determine whether or not antiphase boundaries exist at a given temperature.

Slawny[29] made significant progress in this direction when he pointed out that the one-dimensional structure of this system does directly influence its thermodynamics. Slawny noted that the excitation spectrum of a particular ground state depends extremely sensitively on its one-dimensional antiphase boundary structure. Since the excitation spectrum determines a particular ground state's thermodynamic properties, the one-dimensional disorder has a dramatic influence on the thermodynamics of the system. Slawny's exact arguments apply to a class of systems satisfying three criteria: the system must have a (1) *finite* number of degenerate, (2) *periodic* states in the ground-state manifold which all (3) meet the *Peierls' condition*[30]: that there be an energy gap between the ground state and the first excited state. For these systems, the "true" ground state is the state which admits the largest number of low-lying excitations.

The nearest-neighbor *fcc* Ising antiferromagnet clearly violates the first two of these conditions. The ground-state manifold contains an *infinite* number of *not necessarily periodic* states. Slawny introduces interactions into the model which insure long-range order in three dimensions so that the conditions of his theorem are met, and then considers the limit as these interactions go to zero. He concludes that antiphase boundaries do not appear in the low-temperature expansion for the nearest-neighbor *fcc* Ising antiferromagnet. Based on Slawny's arguments, Mackenzie and Young[31], and later, Lebowitz *et al.*[4] calculated low-temperature expansions about the "true" ground state: the ordered $L1_0$ phase *without* antiphase boundaries. This is a somewhat surprising result: the "true" ground state of the system is "selected" based solely on entropic contributions, and the result of this "selection" is the completely ordered state.

Slawny's conclusions most probably apply to the *fcc* Ising system under consideration here, but there is some danger in his approach. The infinite one-dimensional

degeneracy of the model only exists in one point of parameter space. The fact that an infinitesimal next-nearest-neighbor interaction removes the infinite degeneracy suggests that limiting processes may not be applicable.

Assuming that Slawny's conclusions are correct, there is still more work to be done. It is of interest to understand the behavior of the Ising model at temperatures for which low-temperature expansions are no longer valid. Slawny's arguments do not indicate whether or not antiphase boundaries appear at higher temperatures.

The purpose of this chapter is to investigate, in greater detail, whether or not antiphase boundaries appear in the equilibrium phase diagram of the nearest-neighbor *fcc* Ising antiferromagnet (and by analogy, in the simple binary substitutional alloy). The approach chosen is the construction and solution of an exactly soluble model for cubic {001} antiphase boundaries which violates the first two Slawny criteria. This violation is of the kind encountered in the nearest-neighbor *fcc* Ising antiferromagnet. The insight gained by solution of this simple model can be applied to the more difficult Ising problem, and to understand the role of antiphase boundaries in more complex real alloys.

Section B of this chapter develops the model, which is subsequently solved in section C. Analysis of the results comprises section D, and section E contains the conclusions.

B. The Model

The excitations of the Ising systems consist of spin flips in given configurations. Each antiparallel spin pair that gets converted into a parallel spin pair requires a positive energy of $2J$. Conversely, each parallel spin pair converted into an antiparallel one yields a negative $-2J$ energy. There is an additional $\pm 2h$ extra energy arising from the change of orientation of *each spin* with respect to the external field. The energy spectra of the all states in the ground-state manifold of the nearest-neighbor *fcc*

Ising antiferromagnet are characterized by a set of common low-lying excitations. Since each spin has eight antiparallel and four parallel nearest neighbors, individual, disconnected spin flips produce the lowest level excitations, equal to $(8J \pm 2h)$. The first configuration-dependent differences in the spectra appear in the third level of excitation.[32] The difference, related to the antiphase structure, arises from the simultaneous flip of four closely situated spins[33] ; they are shown in figure 2.4. They are in three successive (001) planes, in the configuration 1-2-1. In this cluster each spin has two of its twelve nearest neighbors within the cluster, and the other ten outside. If all nearest-neighbor pairs connected to this cluster are included, there are altogether 44 pairs; four within the cluster, 40 outside it. The important difference, as shown in figure 2.4, is that in the perfectly ordered $L1_0$ structure the four internal bonds are all antiparallel, whereas in the structure with an antiphase boundary two of the pairs are antiparallel, and two parallel. Moreover the 44 total pairs related to the cluster are 28 parallel and 16 antiparallel pairs in the perfectly ordered $L1_0$ structure, as opposed to 30 and 14, respectively, in the one containing the antiphase boundary. When those four spins are simultaneously flipped the four internal "bonds" remain unchanged; the 40 "outside bonds" on the other hand change character. As a consequence the excitation energy of that four-atom flip is $16J$ in the perfect structure, and $(32J \pm 4h)$ in the defective one.[34] (The $\pm 4h$ term corresponds to the fact that in the defective structure there is a net change of two spin orientations; the sign is chosen to reflect the relative orientation of these two spins with respect to the external magnetic field.)

The presence of one antiphase boundary shifts of the order of n^2 excitations of this type to a higher, magnetic-field dependent energy. (The number of sites in the lattice is n^3.) For zero external field (chemical potential difference), the state with the highest number of third-level excitations is the $L1_0$ phase, and this number decreases as the number of antiphase boundaries increases.

The model constructed in this chapter mimics these properties as closely as possi-

ble while still allowing a simple, exact solution for the thermodynamic properties. Similarly to the nearest-neighbor *fcc* Ising antiferromagnet, the model below has an *infinite* ground state degeneracy in which the states are *not necessarily periodic*. The antiphase dependence of the excitation spectra is very similar in the two systems. Each state in the ground-state manifold of the constructed model admits a common set of lowest-lying excitations, but the number of second-level excitations is determined by the antiphase structure of the state: a state with more antiphase boundaries has fewer second-level excitations because the presence of an antiphase boundary shifts some second-level excitations to higher energy.[35] However, the model does not account for in-plane correlations among the spins.

The model system is composed of n planes, each of which contains N sites. The planes are indexed by the subscript k, and each site within a plane is indexed by the subscripts i and j. The thermodynamic variables are defined to be σ_{ijk} and Σ_k, both of which can assume the values ± 1. The variable σ_{ijk} corresponds to individual spins; on the other hand Σ_k is the *antiphase-boundary* variable. The spins on plane k interact directly with the spins immediately adjacent on planes $k-1$ and $k+1$, but do *not* directly interact with the other spins on plane k. The perfect structure corresponds to Σ_k which are all of the same sign. An antiphase boundary in the model occurs at a plane k such the $\Sigma_k \Sigma_{(k+1)} = -1$, and changes the interaction energy between spins on adjacent planes. A configuration is designated by $\{\sigma, \Sigma\}$. The internal energy is

$$E(\{\sigma, \Sigma\}) = \varepsilon \left\{ \sum_{ijk} (1 + \sigma_{ijk}) + (1/4) \sum_{ijk} (1 + \sigma_{ijk})\,(1 + \sigma_{ij(k+1)})\,(\gamma_0 - \gamma \Sigma_k \Sigma_{(k+1)}) \right\}$$

where the indices run over the entire system, and periodic boundary conditions are *not* assumed. The first term accounts for the elementary excitations of the sites; they have energy 2ε and correspond to flipping a spin in an external field. (The energy scale is set by the value of ε.) The second sum represents an antiphase-structure dependent interaction between excitations on adjacent planes. The states of two adjacent planes,

reflected in the values of their Σ_k's, determine the excitation spectrum of the sites in those planes. If both sites i, j, k and $i, j, (k+1)$ are excited (the factors containing the σ's impose this restriction) there is an additional excitation energy associated with their juxtaposition. This additional energy is $[\gamma_0 - \gamma]$ for the normal $[\Sigma_k \Sigma_{(k+1)} = 1]$ state and $[\gamma_0 + \gamma]$ for the antiphased $[\Sigma_k \Sigma_{(k+1)} = -1]$ state. (The parameters γ_0 and γ are positive dimensionless constants such that $\gamma < \gamma_0$.) The local excitations involving two correlated sites have energies of $(4 + \gamma_0 - \gamma)\varepsilon$ and $(4 + \gamma_0 + \gamma)\varepsilon$. The energy difference between excitations correlated across and antiphase boundary and those correlated away from an antiphase boundary is the antiphase excitation gap, $2\gamma\varepsilon$. For $\gamma = 0$, the energy of the correlated excitations is no longer antiphase structure dependent. In this limit, (and, as is shown below, for the case where n goes to infinity and $N \approx n^2$) the model becomes a collection of N one-dimensional Ising chains, each with n sites; the external magnetic field is given by $h = -\varepsilon[1 + (\gamma_0 - \gamma)/2]$ and the nearest-neighbor spin coupling is $J = \varepsilon(\gamma_0 - \gamma)/4$.

The partition function of the model system containing nN sites is written:

$$Z_{nN} = \sum_{\{\sigma,\Sigma\}} e^{-\beta E(\{\sigma,\Sigma\})}$$

where $\beta = 1/k_B T$, k_B is Boltzmann's constant, and T is the temperature.

C. The Solution of the Model

Let μ_k denote the number of sites in plane k which are excited, and ν_k the number of these for which the equivalent site in plane $(k+1)$ is also excited. The number of configurations for a two plane system is

$$C_N^{\mu_1} C_{\mu_1}^{\nu_1} C_{N-\mu_1}^{\mu_2 - \nu_1} \tag{2.1}$$

where C_N^M is the binomial coefficient:

$$C_N^M = \frac{N!}{(N-M)!\, M!}.$$

The first coefficient in (2.1) is the number of ways to choose the μ_1 sites on plane 1, the second, the number of ways to choose the ν_1 sites on plane 2 which are juxtaposed with an excitation on plane 1, and the last, the number of ways to place the remaining excitations on plane 2. There are restrictions on the values for μ_1, ν_1, and μ_2. All physically allowed configurations of the planes are included by summing over all terms for which expression (2.1) is defined.

The analysis above is easily extended to the case of n planes. The energy in terms of the μ_k and ν_k is

$$E = 2\varepsilon \sum_{k=1}^{n} \mu_k + \varepsilon \sum_{k=1}^{n-1} \nu_k(\gamma_0 - \gamma\Sigma_k\Sigma_{k+1}). \tag{2.2}$$

The partition function is

$$Z_{nN} = \sum_{\{\Sigma\}} \sum_{\mu_1} \cdots \sum_{\mu_n} \sum_{\nu_1} \cdots \sum_{\nu_{n-1}} \left\{ C_N^{\mu_1} \prod_{k=1}^{n-1} C_{\mu_k}^{\nu_k} C_{N-\mu_k}^{\mu_{k+1}-\nu_k} \right\} \left\{ \prod_{k=1}^{n-1} x_k^{\nu_k} \right\} (w)^{\sum_{k=1}^{n} \mu_k} \tag{2.3}$$

where $\sum_{\{\Sigma\}}$ is a sum over all configurations of the antiphase boundaries, the remaining sums run over all physical values of μ_k and ν_k, $w = e^{-2\beta\varepsilon}$ and $x_k = e^{-\beta\varepsilon(\gamma_0 - \gamma\Sigma_k\Sigma_{k+1})}$.

The terms involving ν_{n-1} and μ_n reduce to terms involving μ_{n-1}

$$\sum_{\nu_{n-1}} \sum_{\mu_n} C_{\mu_{n-1}}^{\nu_{n-1}} C_{N-\mu_{n-1}}^{\mu_n - \nu_{n-1}} \, x_{n-1}^{\nu_{n-1}} \, w^{\mu_n} = (1+w)^{N-\mu_{n-1}} \, (1 + x_{n-1}w)^{\mu_{n-1}}.$$

This reduction of terms allows exact solution of the model, using techniques similar to those employed in the transfer matrix method. If the variable y_k is defined by the following (descending index) mapping:

$$y_k = w \, \frac{(1 + x_k y_{k+1})}{(1 + y_{k+1})}, \qquad y_n = w, \tag{2.4}$$

then the partition function is then given by

$$Z_{nN} = \sum_{\{\Sigma\}} \prod_{k=1}^{n} (1 + y_k)^N \ . \tag{2.5}$$

The sum over all configurations of the antiphase boundaries, which is not performed analytically, is complicated because each y_k depends on the antiphase structure of all the layers $\geq k$. (The sum has been calculated numerically for small n.) The apparent asymmetry of this solution is caused by the method of solution; it can be demonstrated (analytically for small n, numerically for larger n) that the expression for a given configuration is independent of the end from which the mapping (2.4) is begun.

D. Analysis

Expression (2.5) can be used to prove that in the thermodynamic limit (i.e. infinite-sized system), the free energy of the three-dimensional system is exactly the free energy of one of the two states without antiphase boundaries. Slawny's conclusions that only one of the many states of the ground-state manifold should appear in the low temperature expansions is indeed applicable to this system. Even more importantly, in the thermodynamic limit antiphase boundaries have zero concentration at any finite temperature.

The free energy of the d-dimensional model system (i.e. a system where $N \approx n^{d-1}$) is proportional to the natural logarithm of the partition function

$$F = -k_B T \ \ln \left\{ \sum_{\{\Sigma\}} \prod_{k=1}^{n} (1 + y_k)^{n^{d-1}} \right\}. \tag{2.6}$$

The two states without antiphase boundaries contribute the largest terms to the sum, and the next largest terms are from configurations with just one antiphase boundary. This makes physical sense, because each antiphase boundary replaces approximately n^{d-1} second-lowest-lying excitations by slightly higher ones. The result of this replacement is a reduction in the value of the product over k. The free energy can be written

$$F = -k_B T \ln S_{\max} - k_B T \ln \left\{ 2 + 1/S_{\max} \sum_{\{\Sigma'\}} \prod_{k=1}^{n} (1 + y_k)^{n^{d-1}} \right\} . \qquad (2.7)$$

where $S_{\max}$ is the largest term in the sum over configurations in (2.6), i.e. that corresponds to the two perfectly ordered states, and the sum over $\{\Sigma'\}$ includes all configurations except those two corresponding to $S_{\max}$. The first term in (2.7) is proportional to n^d. For the last term of expression (2.7) to contribute to the free energy, it must also be proportional to n^d. The second largest terms in the sum over antiphase configurations differ from the largest for some $m < n$ of the y_k. Define α to be the geometric mean of the ratio of these altered terms to their corresponding values in the product for the system with no antiphase boundaries:

$$\alpha = \prod_{j=1}^{m} \left\{ \frac{1 + y_j}{1 + y_{\max\, j}} \right\}^{1/m} < 1 \quad .$$

If the number of configurations with only one antiphase boundary is taken to be 2^n -- obviously an overestimate since 2^n is the *total* number of configurations -- then the last term in equation (2.7) is less than or equal to

$$-k_B T \ln \left\{ 2 + 2^n \alpha^{n^{d-1}/m} \right\} = -k_B T \ln \left\{ 2 + (2^{n^{2-d}/m}\ \alpha)^{n^{d-1}/m} \right\} . \qquad (2.8)$$

The only way in which (2.8) can be of order n^d is if $(2^{n^{2-d}/m}\ \alpha) > 1$, which is possible only if $n^{2-d}/m > 0$. Since $1 \le m < n$, antiphase boundaries do not appear[36] in the free energy for $d > 2$, and hence do not appear in the three-dimensional system.

For $d > 2$, it can be proven explicitly that the antiphase boundaries themselves do not appear. Assume that the second largest terms in the sum arise from configurations with approximately n antiphase boundaries, and that there are 2^n of these configurations. With arguments similar to those developed above for the free energy, the contribution from these terms to the concentration of antiphase boundaries is found to be zero:

$$\lim_{n \to \infty} (2^{n^{2-d}/m}\ n^{n^{1-d}/m}\ \alpha)^{n^{d-1}m} = 0 \quad , \quad d > 2 \quad . \tag{2.9}$$

This is physically reasonable since it has been argued that, if present, antiphase boundaries must affect the observable thermodynamic properties of the system. In this situation, the absence of antiphase boundaries in the free energy is indicative of their zero concentration.

While antiphase boundaries cost no energy in the ground state, there is a free energy associated with their creation at any nonzero temperature (this energy stems from the coupling between the site spin-variables, σ_{ijk}, and the antiphase variables, Σ_k). The energy of one boundary is proportional to the "antiphase excitation gap", $2\gamma\varepsilon$, multiplied by the necessarily finite number of juxtaposed single-site excitations which scales with the area of the planes, n^{d-1}. In the thermodynamic limit, the energy cost becomes infinite (for $d > 1$). This argument suggests that antiphase boundaries have zero concentration in any version of this system with dimension larger than one, and that antiphase boundaries appear only for $d = 1$. [A seemingly unphysical one-dimensional antiphase boundary is defined *mathematically* by setting $d = 1$ in expression (2.6).]

For $d > 1$ it is possible to write down the complete partition function of the model in a compact form, which can then be used to calculate all the thermodynamic functions. Since no antiphase boundaries appear, the partition function is determined entirely by the period-one fixed point of the mapping (2.4). (For the case with no antiphase boundaries, the x_k of (2.4) becomes a constant, $x_\infty = e^{-\beta\varepsilon(\gamma_0 - \gamma)}$, independent of k). The partition function is

$$Z_{n^d} = (1 + y)^{n^d} \quad , \quad d \geq 2 \tag{2.10}$$

where y is the period-one fixed point of the mapping (2.5) with x_∞ substituted for x_k:

$$y = 1/2 \left\{ x_\infty w - 1 + [\,(x_\infty w - 1)^2 + 4w\,]^{1/2} \right\} . \tag{2.11}$$

(Surface effects are neglected.)

The free energy is easily calculated from equations (2.10) and (2.11). In the limit $\gamma_0 = \gamma = 0$, the free energy is that expected for an assembly of n^d non-interacting two-state systems. (Strictly speaking, in this limit antiphase boundaries appear, but since they do not alter the excitation spectra of the various states, their contribution to the free energy is strictly one dimensional and vanishes in the thermodynamic limit. The concentration of antiphase boundaries is exactly one half for all temperatures.) For $\gamma_0 \neq \gamma = 0$, the boundaries (which are again decoupled from the system) appear but, the two-state systems are now correlated. With $\gamma_0 \neq 0$, $\gamma \neq 0$, the system has no antiphase boundaries; the sites are, however, still correlated. The heat capacity per site for $d = 3$ (figure 2.5), which displays a Schottky anomaly, shows that the correlated system is still very similar to a collection of isolated two-state systems.

In one dimension, the antiphase boundaries can be defined mathematically and are expected to occur. The entire expression (2.5) must be used to calculate the thermodynamic properties. The partition function is calculated for periodic one-dimensional systems containing up to sixteen sites, and the concentration of antiphase boundaries is computed. This concentration is plotted as a function of $\beta\epsilon/(1 + \beta\epsilon)$ in figure 2.6 for $\gamma_0 = 0.8$, and (a) $\gamma = 0.1$, (b) $\gamma = 0.3$, and (c) $\gamma = 0.6$. (The abscissae are zero at infinite temperature, and one at zero temperature.) The results are not very sensitive to the number of sites: there is no perceptible difference between the four- and sixteen-site calculations. At very low temperatures (right side of figure 2.6), the concentration of antiphase boundaries is one half, exactly the value expected from averaging over all of the ground states. The physical difference between the three curves is the antiphase excitation gap, $2\gamma\epsilon$, which increases from curve (a) through curve (c). As the temperature increases from zero, the concentration of antiphase boundaries decreases; the system becomes *more ordered,* with respect to antiphasing, as the temperature is *increased.* (In this situation, "order" is proportional to the concentration of antiphase

boundaries; the boundaries themselves do not form an ordered structure but are distributed randomly over the sites of the system). The physics behind this unusual behavior is quite clear. The system begins to order so that the number of excitations available to it at lower temperatures actually increases, just as in the three-dimensional case. The apparent ordering actually results in an *increase* in entropy. As the temperature increases further, the concentration of antiphase boundaries increases towards its infinite temperature value of one half.

Whereas antiphase boundaries have zero concentration in the infinite three-dimensional model, they do appear *with nonzero concentration at equilibrium* in finite-sized clusters with periodic boundary conditions. These are precisely the type of systems used in the Monte Carlo calculations. It is therefore possible that these results reflect the presence of antiphase boundaries which are unstable in the thermodynamic limit. Figure 2.7 is a plot of the concentration of antiphase boundaries (for $d = 3$) versus the same function of $\beta\varepsilon$ used in figure 2.6, for $\gamma_0 = 0.5$ and $\gamma = 0.2$, for systems with up to $16^3 = 4096$ sites. (The Monte Carlo calculations are often performed on systems containing on the order of 6000 sites.[19–21]) Figure 2.8 is the same type of plot for the parameters $\gamma_0 = 0.8$ and $\gamma = 0.6$.

As in the one-dimensional case, the concentration of antiphase boundaries is one half for very low temperatures. For a finite range of temperatures an increase in temperature reduces the concentration of antiphase boundaries. Unlike the one-dimensional case, these results depend on the size of the system. For larger systems, the concentration of antiphase boundaries decreases more rapidly as the temperature increases. This makes physical sense, since the energy cost of a nonzero temperature antiphase boundary scales as n^2. In the thermodynamic limit, the concentration of antiphase boundaries is zero everywhere except at $T = 0$ and $T = \infty$. The actual value of the minimum is also a function of the antiphase excitation gap.

It is very likely that the nearest-neighbor *fcc* Ising antiferromagnet behaves similarly. Further insight is gained by analyzing how Ising model maps onto the model solved here. The most notable feature is that the effective value of the antiphase excitation gap for the Ising model is magnetic field dependent. In the Ising model at zero temperature, the antiphase excitation gap is given by $16J \pm 4h$. (The antiphase excitation gap is always determined by the lowest energy excitations which distinguish between the many ground states.) The gap actually decreases as the triple-point field is approached, suggesting that antiphase boundaries are more likely to appear, as is observed in the Monte Carlo studies.[25–27,37] It seems unlikely, however, that the effective value of γ can ever be identically zero, which is a necessary condition to have a nonzero concentration of antiphase boundaries in the thermodynamic limit.

The connection between complete disorder and and the appearance of antiphase boundaries needs to be carefully examined. Clearly, an antiphase boundary is not definable in the disordered state. If, however, there is any amount of long-range order, the concept of an antiphase boundary is meaningful and it is then important to understand the relationship between the three-dimensionally disordered state and the one-dimensionally disordered state. It is conceivable that, near the transition temperature, three-dimensional disorder could couple to (and reduce the value of) the antiphase excitation gap, resulting in an increase of the number of antiphase boundaries.

This analysis may explain the depression of the transition temperatures found in Monte Carlo methods relative to CVM results. The appearance of antiphase boundaries near the order-disorder transition may be interpreted as complete disorder, resulting in the observed depression. Furthermore the relative depression of the transition temperature would be largest near the triple point because of the further reduction in the effective value of γ due to the magnetic-field dependence. This is the observed behavior (figure 2.9).

The role of in-plane direct correlations in the Ising system, which are completely

neglected in the model developed here, must be evaluated more carefully. In the Ising model, a large number of excitations in a plane can result in a plane which is "anti-phased". Hence, antiphase boundaries could arise from this mechanism.

E. Conclusion

The model developed and solved here is a considerably simplified version of the nearest-neighbor *fcc* Ising antiferromagnet which mimics its ground state properties. The model provides a unique insight into some of the characteristics of the more complicated Ising system.

The simplified model is analyzed for consistency with the predictions of Slawny. As Slawny conjectured, the "true" thermodynamic ground states of the three- and two-dimensional versions of this system are in fact the states with the largest number of low-lying excitations -- the ordered states without antiphase boundaries. Furthermore, in the thermodynamic limit, antiphase boundaries have zero concentration at any finite temperature, because, at finite temperatures, the excitation energy of an antiphase boundary scales with n^2, where n^3 is the number of sites, and the entropy scales as n.

In the (mathematically defined) one-dimensional system, antiphase boundaries do appear. Their concentration at zero and infinite temperatures is equal to one half, and is less than one half at intermediate temperatures. There is a range of temperatures for which *increasing* the temperature results in a *more ordered* antiphase structure. The degree to which the system orders is determined by the antiphase excitation gap, $2\gamma\varepsilon$. Larger degrees of order correspond to larger values of γ.

The behavior of the model for systems with sizes on the order of those used in the Monte Carlo calculations was investigated. It was found that for all finite-sized d-dimensional systems antiphase boundaries will appear *at equilibrium with nonzero concentration*. The antiphase boundaries are more likely to appear in smaller systems, and systems in which the antiphase excitation gap is small.

The model can be used to infer properties of the more complicated nearest-neighbor *fcc* Ising antiferromagnet and, additionally, suggests a possible resolution of the discrepancies between Monte Carlo and CVM results. In the nearest-neighbor *fcc* Ising antiferromagnet, the effective antiphase excitation gap is magnetic-field dependent. As the triple-point field is approached, the gap decreases, and antiphase boundaries appear in the Monte Carlo calculations. Furthermore, as the planes become more and more disordered, the effective energy cost of a nonzero temperature antiphase boundary may decrease. It is then possible that near the transition temperature, the concentration of antiphase boundaries might rapidly increase (for finite-sized systems). Since the order-disorder transition is known to be first order, it is unlikely that the energy cost per unit area of an antiphase boundary can ever be identically zero for the infinite system at finite temperature below the transition, and antiphase boundaries most likely do not appear.

The role of in-plane direct correlations in the Ising model needs to be assessed more carefully. The chance that a significant number of excitations can "create" an antiphase boundary leaves open the possibility that the boundaries may be stable in the infinite three-dimensional Ising system. The density of excitations required for the "creation" of an antiphase boundary is quite high. This information, combined with the knowledge that the phase transition is first-order, suggests that the nearest-neighbor *fcc* Ising model completely disorders before an antiphase boundary is "created". It is therefore plausible that complete {001} antiphase boundaries do not appear in the true equilibrium phase diagram of the nearest-neighbor *fcc* Ising antiferromagnet.

F. References for Chapter II

1 R. Kikuchi, Progress of Theor. Physics Suppl. 87 , 69 (1986).

2 C. Domb, Advanc. Phys. 9 , 150 (1960).

3 M. F. Sykes, J. W. Essam, B. R. Heap and B. J. Hiley, J. Math. Phys. 7 , 1557 (1966).

4 J. L. Lebowitz, M. K. Phani and D. F. Styer, J. Stat. Phys. 38 , 413 (1985).

5 R. Kikuchi, Phys. Rev. 81 , 988 (1951).

6 W. Shockley, J. Chem. Phys. 6 , 130 (1938).

7 H. A. Bethe, Proc. Roy. Soc. A150 , 552 (1935).

8 J. M. Ziman, *Models of Disorder* (Cambridge University Press, London, 1979).

9 J. A. Barker, Proc. Roy. Soc. A216 , 45 (1953).

10 Some CVM calculations calculate the properties of an isolated antiphase boundary, see, for example, R. Kikuchi and J. W. Cahn, Acta. Metall. 27 , 1337 (9179).

11 For a nice review of the alloy problem see D. de Fontaine, in *Solid State Physics,* edited by F. Seitz, D. Turnbull, and H. Ehrenreich (Academic, New York, 1979), Vol. 34, p. 73.

12 P. Turchi, M. Sluiter, and D. de Fontaine, Phys. Rev. B 36 , 3161 (1987).

13 A. Reich and L. M. Falicov, Phys. Rev. B 36 , 3117 (1987).

14 K. Terakura, T. Oguchi, T. Mohri, and K. Watanabe, Phys. Rev. B 35 , 2169 (1987).

15 H. Sato and R. S. Toth, Phys. Rev. 124 , 1833 (1961).

16 H. Sato and R. S. Toth, Phys. Rev. 127 , 469 (1962).

17 R. H. Fowler and E. A. Guggenheim, Proc. Roy. Soc. (London), A174 , 189 (1940).

18 C. M. van Baal, Physica 64 , 571 (1974).

19 R. Kikuchi, J. Chem. Phys. 60 , 1071 (1974).

20 N. S. Golosov, L. E. Popov, and L. Ya. Pudan, J. Phys. Chem. Solids 34 , 1149 and 1157 (1973).

21 D. de Fontaine and R. Kikuchi, Nat. Bur. Stand. (U.S.), Report No. SP-496, 1978, p. 999.

22 K. Binder, Phys. Rev. Lett. 45 , 811 (1980).

23 M. K. Phani, J. L. Lebowitz, and M. H. Kalos, Phys. Rev. B 21 , 4027 (1980).

24 A. Finel and F. Ducastelle, Europhys. Lett. 1 , 135 (1986).

25 U. Gahn, J. Phys. Chem. Solids, 47 , 1153 (1986).

26 H. T. Diep, A. Ghazali, B. Berge, and P. Lallemand, Europhys. Lett. 2 , 603 (1986).

27 H. Ackermann, S. Crusius, and G. Inden, Acta Metallurgica 34 , 2311 (1986).

28 R. Kikuchi and H. Sato, Acta Metallurgica 22 , 1099 (1974).

29 J. Slawny, J. Stat. Phys.. 20 , 711 (1979).

30 S. A. Pirogov and Ya G. Sinai, Teor. Math. Fiz. 25 , 358 (1975); 26 , 61 (1976).

31 N. D. Mackenzie and A. P. Young, J. Phys. C 14 , 3927 (1981).

32 The excitations of the nearest-neighbor *fcc* Ising antiferromagnet form a discrete energy spectrum. A third-level excitation is then defined as any excitation which has the third lowest excitation energy.

33 A. Danielian, Physical Review 133 , A1344 (1964).

34 This increase in excitation energy does not go uncompensated. Clusters with a higher excitation energy decrease it in the presence of an antiphase boundary. The cluster of four atoms all of the same spin and in the same configuration as that of figure 2 (1-2-1) has, in the perfect $L1_0$ structure, an excitation energy of

$(48J \pm 8h)$; in the "faulted" structure, with three spins up and one spin down, the excitation energy reduces to $(32J \pm 4h)$. This excitation, however, is much higher in energy than the one corresponding to the cluster considered in the text and influences the thermodynamics at higher temperatures. The changes in energy, on the other hand, exactly compensate each other.

35 Differences in the excitation spectra of the states of the model first appear at the second level of excitation, not the third. The physics of the one-dimensional aspect of the *fcc* Ising antiferromagnet is still accurately represented by the model: it has an infinite number of states in the ground-state manifold which differ only in their excitation spectra.

36 Antiphase boundaries naturally appear for the case in which $x_k = 1$. Physically, this corresponds to all states in the ground-state manifold having identical excitation spectra. Hence for this case, one clearly needs to include all possible configurations in the low-temperature expansion for the partition function. The contribution of the antiphase boundaries, however, is thermodynamically negligible, and the concentration of antiphase boundaries is one half for all temperatures.

37 From the calculations presented here, it seems plausible that antiphase boundaries would appear in Monte Carlo systems even for systems with very small next-nearest-neighbor interactions, and one would not expect any kind of discontinuous behavior in the Monte Carlo results as the next-nearest-neighbor interaction is allowed to go to zero. There is also some question concerning the role of the superdegenerate point in the phase diagram. There does not seem to be any evidence for a disordered-type phase stemming from this point in the phase diagram. Rather, the phase diagram seems to contain only the $L1_0$, $L1_2$, and the disordered phases. See reference 4 for more details.

G. Figures for Chapter II

Figure 2.1 Two possible completely random configurations of four of the six bonds at a site of the simple cubic lattice. The dark circles refer to up spins and the light circles to down spins. The structure in (a) is not physical as it requires the central site to be pointing both up and down. The structure in (b) is physically consistent. The cluster variation method proceeds by calculating all the possible arrangements of bonds on the lattice, even the ones that are not physically permissible [i.e. arrangements similar to that pictured in structure (a)] and then corrects that number (which is too large) by multiplying by the fraction of all those states that are physically allowed. The fraction of allowed states is approximated by counting the number of ways to arrange zN spins over the N sites of the lattice (where z is the coordination number) with z per site so that all z spins at each site are pointing in the same direction, and dividing that result by the total number of configurations of zN spins over the N sites of the lattice, including those that are not physically allowed.

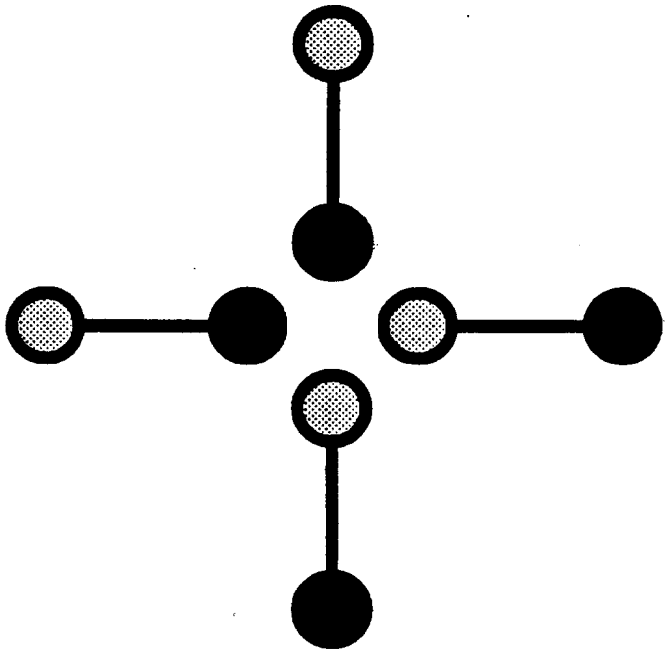

(a)

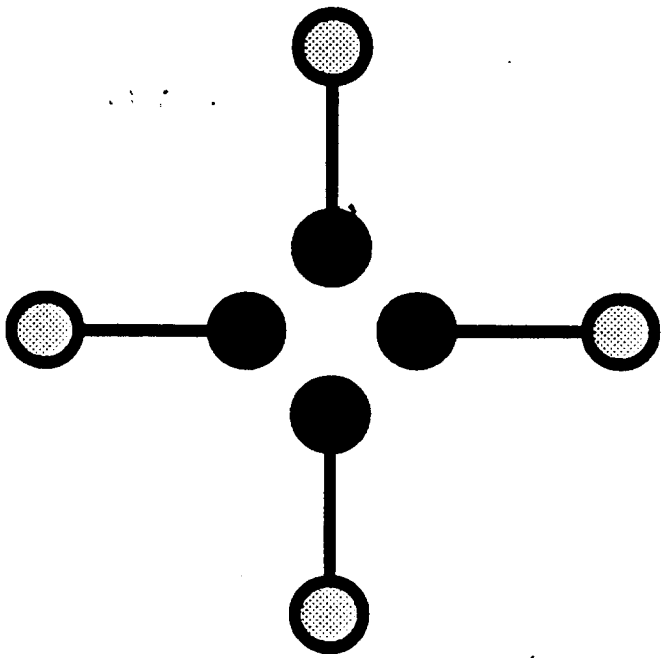

(b)

figure 2.1

Figure 2.2 The three ordered phases which appear in the phase diagram of the nearest-neighbor face-centered-cubic Ising antiferromagnet. Each cube shows a small section of three (001) planes. Dark symbols represent lattice sites that have spins pointing mostly up, and the lighter circles are lattice sites with spins that point mostly down. The phase (a) is completely disordered; all sublattices are equivalent and may have most of their spins pointing either up or down (in a nonzero external magnetic field), or there may be equal numbers of up and down spins. Phase (b) is the $L1_0$ (AB) phase. This phase has two sublattices in which the spins are pointing mostly down, and two sublattices in which the spins are pointing mostly up. Structure (c) is the $L1_2$ (A_3B) phase. In this phase, three sublattices have their spins pointing mostly up and one sublattice has its spins pointing mostly down (up is in the direction of the external field).

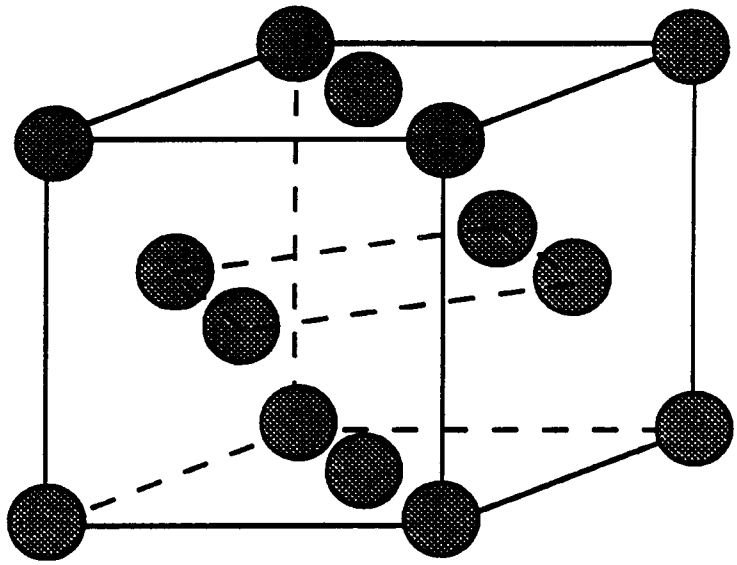

(a)

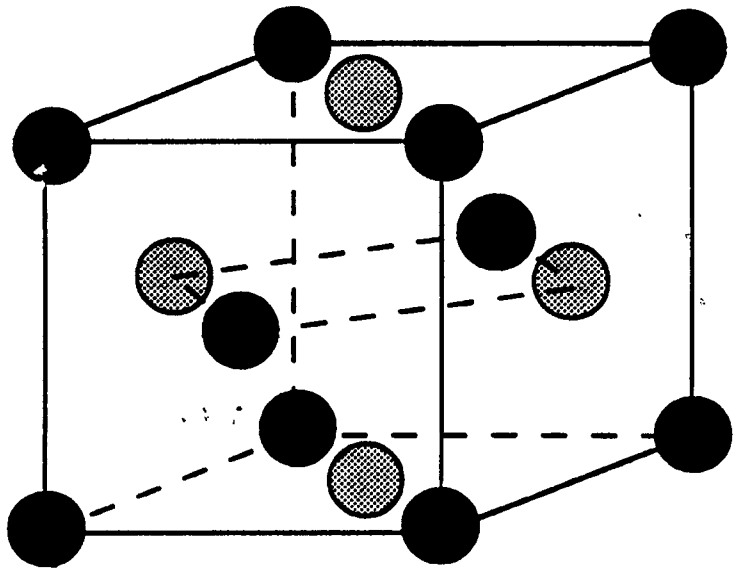

(b)

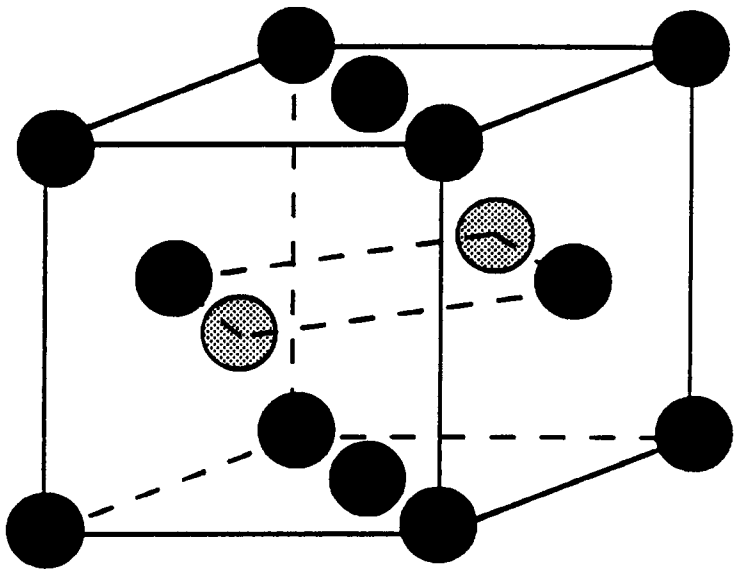

(c)

figure 2.2

Figure 2.3 The four possible (001) planes of the perfectly ordered $h = 0$, $T = 0$, *fcc* Ising antiferromagnet. Each dark (light) symbol represents an up (down) spin. The planes labelled Ba and Bb are the configurations produced by placing planes a and b, respectively, on top of plane B. The dashed boxes contain one of the nearest-neighbor tetrahedra which compose the *fcc* lattice. Each of these tetrahedra is in the minimal energy configuration, containing two up spins and two down spins. The planes can be stacked in any order: (...ZzZzZzZz...), where each Z (z) is a plane of type A (a) or B (b), and the energy is still minimal.

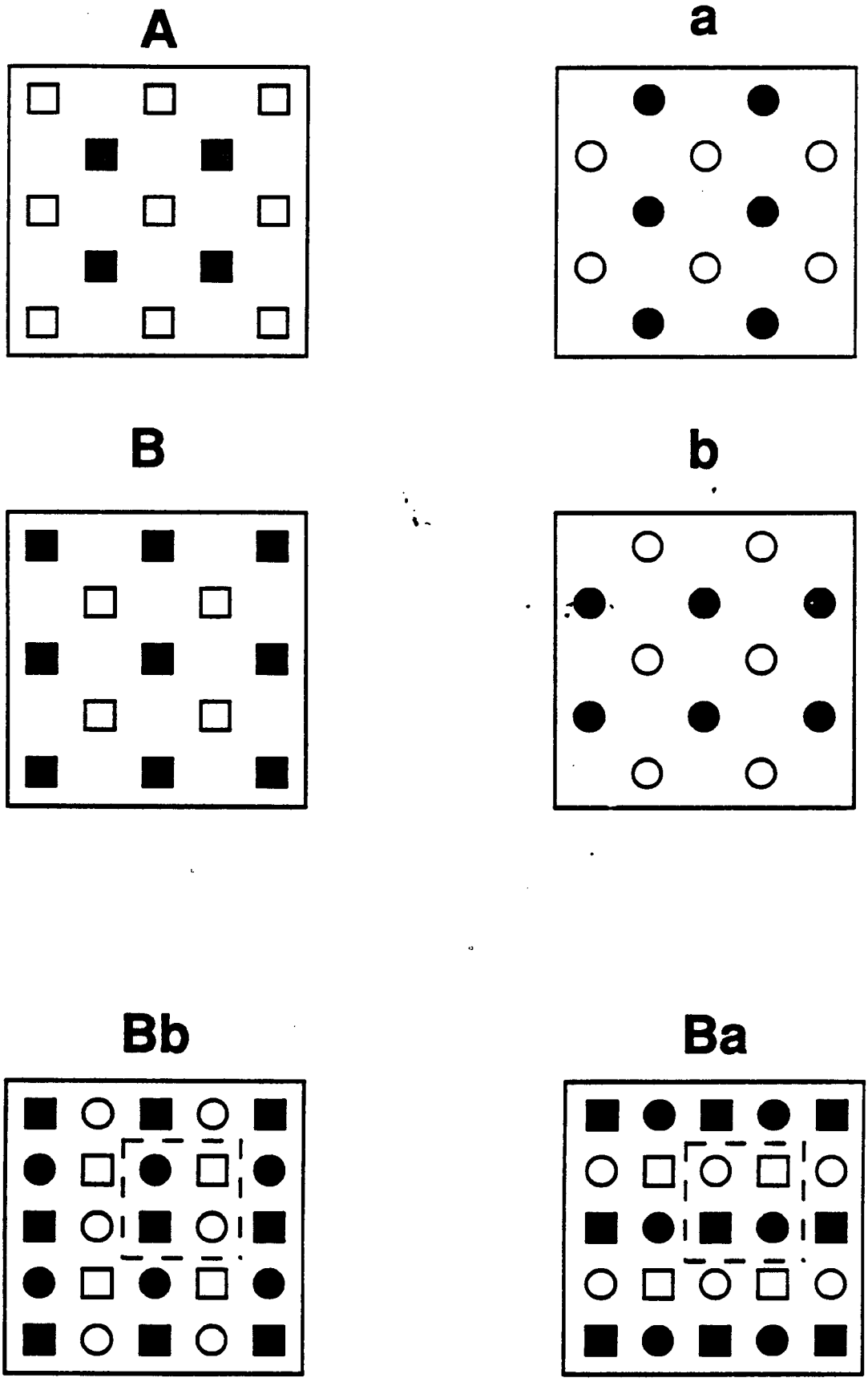

figure 2.3

Figure 2.4 The four-site connected clusters which distinguish between the states in the ground-state manifold of the *fcc* Ising antiferromagnet. The lines represent nearest-neighbor bonds. The planes are labelled as in figure 2.3. The cluster in *(i)* contains one site from the upper plane which is type A, two sites from the central plane which is type a, and one site from the lower plane, also of type A. The energy associated with flipping all four spins in this cluster is $16J$. The cluster in *(ii)* contains one site from the upper plane which is type A, two sites from the central plane which is type a, and one site from the lower plane which is type B. This type of cluster exists (at zero temperature) only at an antiphase boundary. The energy associated with flipping these spins is $(32J \pm 4h)$ where the sign is chosen to reflect the orientation of the external magnetic field. The result of one antiphase boundary is to replace n^2 clusters of type *(i)* with clusters of type *(ii)* which clearly alters the excitation spectrum of the system.

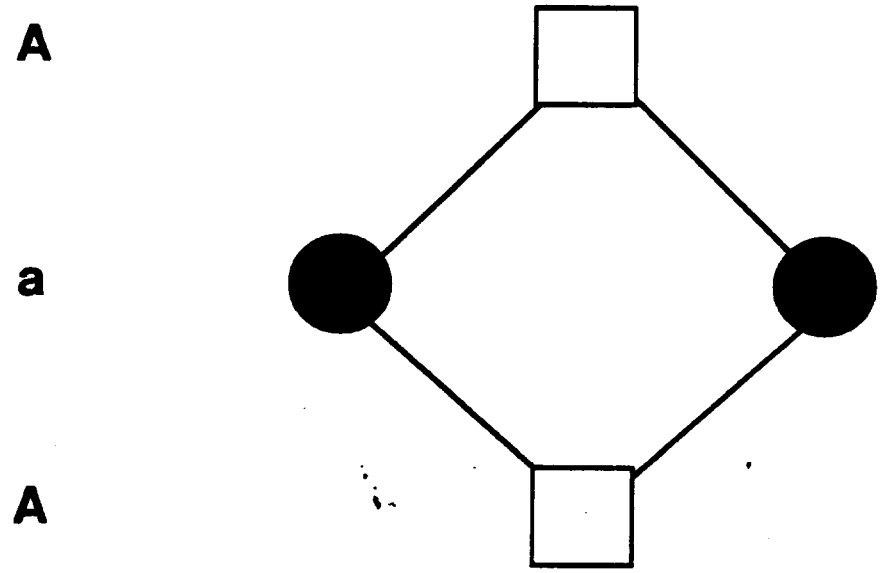

(i)

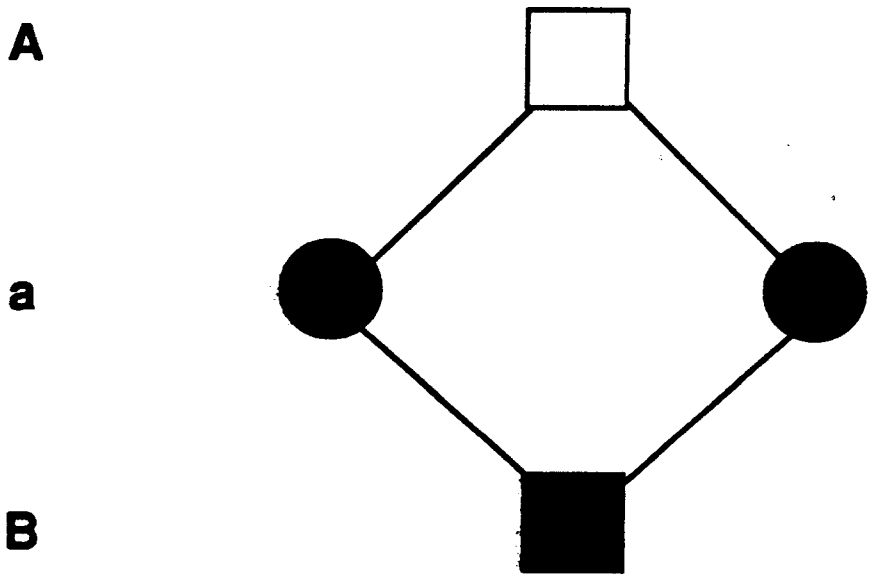

(ii)

figure 2.4

Figure 2.5 The dimensionless heat capacity per site, $\partial u/\partial\tau$, where u is the internal energy and $\tau = \beta^{-1}$, for a three-dimensional system for both correlated and uncorrelated systems plotted versus β. The correlated system has parameters $\gamma_0 = 0.7$ and $\gamma = 0.2$ While the correlated system is considerably more complex than the collection of non-interacting two-state systems, the heat capacity still displays the characteristic Schottky anomaly.

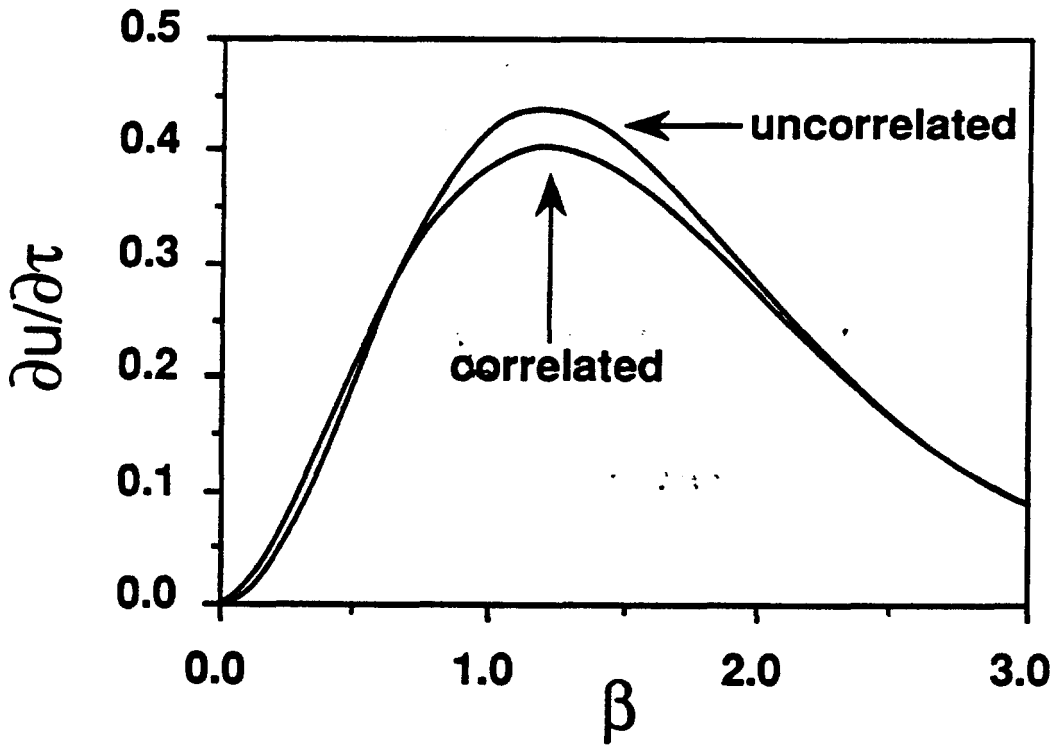

figure 2.5

Figure 2.6 The concentration of antiphase boundaries plotted as a function of $\beta\varepsilon/(1 + \beta\varepsilon)$ for the one-dimensional system for three values of the parameters: (a) $\gamma_0 = 0.8$ and $\gamma = 0.1$; (b) $\gamma_0 = 0.8$ and $\gamma = 0.3$; and (c) $\gamma_0 = 0.8$ and $\gamma = 0.6$. The abscissae are zero at $\beta = 0$ and one at $\beta = \infty$. [Antiphase boundaries are defined mathematically in one dimension by putting $d = 1$ in expression (2.6).] The curves display a minimum in the concentration of antiphase boundaries at some intermediate temperature. For some range of temperatures, the antiphase structure actually becomes *more ordered* as the temperature is *increased*. The depth of the minimum is strongly dependent on the antiphase excitation gap, $2\gamma\varepsilon$, which determines the energy difference between excitations involving an antiphase boundary and those which do not. The minimum is deeper for the larger values of γ.

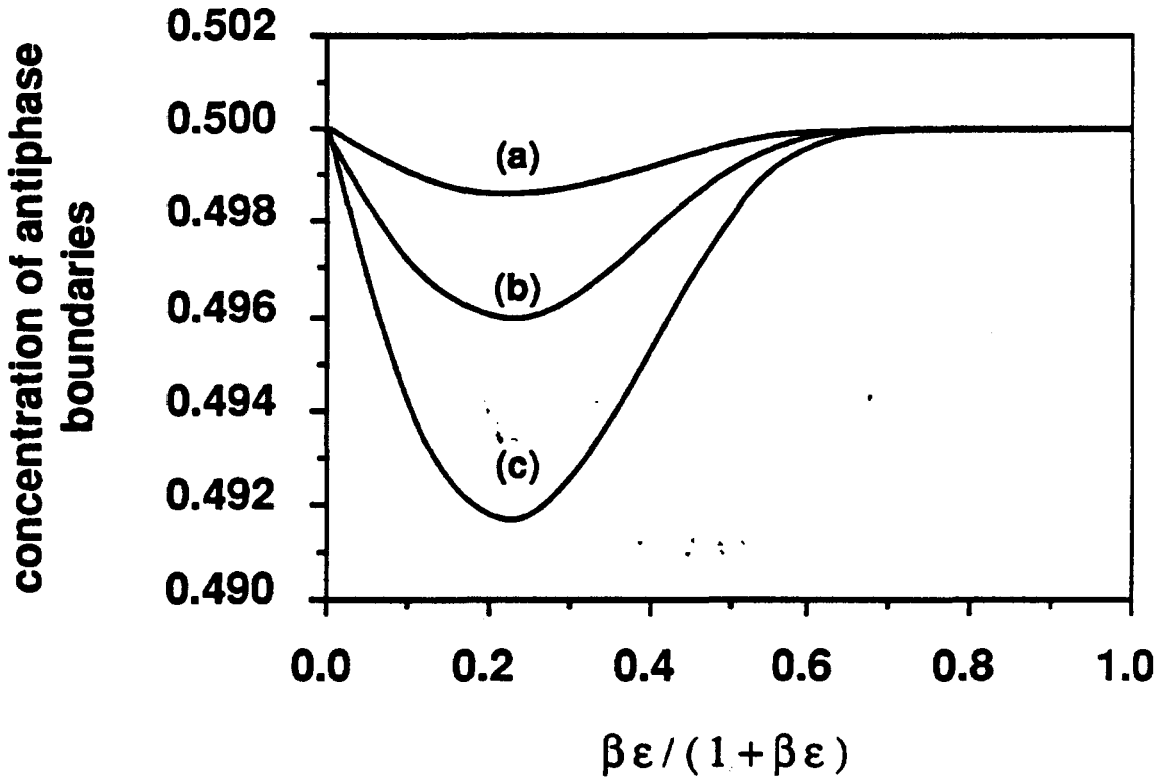
concentration of antiphase boundaries
0.502
0.500
0.498
0.496
0.494
0.492
0.490
(a)
(b)
(c)
0.0
0.2
0.4
0.6
0.8
1.0
βε/(1+βε)

figure 2.6

Figure 2.7 The concentration of antiphase boundaries plotted as a function of $\beta\varepsilon/(1 + \beta\varepsilon)$ for three-dimensional systems of finite size n^3 for $\gamma_0 = 0.5$ and $\gamma = 0.2$. The abscissae are zero at $\beta = 0$ and one at $\beta = \infty$. The curves all display a minimum in the concentration of antiphase boundaries at some intermediate temperature. The depth of the minimum is strongly dependent on the size of the sample and is deeper for larger samples. The depth of the minimum also depends on γ.

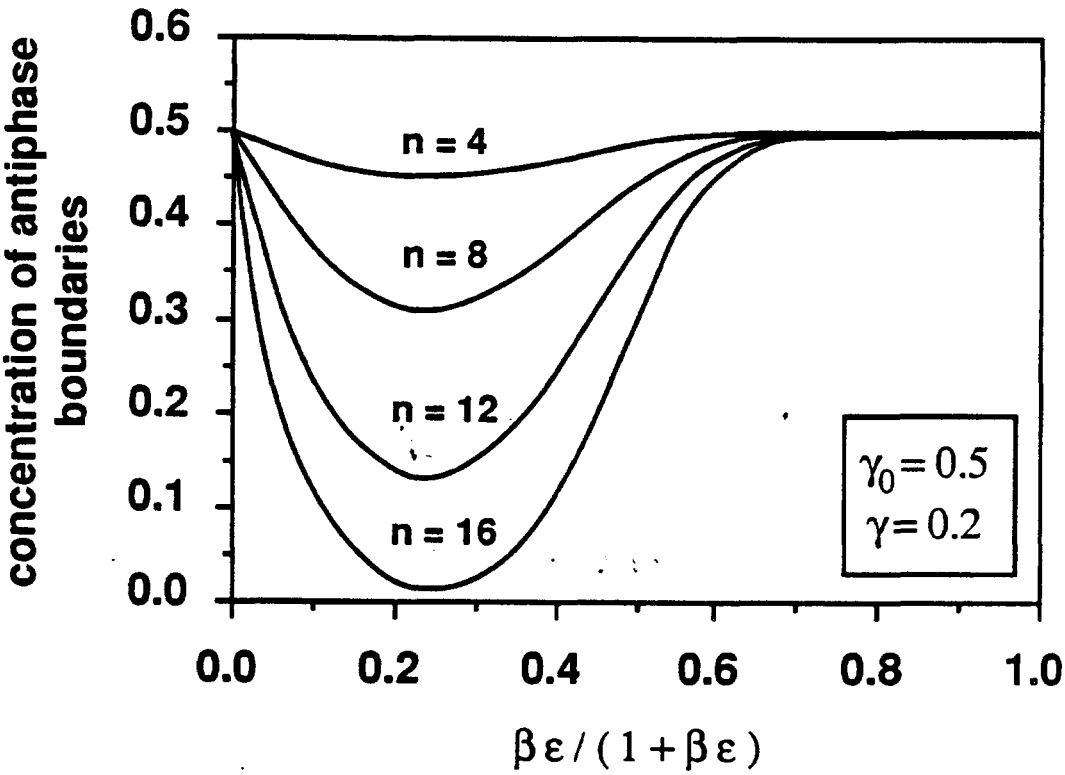
concentration of antiphase boundaries
0.6
0.5
0.4
0.3
0.2
0.1
0.0
n = 4
n = 8
n = 12
n = 16
$\gamma_0 = 0.5$
$\gamma = 0.2$
0.0
0.2
0.4
0.6
0.8
1.0
$\beta\varepsilon / (1 + \beta\varepsilon)$

figure 2.7

Figure 2.8 The concentration of antiphase boundaries plotted as a function of $\beta\varepsilon/(1 + \beta\varepsilon)$ for three-dimensional systems of finite size n^3 for $\gamma_0 = 0.8$ and $\gamma = 0.6$. The abscissae are zero at $\beta = 0$ and one at $\beta = \infty$. The curves display a minimum in the concentration of antiphase boundaries at some intermediate temperature. The depth of the minimum is strongly dependent on the size of the sample. The minima of the curves are deeper in this plot than they are for their counterparts in figure 2.7 because of the larger value of γ. The $n = 16$ case displays a considerable range of temperature for which the concentration of antiphase boundaries is numerically negligible. In the thermodynamic limit, $n \rightarrow \infty$, the concentration of antiphase boundaries is zero over the entire range of β (except the endpoints $\beta = 0$ and $\beta = \infty$).

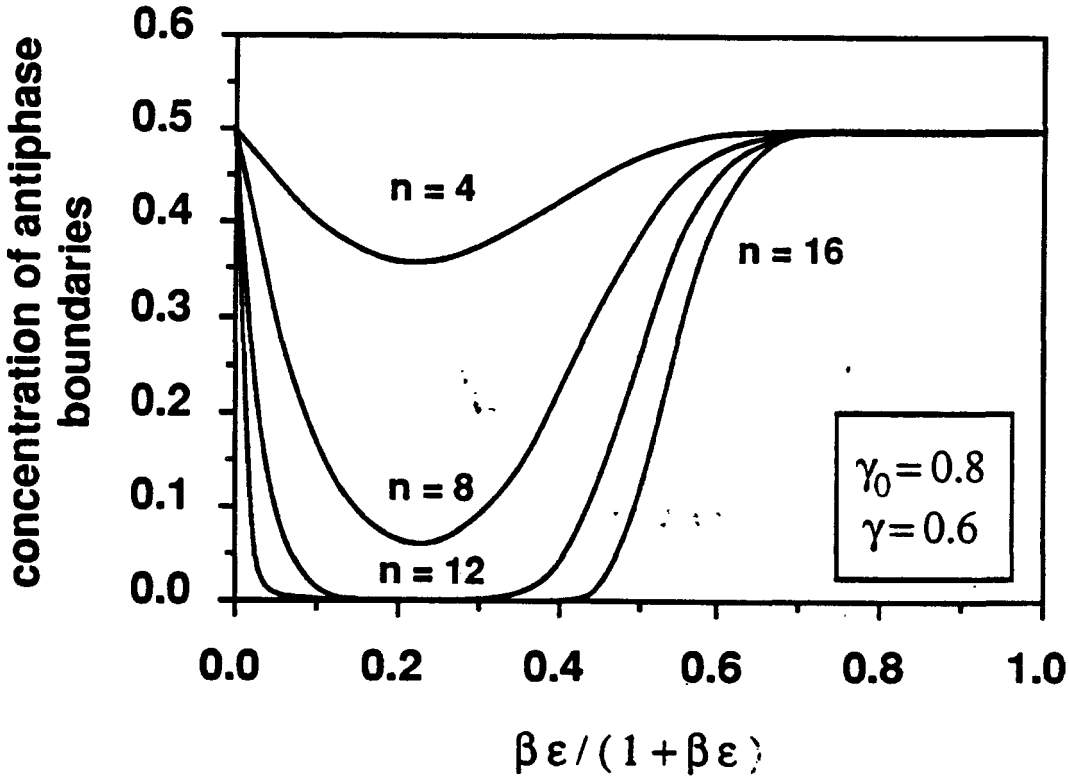
concentration of antiphase boundaries
0.6
0.5
0.4
0.3
0.2
0.1
0.0
n = 4
n = 16
n = 8
n = 12
$\gamma_0 = 0.8$
$\gamma = 0.6$
0.0
0.2
0.4
0.6
0.8
1.0
$\beta\varepsilon/(1+\beta\varepsilon)$

figure 2.8

Figure 2.9 The equilibrium phase diagrams of the nearest-neighbor *fcc* Ising antiferromagnet predicted by the CVM[24] (dashed line) and Monte Carlo[26] (solid line) methods. The transition temperature predicted by the Monte Carlo results is depressed relative to those predicted by CVM. The model constructed here suggests that the Monte Carlo results are influenced by the presence of antiphase boundaries which do not appear in an infinite system.

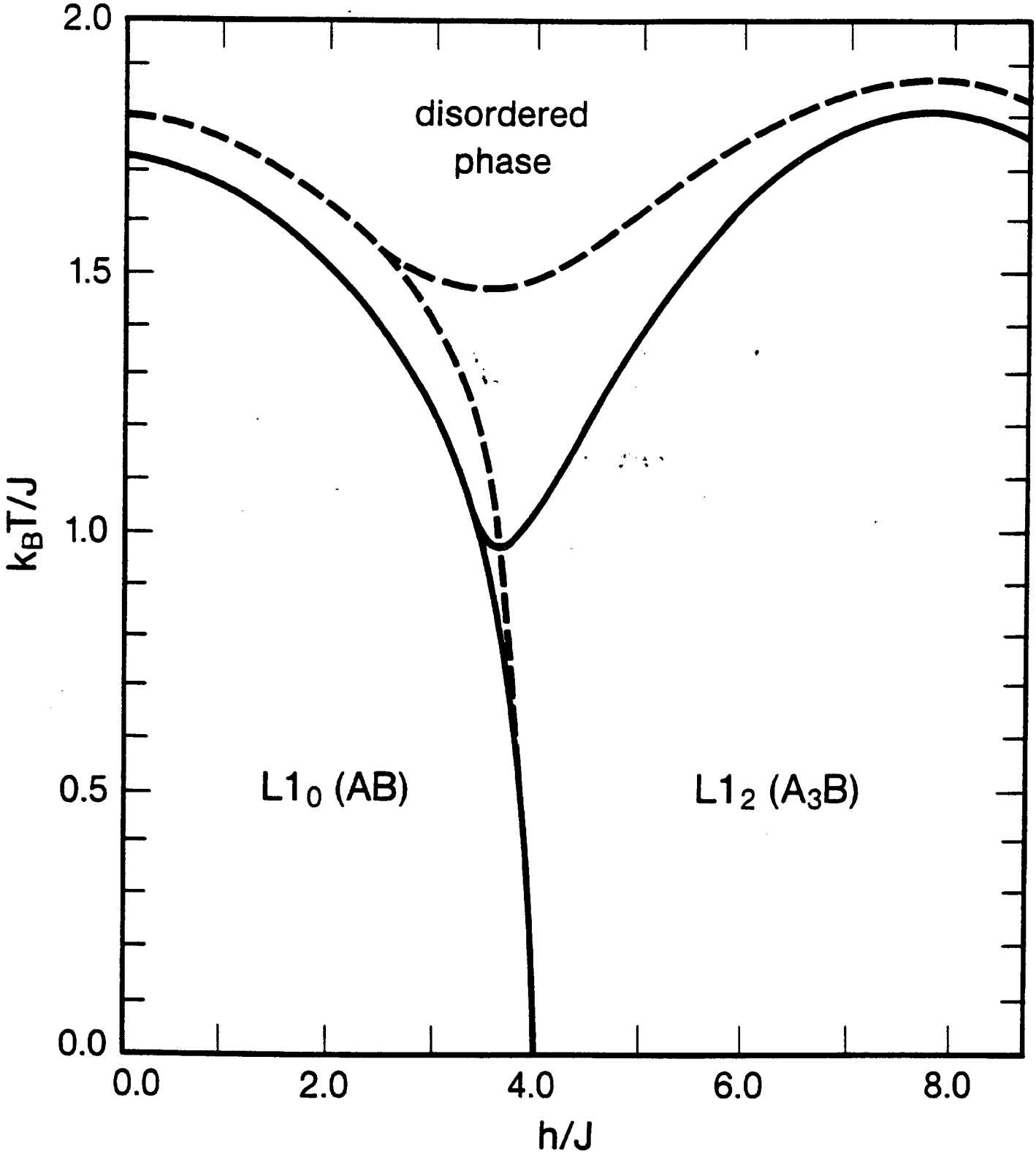
2.0
1.5
1.0
0.5
0.0
k_BT/J
disordered
phase
$L1_0$ (AB)
$L1_2$ (A_3B)
0.0
2.0
4.0
6.0
8.0
h/J

Figure 2.9

Chapter III : Magnetic Structure of the Surface of EuTe

A. Introduction

Recent low-energy-electron-diffraction experiments, performed by V. A. Grazhulis *et al.*[1] revealed a complex magnetic structure for the (001) surface of EuTe, which included periodic structures incommensurable with the underlying lattice. Furthermore, the periodicity of the magnetic structure changed as the temperature varied.

This is a surprising result. Incommensurable structures are usually the result of Fermi-surface effects[2–4]; the incommensurable structure arises from a Fermi-surface instability as in the case of a charge-density wave. The periodicity of the structure is related to the distance which spans the Fermi surface (i.e. $-\mathbf{k}_F$ to $\mathbf{k}_F$) and there is no *a priori* reason to expect this length scale to be commensurable with the underlying lattice. (A distortion with a wavelength of $2k_F$ opens a gap at the Fermi level, thus lowering the energy.) EuTe, a semiconductor, has no Fermi surface. The stability of incommensurable structures in this system appears somewhat puzzling.

Solving the puzzle requires an understanding of magnetic interactions responsible for the behavior of the bulk. EuTe crystallizes in the rock-salt structure. Its magnetism results from the strongly localized $4f$-electrons of the Eu atoms; the net spin on each site is 7/2.

Since the spins are well localized, the Heisenberg Hamiltonian discussed in chapter I models the magnetism of this compound. There are three exchange interactions which, when taken together, determine the stable magnetic phases of bulk EuTe. The exchange interactions described below can all be derived from a single Hamiltonian[5], so the separation into three distinct types, although customary, is somewhat misleading. The three exchange interactions are actually special cases of the more general exchange process. (There are other interactions which may be important for the stability of certain magnetic structures: the dipole-dipole interaction[6], which can be

included in the effective exchange interactions, and the anisotropy energy, which is neglected in the following calculation.)

The first is the direct exchange between nearest-neighbor Eu spins. This interaction's strength depends on the direct overlap of the wavefunctions of two sites. Since the Eu 4-*f* wavefunctions are very localized, this overlap is quite small, as is the resulting exchange.

Superexchange, first described by Kramers[7] and later by Anderson[8], essentially determines the magnetic properties of bulk EuTe. In the rock-salt structure of EuTe, each Eu spin couples to its next-nearest-neighbor Eu spins through the *p*-orbitals of a Te atom. The ions are arranged collinearly, Eu-Te-Eu. The superexchange is mediated by the filled *p*-shell of the Te anion as shown in figure 3.1. The first step in this process involves the hopping of one of the *p*-shell electrons onto a neighboring cation [figure 3.1(a)]. In the second step, a direct exchange between the remaining anion electron and an electron on the other cation adjacent to that anion takes place [figure 3.1(b)]. The final step is the return of an electron from the doubly occupied cation [figure 3.1(c)] to the anion. In the final state, the cation spins have been exchanged.

Superexchange only connects spins aligned antiferromagnetically, and, since the process appears in second-order perturbation theory, always results in a decrease in energy. The mediation of superexchange by the *p*-orbitals of the anion, implies sensitivity to the arrangement of the cation-anion-cation system. Superexchange only contributes significantly when the three ions are collinear and connected by a single *p*-orbital.[9] Hence nearest-neighbor spins in EuTe do not interact via superexchange (here, nearest-neighbor refers to only the atomic sites with spins, the Eu atoms, and does not include the spinless sites, the Te atoms).

The stable magnetic structure resulting from this interaction is that shown in figure 3.2. In this arrangement, each spin aligns antiferromagnetically with its six next-nearest-neighbor spins, thus minimizing the superexchange energy. This is the

observed magnetic structure[10] of NiO, MnO, FeO, and EuTe.

Another exchange mechanism plays a role in determining the magnetic structure of EuTe. In order for the direct- and super-exchanges to take place, the Wannier states on the two sites must overlap directly, or with a common anion. In systems composed of localized spins embedded in a "sea" of conduction electrons, the magnetic interaction can be mediated via the non-magnetic "sea." The conduction-band electrons "feel" the spin orientation of the $4f$ -electrons at one site, and are in a configuration reflecting this orientation. The $4f$ -electrons at another site can then sense the orientation of the original site's spin through the configuration of the conduction electrons. This mechanism, first suggested by Ruderman and Kittel[11] as an explanation for the coupling between nuclear moments in a metal, is referred to as the indirect exchange interaction. The Hamiltonian is still of the Heisenberg form but now, for a free-electron gas, the effective exchange constant appears as

$$J_{ij}^{ind} \propto -J_{eff}^2 \left[\frac{\sin 2k_F R_{ij} - 2k_F R_{ij} \cos 2k_F R_{ij}}{(2k_F R_{ij})^4} \right]$$

where J_{eff} is the exchange constant for the $4f$ -electron conduction-electron exchange, k_F is the magnitude of the Fermi wavevector of the metal, and R_{ij} is the distance between the rare earth metal sites i and j. This long-ranged interaction, which can be ferromagnetic or antiferromagnetic, depending on R_{ij}, decreases only as $1/R_{ij}^3$. It has been applied to the study of rare-earth magnetism[12], nuclear magnetism[11], and even spin glasses[13].

As mentioned above, EuTe is a semiconductor which implies that there are only a small number of conduction electrons. The indirect exchange interaction can still be important; electrons, virtually excited into the conduction band, can mediate the indirect exchange. One expects this interaction to be very sensitive to the structure of the electronic states above the Fermi level.

The exchange interactions important in the bulk are also important near the surface, and are probably related to the stabilization of the incommensurable magnetic structures. Other possibilities, however, do exist. For example, a rotational magnetic field or incommensurable potential would stabilize the incommensurable structures, but both of these options seem artificial. It is argued below that the incommensurable magnetic structures arise naturally from the competition between nearest-neighbor exchange and the antiferromagnetic next-nearest-neighbor exchange involving spins near the surface. (The anisotropy energy of the spins is neglected in this argument. While it is possible that this energy plays a role in stabilizing the incommensurable structures, it is shown below that this contribution is not necessary. It also seems unlikely that anisotropy would destabilize the incommensurable structures.)

Some evidence suggests that competing interactions may be responsible for the stability of the incommensurable structure. Table 3.1 contains the experimentally[14] derived exchange constants (for both nearest- and next-nearest-neighbor exchange interactions) and the critical temperatures for the europium monochalcogenides. In table 3.1, J_{nn} is the net nearest-neighbor exchange and J_{nnn} is the net next-nearest-neighbor exchange interaction. The critical temperature is either the Curie point or the Néel temperature, depending on whether the system is ferromagnetic or antiferromagnetic. The reported critical temperature for EuTe is only approximate.

Perhaps the most interesting feature of table 3.1 is the double entry for EuSe. This compound is ferromagnetic below 2.8 K and antiferromagnetic between 2.8 K and 4.6 K. Thus the system undergoes a transition from a ferromagnetic state to an antiferromagnetic state. The only magnetic system, of which the author is aware, which displays the same type of behavior without the influence of an external field is the Axial-Next-Nearest-Neighbor-Ising (ANNNI)[15] model, in which competing exchange interactions result in long-period magnetic structures with a temperature dependent periodicity. Table 3.1 also indicates a trend in the net exchange energies. As one

moves down the periodic table from O to Te, the next-nearest-neighbor exchange in EuX (where X is O, S, Se or Te) grows and the nearest-neighbor exchange decreases. At the point where the two exchange constants are nearly equal, EuSe, the transition from a ferromagnetic state to the antiferromagnetic state is observed. (It should be noted that this argument is somewhat circular; the exchange integrals are calculated from experimental data within the Heisenberg theory and are not measured directly, indicating that this observation is merely self-consistent.) EuTe is an antiferromagnet, as indicated in table 3.1, but subtle electronic changes could shift it into the ferromagnetic regime.

In addition to the thermodynamic effects of change in temperature, the exchange integrals themselves could be temperature dependent. For example, changes in temperature will alter the occupation of the conduction band, thus affecting the exchange integrals. A small change in exchange integrals could result in a large change in periodicity. The presence of the surface is sure to alter the values of the exchange interactions involving spins near the surface, either directly through the change in symmetry and its effects on the electronic structure near the surface, or indirectly, through buckling, thermal expansion, or some other surface effect. Furthermore, these changes in the exchange interactions near the surface are likely to depend sensitively on the temperature, thus creating a temperature dependent periodicity.

It will be shown below that competing exchange interactions are capable of producing complex, incommensurable magnetic structures on the surface of EuTe. The proposed model Hamiltonian is the simple Heisenberg Hamiltonian discussed in chapter I, suitably adapted for use near a surface. The incommensurable magnetic structures are demonstrated to be stable for a wide range of the exchange interactions, and are predicted to be clearly visible in low-energy-electron-diffraction experiments.

The surfaces of the europium monochalcogenides and similar compounds are expected to display anomalous magnetic properties.[16] For example, Castiel[17] calculated

the surface magnons of the unreconstructed {001} and {111} surfaces of the EuX ferromagnets. His calculation predicted soft magnons on both surfaces, demonstrating their tendency to reconstruct magnetically. The calculation involved only normal modes, however, and no attempt was made to calculate the actual ground-state spin structure.

Experimentally, techniques which probe the surface magnetic structure either directly, such as low-energy electron diffraction (LEED),[16,18–20] and spin-polarized low-energy electron diffraction (SPLEED),[16] or indirectly, for example spin-polarized photoemission,[21–23] have provided valuable experimental results. Photoemission experiments on EuO suggest the presence of a paramagnetic sheet on its {001} surfaces.[24,25] SPLEED studies of Gd give a surface Curie point a full 22 K above the bulk value.[26] In the experiment which prompted this research,[1] Grazhulis and collaborators report the appearance of symmetry-breaking incommensurable surface spin-structures with temperature dependent wavevectors in low-temperature (≈10 K) low-energy electron diffraction studies of single-crystal EuTe {001} surfaces obtained by cleavage under ultrahigh vacuum conditions.

The calculation presented here demonstrates that the stability of the incommensurable magnetic structures on the {001} surfaces of EuTe, observed by Grazhulis and coworkers, most likely originates in the competition between relatively large surface nearest-neighbor exchanges and the second-nearest-neighbor superexchange interactions characteristic of the bulk. (This possibility has been clearly demonstrated in the ANNNI[15,27] model.) The calculation, based on a classical Heisenberg Hamiltonian at zero temperature, including all possible commensurable structures plus one class of incommensurable surface spin arrangements, yields a complex phase-stability diagram (as a function of surface exchange integrals) with regions of commensurable and incommensurable ground-state-structures. There is no need to introduce potentials incommensurable with the lattice to stabilize the incommensurable structures.[28,29]

Section B of this chapter deals with the details of the model and the calculation, section C contains the results and discussion, and section D presents the conclusions.

B. Calculations

The Eu atoms of the (001) surface of EuTe are sketched in figure 3.3. The orientation shown for the spins are those chosen for the bulk antiferromagnet.[30] Three exchange integrals enter the calculation: J, the superexchange between second-nearest neighbors throughout the crystal; K, the net exchange between nearest neighbors on the surface; and L, the net exchange between nearest neighbors where one atom is in the surface layer, and the other is in the second layer. Because only the antiferromagnets are considered, J is restricted to be positive, but K and L are allowed to have either sign. (J, K and L include contributions from the dipole-dipole interaction and the direct, indirect and superexchange processes.) Nearest-neighbor exchange in the bulk is neglected and all layers, except the two surface layers, are assumed to have the bulk antiferromagnetic configuration, which amounts to a renormalization of the exchange interactions. The model neglects anisotropy energy and all further neighbor exchanges, but retains the minimum number of interactions needed for describing the physical mechanism. The total energy is written

$$E = J \sum_{(ij)} \mathbf{S}_i \cdot \mathbf{S}_j + K \sum_{<ij>} \mathbf{S}_i \cdot \mathbf{S}_j + L \sum_{[ij]} \mathbf{S}_i \cdot \mathbf{S}_j \quad , \tag{3.1}$$

where $\mathbf{S}_i$ is a classical spin of unit magnitude fixed at site i, (ij) designates a second-nearest-neighbor pair, $<ij>$ is a nearest-neighbor pair with both spins at the surface, and $[ij]$ is a nearest-neighbor pair with one spin at the surface and one in the second layer; the sums run over an infinite half space.

Exchange interactions depend quite sensitively on a variety of parameters including pressure, doping, temperature, and proximity to a surface.[12,13,16,31] The properties of EuSe suggest that the exchange interactions in the europium monochalcogenides

may be sensitive to changes in temperature. It is possible to model this temperature dependence by varying exchange interactions at zero temperature. Additionally, the nearest-neighbor surface exchange is more sensitive to the effects of the loss of three-dimensional symmetry at the surface, as reflected in the electronic structure and the buckling of the surface, than the second-nearest-neighbor superexchange. (Table 3.1 indicates that the nearest-neighbor exchange is more sensitive to the changes in electronic structure and atomic size of the chalcogenides than the next-nearest-neighbor exchange.) This model, therefore, investigates a range of surface exchange interactions, measured relative to the bulk superexchange strength.

The two-dimensional unit cell chosen for the calculation contains four atoms from each plane. The cell, with linear dimension b, and its Brillouin zone are shown in figure 3.4. (The spins are depicted in the chosen bulk configuration.) The points Y and Y′ in the Brillouin zone are not equivalent because the spin domain structure of the bulk introduces a preferred direction on the surface.

The Eu face-centered-cubic lattice is divided into four interpenetrating simple-cubic lattices each of which is further divided into two interpenetrating face-centered-cubic lattices. Each simple-cubic sublattice is denoted by a subscript i which runs from A to D. Each face-centered-cubic sub-sublattice corresponding to a given simple-cubic sublattice is designated by the subscript μ, which is either α or β.

The trial spins have the form of a "frozen", finite-amplitude spin-wave:

$$\mathbf{S}_{i\mu}(\mathbf{R}) = x_{i\mu}\, cos(\,\mathbf{k}\cdot\mathbf{R} + \phi_{i\mu}\,)\,\hat{\mathbf{x}} + y_{i\mu}\, sin(\,\mathbf{k}\cdot\mathbf{R} + \phi_{i\mu}\,)\,\hat{\mathbf{y}} + z_{i\mu}\,\hat{\mathbf{z}} \quad , \qquad (3.2)$$

$$x_{i\mu}^2 = y_{i\mu}^2 = 1 - z_{i\mu}^2 \quad ,$$

where $\hat{\mathbf{z}}$ in a unit vector in the direction of the bulk spin quantization, $\mathbf{R}$ refers to the position of the unit cell, and $\mathbf{k}$ lies in the Brillouin zone of figure 3.4. The definition used here is such that states with $\mathbf{k} = 0$ are referred to as commensurable, and states with $\mathbf{k} \neq 0$ are called incommensurable. The trial spins have magnitude unity and

expression (3.1) is easily summed to obtain a closed expression for the energy per unit cell for all **k**, including those **k** at the zone edge.

All spins in planes below the first two layers are kept fixed:

$$x_{i\mu} = y_{i\mu} = 0 \quad , \tag{3.3a}$$

and

$$z_{i\alpha} = 1 \, , \qquad z_{i\beta} = -1 \quad . \tag{3.3b}$$

The *ansatz* (3.2) is substituted into expression (3.1), and the total energy for given values of (K/J) and (L/J) in the range $-5 \leq (K/J) \leq 5$ and $-5 \leq (L/J) \leq 5$ is minimized with respect to $x_{i\mu}$, $y_{i\mu}$, **k**, and $\phi_{i\mu}$.

C. Results and Discussion

The minimum-energy phase-stability diagram for commensurable structures (**k** = 0) is shown in figure 3.5. The contours are the energy per unit cell of the two surface layers measured in units of J. The dark lines represent phase boundaries of second or higher order: the orientations of the spins change continuously with (K/J) and (L/J).

The bulk phase (figure 3.3) is the lowest energy commensurable spin structure in region (I) of parameter space. The two surface layers of the this phase have energy per unit cell $-24\,J$.

The minimum energy commensurable spin structure in region (II) can be described analytically in terms of the parameter (K/J). The second-layer spins are in the bulk configuration [equations (3.3)], and the first layer spins are given by

$$\begin{aligned}
\mathbf{S}_{A\alpha}(\mathbf{R}) &= [\, 1 - 1/[\, 4\,(K/J) - 8\,]^2\,]^{1/2}\,\hat{\mathbf{x}} + [\, 1/[\, 4\,(K/J) - 8\,]\,]\,\hat{\mathbf{z}} \quad , \\
\mathbf{S}_{B\alpha}(\mathbf{R}) &= -[\, 1 - 1/[\, 4\,(K/J) - 8\,]^2\,]^{1/2}\,\hat{\mathbf{x}} + [\, 1/[\, 4\,(K/J) - 8\,]\,]\,\hat{\mathbf{z}} \quad , \\
\mathbf{S}_{A\beta}(\mathbf{R}) &= [\, 1 - 1/[\, 4\,(K/J) - 8\,]^2\,]^{1/2}\,\hat{\mathbf{x}} - [\, 1/[\, 4\,(K/J) - 8\,]\,]\,\hat{\mathbf{z}} \quad ,
\end{aligned} \tag{3.4}$$

$$S_{B\beta}(\mathbf{R}) = -[\ 1 - 1/[\ 4\ (K/J) - 8\ ]^2\ ]^{1/2}\ \hat{\mathbf{x}} - [\ 1/[\ 4\ (K/J) - 8\ ]\ ]\ \hat{\mathbf{z}}\quad .$$

The expression for the energy per unit cell of the two surface layers is

$$E = -8\ (K/J) - 4 - [\ 1/[2\ (K/J) - 4\ ]\ ]\quad . \tag{3.5}$$

The (I)-(II) boundary is at $(K/J) = 2.25$. As (K/J) is increased with (L/J) held constant, the spins tend more and more toward the nearest-neighbor square-antiferromagnet (NNSA) in which every surface spin is aligned exactly antiparallel to its four nearest-neighbor surface spins, and all surface spins lie in the (001) plane. The configuration of the surface spins for $(K/J) = 2.50$ is shown in figure 3.6, and table 3.2 displays the corresponding values of the variational parameters of equation (3.2). (The units and coordinate system used for **k** in this and all further tables is such that the points Y′ and Y are given by [0.000 , 0.500] and [0.500 , 0.000] respectively.)

The variational parameters for a spin configuration typical of region (III) are given in table 3.3. In this region, the spins in each of the two surface planes have their z-components aligned in the bulk configuration, and their xy-components aligned ferromagnetically. The two surface planes then align with xy-components antiparallel $[(L/J) > 0]$, or parallel $[(L/J) < 0]$. The canting of the spins in both the surface layer and the second layer depends on (L/J) and (K/J). A positive value for (K/J) should result in partial NNSA alignment of the surface spins, except when the (L/J) interaction overwhelms the (K/J) interaction, as it does in region (III). For $(K/J) < 0$, there is no competition between the two types of nearest-neighbor interactions; both interactions favor a partially ferromagnetic alignment of the surface spins.

The regions labelled (IV_a) and (IV_b) display the most complicated behavior of all the commensurable structures. Table 3.4 contains the parameters describing the stable structure at the point $(K/J) = 3.0$, $(L/J) = 4.0$. The surface layer is in a spiral-type state and the second-layer spins are aligned in a fashion similar to the second-layer spins in region (III), i.e. mostly antiparallel to the surface layer for $(L/J) > 0$ (IV_a)

and mostly parallel to the surface layer for $(L/J) < 0$ (IV_b). This configuration is the result of the "frustration" arising from the competition between (K/J) and (L/J).

The $\pm (L/J)$ symmetry of figure 3.5 is easily understood. As stated above, the nearest-neighbor interplane exchange tends to align the in-plane components of the spins in each of the two (001) planes nearest to the surface ferromagnetically. The symmetry in $\pm (L/J)$ stems from the fact that the two partially ferromagnetic surface planes can align in either of two directions: ferromagnetically or antiferromagnetically, depending on the sign of (L/J). Even though the configurations of the spins are drastically different for $\pm (L/J)$, the resulting minimum energies are identical. (This symmetry continues to hold when incommensurable structures are included in the calculation, although the configurations are considerably more complicated.)

Inclusion of incommensurable spin structures [$\mathbf{k} \neq 0$ in equation (3.2)] yields the phase-stability diagram of figure 3.7. The most notable difference from figure 3.5 is the appearance of the two shaded regions in which the structures of minimum energy are incommensurable with the underlying lattice. Because *all* commensurable structures have been included and explicitly calculated, the ground state in the shaded regions is *guaranteed* to be incommensurable. Since the trial state equation (3.2) does *not* include *all possible incommensurable structures*, the true *incommensurable* ground states may be different from the ones reported here.

The structures labelled (i), (ii), and (iii) are equivalent to those labelled (I), (II), and (III) in figure 3.5. The incommensurable structures are of two types labelled (iv) and (v). The stable structures in regions (iv) are the finite-amplitude "frozen" spin-waves, whose z–components are reminiscent of the bulk antiferromagnetic state. The structure appearing in regions (v) are also the "frozen" spin-waves, but their z–components are suggestive of a cross between the bulk-antiferromagnetic state and state similar to NNSA, but with the spins all pointing in the $\pm z$ direction instead of lying in the xy plane (z-NNSA). As in the commensurable case, the subscripts a and

b refer to the manner in which the second layer spins align themselves with the surface layer, i.e. generally antiparallel or parallel, respectively. Typical spin parameters for these two regions are given in tables 3.5, 3.6, and 3.7. Figures 3.8, 3.9, and 3.10 are the incommensurable spin structures corresponding to the parameters of tables 3.5 through 3.7 respectively. The structures in figures 3.8 and 3.9 have the same energy, even though their **k**-vectors are orthogonal to each other.

The **k**-vectors of the minimum-energy incommensurable states lie along either the line from Γ-to-Y or the line from Γ-to-Y′ (figure 3.4). By symmetry, the minimum-energy states with wavevectors ±**k** are degenerate. The structures in regions (iv) have an additional degeneracy: the minimum-energy state with wavevector on the line from Γ-to-Y is degenerate with the state with wavevector of the same magnitude on the line from Γ-to-Y′. This degeneracy is somewhat surprising given the domain asymmetry of the bulk configuration, but it can be understood as follows. The Heisenberg interactions only couple respective components of the two spins: the x-component of one spin is coupled to the x-component of another, and so on. The asymmetry of the bulk lies entirely in the z-component of the spins. Since the z-components of the spins have no **k** dependence, one might expect the Γ-to-Y and Γ-to-Y′ directions to be equivalent. This is certainly true if the z-components of all the spins in a given layer have the same magnitude, as they do in regions (iv). If, however, the z-components of a given plane are not of uniform magnitude, as in regions (v), the asymmetry of the bulk is felt through the corresponding magnitudes of the xy-components of the spins, which are also no longer uniform. These xy-components do depend directly on **k**, and so the Γ-to-Y and Γ-to-Y′ directions are not equivalent. Examination of tables 3.5 through 3.7 and figures 3.8 through 3.10 reveal that the conditions for the additional degeneracy are fulfilled in regions (iv) but not in regions (v). The interaction responsible for lifting the degeneracy in regions (v) is K, the nearest-neighbor surface interaction. The observed z-NNSA-bulk mixed state is a configuration resulting from the

compromise between a large antiferromagnetic (K/J) and the constraints imposed by equation (3.2).

The (i)-(iv) and (ii)-(v) boundaries of figure 3.7 are, in **k**-space, discontinuous transitions: **k** goes discontinuously from zero to a finite value at the boundary. The xy-amplitudes of the "frozen" spin-waves increase continuously from zero to a finite value. The (iii)-(iv) boundaries represent higher order transitions. The (iv)-(v) boundaries are even more complicated: the xy-amplitudes change continuously across the boundary, as does the magnitude of **k**, but the degeneracy goes from fourfold to twofold when crossing from regions (iv) into regions (v).

The value of **k** for the minimum energy state can be very sensitive to changes in the surface exchange integrals. Extreme sensitivity occurs in the region of parameter space thought to correspond to EuTe (i.e. antiferromagnetic second-nearest-neighbor exchange and ferromagnetic nearest-neighbor exchanges). Hence the small changes in the nearest-neighbor surface exchange expected to arise from temperature variation could generate large, experimentally observable shifts in **k**.

A notable feature of the results presented here is that the nearest-neighbor coupling between the surface and second layers is necessary for the stability of the incommensurable "frozen" spin waves. The surface-only nearest-neighbor exchange, however, is not required for their stability. The region of stability of the incommensurable structures completely covers the regions (IV) of the commensurable phase-stability diagram, as one might expect, for these are exactly the regions of parameter space in which the spins are most "frustrated".

The magnetic structure of the surface should lead to Bragg diffraction peaks of low-energy electron diffraction experiments.[20,21] The intensity of the LEED beams at wavevector **Q** due to magnetic structure is proportional to the squared magnitude of the Fourier transform of the magnetization $|\mathbf{S}(\mathbf{Q})|^2$. Since some of the magnetic structure peaks do not correspond to chemical diffraction beams, they should be

readily observed,[32] even with unpolarized electrons.

The positions of the beams diffracted by magnetic structures are designated by the vector **Q**. The magnituces of the vectors are measured in units of $[2\pi/b]$. The diffracted beams at $\mathbf{Q} = [2n\ ,\ 2m + 1]$ (n and m are integers) are those associated with the bulk-antiferromagnetic structure. The beams $\mathbf{Q} = [2n + 1\ ,\ 2m + 1]$ are associated with NNSA surface structure. The beams at $\mathbf{Q} = [2n\ ,\ 2m]$ are those associated with the chemical periodicity of the surface, and the ferromagnetic-surface structures as well. The beams due to incommensurable magnetic structure are those described by nonintegral n or m. The structure factors calculated here are those of the surface layer only, and are calculated assuming only a single "frozen" spin wave.

Figure 3.11(a) is a plot of the structure factors for nonzero diffraction beams as a function of (L/J) for $(K/J) = 0$. The spin structures used in constructing this plot all have **k** along the Γ-to-Y line, but the plot would be identical for **k** along the Γ-to-Y′ line. The solid line is the structure factor for the bulk-antiferromagnetic beams, the chain-dot line is the structure factor for the ferromagnetic beams, and the dashed line is used for NNSA-like beams. The dotted line corresponds to the beams diffracted by the incommensurable magnetic structure, which, for the choice of **k**'s used here, are located at $\mathbf{Q} = [2n\ ,\ 2m] \pm \mathbf{k}$ for $4.0 > (L/J) > 2.8$ and at $\mathbf{Q} = [2n + 1\ ,\ 2m] \pm \mathbf{k}$ for $1.414 < (L/J) < 2.8$. Figure 3.11(b) is a schematic diagram of the expected LEED pattern. Figure 3.12 plots the **k**-vectors of the incommensurable diffraction beams in figure 3.11(a). From $(L/J) = 0$ to $(L/J) = 1.414$ the surface structure is the bulk antiferromagnet. At $(L/J) = 1.414$ the surface undergoes a transition to an incommensurable state clearly shown by the jump in **k** seen in figure 3.12. It is at this value of L/J that the LEED beams arising from the incommensurable magnetic structure appear in the positions indicated in figure 3.11(b). As (L/J) increases further, more of the scattering strength is at the incommensurable peaks. Simultaneously, however, **k** approaches the Γ-point. At $(L/J) = 4.0$, the two incommensurable spots merge at the

zone center. Although in figure 3.11(a) this merging appears to be a discontinuous transition, it is not. It is the usual factor of two encountered in incommensurable-commensurable transitions. The distinct jump at $(L/J) = 4.0$ appears because for $(L/J) < 4.0$ the electrons are scattered into *two* spots with equal intensity, whereas for $(L/J) \geq 4.0$ the two peaks merge into *one* [figure 3.11(b)]. The graph in figure 3.11(a) shows the structure factor for only one of the two equivalent spots.

Figure 3.13 is a plot of the magnetic structure factors for $(L/J) = 3.00$ as a function of (K/J) for the region near the (iv_a)-(v_a) boundary. Here the **k**-vectors of the incommensurable state were chosen to lie along the Γ-to-Y′ line. The chain-dash line is the magnetic structure factor of the incommensurable diffraction beams at the points $\mathbf{Q} = [2n + 1\ ,\ 2m + 1] \pm \mathbf{k}$. The dotted line is the structure factor for incommensurable beams at $\mathbf{Q} = [2n\ ,\ 2m + 1] \pm \mathbf{k}$. The structural transition at $(K/J) = 2.56$ is clearly evident and is continuous.

Figures 3.11, 3.12 and 3.13 indicate that the LEED patterns expected from the different structures should be very sensitive to relatively small changes in surface exchange integrals. LEED experiments performed on these materials, therefore, should be able to detect magnetic structural changes experimentally induced by small changes in the surface exchange integrals.

D. Conclusion

The phase-stability diagram of the simple classical Heisenberg Hamiltonian [expression (3.1)], found with trial states of the form given by expression (3.2), is remarkably complex. It shows entire regions of parameter space in which incommensurable spin structures are the stable ground state. Since *all* commensurable structures are included in this model, the incommensurable regions of the phase-stability diagram (figure 3.7) are certain to have incommensurable ground states, which may be the "frozen" spin waves of equation (3.2), or more complex *incommensurable* structures. These incommensurable surface structures are not stabilized by Fermi-surface effects

or incommensurable potentials, but are the result of competing nearest- and second-nearest-neighbor exchange interactions. Nearest-neighbor coupling between the first and second layers seems to be necessary for the stability of the incommensurable structures.

The stable incommensurable "frozen" spin waves used in the calculation are of two basic types: one reminiscent of the bulk structure, type (iv), and one which is suggestive of a mixture of the bulk and z-NNSA structures, type (v). The fourfold degeneracy of the (iv)-type phase and the twofold degeneracy of the (v)-type phase are understood in terms of the coupling to the bulk: the xy-components of the (iv)-type phase surface spins do not feel the asymmetry of the bulk because the z-components of the spins in each layer are uniform. Differing from the properties of the (iv)-type phases, the (v)-type phases have nonuniform z-components of the surface spins and the transverse xy-components of the spins "feel" the asymmetry of the bulk (through their nonuniform magnitude) thereby lifting the degeneracy.

It is possible to choose the parameters (K/J) and (L/J) to stabilize the state of any **k**-vector along the Γ-to-Y or the Γ-to-Y′ line. In some regions of parameter space, which may also coincide with the parameters corresponding to EuTe, the k-vector of the incommensurable stable state is very sensitive to small changes in the parameters.

Since the LEED patterns of these antiferromagnets are expected to display additional diffraction beams caused by magnetic structure at the surface, the magnetic structure factors for several interesting cases were calculated. They revealed that the LEED pattern should be very sensitive to changes in surface exchange integrals. This sensitivity, expected in both location and intensity of the diffraction beams, should be easily observed.

In conclusion, it has been demonstrated that competing nearest- and next-nearest-neighbor exchange interactions involving the surface spins could be the stabilization

mechanism for the observed incommensurable structures. Difficulties inherent in the experiments and the theory, however, make direct application for the extraction of the surface exchange integrals difficult.

E. References for Chapter III

1 V. A. Grazhulis, private communication.

2 A. Werner, A. Arrott, and H. Kendrick, Phys. Rev. 155 , 528 (1967).

3 W. M. Lomer, Proc. Roy. Soc. (London) A 80 , 489 (1962).

4 L. M. Falicov and D. R. Penn, Phys. Rev. 158 , 476 (1967).

5 C. E. T. Gonçalves and L. M. Falicov, J. Phys. C: Solid State Phys. 5 , 63 (1972).

6 T. Janssen, Phys. Kond. Mat. 15 , 142 (1972).

7 H. A. Kramers, *Physica* 1 , 182 (1934).

8 P. W. Anderson, Phys. Rev. 115 , 2 (1959).

9 B. Koiller and L. M. Falicov, J. Phys. C. 8 , 695 (1975).

10 C. Kittel, *Introduction to Solid State Physics* (Wiley, New York, 1986), 6th edition.

11 M. A. Ruderman and C. Kittel, Phys. Rev. 96 , 99 (1954).

12 See, for example, *New Developments in Semiconductors*, edited by P. R. Wallace, R. Harris and M. J. Zuckerman (Noordhoff,Leyden, 1973).

13 D. C. Mattis, *The Theory of Magnetism I* (Springer-Verlag, Berlin-Heidelberg-New York-Tokyo, 1988), and references therein.

14 R. Ritter, L. Jansen, and E. Lombardi, Phys. Rev. B 8 , 2139 (1973).

15 M. E. Fisher and W. Selke, Phil. Trans. Roy. Soc. 302 , 1 (1981).

16 *Magnetic Properties of Low-dimensional Systems* , edited by L. M. Falicov and J. L. Moran-Lopez (Springer-Verlag, Heidelberg, 1986).

17 D. Castiel, Surface Science 60 , 24 (1976).

18 V. A. Grazhulis, A. M. Ionov, and V. F. Kuleshov, Phys. Chem. Mech. Surfaces 4 , 503 (1986).

19 R. E. De Wames, Phys. Stat. Sol. 39 , 437 (1970).

20 L. M. Falicov and R. E. De Wames, Phys. Stat. Sol. 39 , 445 (1970).

21 H. C. Siegmann, Phys. Rev. 17 , 37 (1975).

22 R. H. Victora and L. M. Falicov, Phys. Rev. B. 31 , 7335 (1985).

23 L. E. Klebanoff, R. H. Victora, L. M. Falicov, and D. A. Shirley, Phys. Rev. B. 32 , 1997 (1985).

24 K. Sattler and H. C. Siegmann, Phys. Rev. Lett. 29 , 1565 (1972).

25 M. Campagna, D. T. Pierce, K. Sattler, and H. C. Siegmann, Helv. Phys. Acta. 47 , 27 (1974).

26 S. F. Alvarado, E. Kisker, and M. Campagna, in *Magnetic Properties of Low-dimensional Systems* , edited by L. M. Falicov and J. L. Moran-Lopez (Springer-Verlag, Heidelberg, 1986) p. 52.

27 D. de Fontaine, A. Finel, S. Takeda, and J. Kulik, in *Noble Metal Alloys* , edited by T. B Massalski, W. B. Pearson, L. H. Bennett, and Y. A. Chang (The Metallurgical Society, Warrendale PA, 1986), p. 49.

28 S. Aubry and P.Y. Le Daeron, *Physica* 8D , 381 (1983).

29 T. Janssen and A. Janner, Adv. Phys. 36 , 519 (1987).

30 There are eight possible antiferromagnetic {111} structures. The configuration chosen here utilizes the (111) planes and has the bulk spins pointing in the z-direction. While specific details of the calculation differ for other choices, the physical conclusions are identical for all eight structures.

31 V. G. Tissen and E. G. Ponyatovski, JETP Lett. 46 , 361 (1987).

32 P. Palmberg, R. E. De Wames, and L. Vredevoe, Phys. Rev. Lett. 21 , 682 (1968).

F. Tables for Chapter III

Table 3.1

Experimentally Determined Properties of the Europium Monochalcogenides

Compound	Structure	Critical Temperature (K)	J_{nn} (K)	J_{nnn} (K)
EuO	ferro.	69.4	-0.75	0.06
EuS	ferro.	16.5	-0.20	0.08
EuSe	ferro.	2.8	-0.13	0.11
EuSe	antiferro.	4.6	-0.13	0.11
EuTe	antiferro.	10	-0.03	0.17

Table 3.2

Surface Spins Typical of Region (II)

$(K/J) = 2.5$

$\mathbf{k} = [0\ ,\ 0]$

Surface Energy per Unit Cell = $-24.6145\ J$

$i\mu$	$x_{i\mu}$	$y_{i\mu}$	$z_{i\mu}$	$\phi_{i\mu}$
$A\alpha$	0.8660	0.8660	0.5000	0.0000
$A\beta$	0.8660	0.8660	-0.5000	0.0000
$B\alpha$	-0.8660	0.8660	0.5000	0.0000
$B\beta$	-0.8660	0.8660	-0.5000	0.0000
$C\alpha$	0.0000	0.0000	1.0000	0.0000
$C\beta$	0.0000	0.0000	-1.0000	0.0000
$D\alpha$	0.0000	0.0000	1.0000	0.0000
$D\beta$	0.0000	0.0000	-1.0000	0.0000

Table 3.3

Surface Spins Typical of Region (III)

$(K/J) = -2.50$ and $(L/J) = 2.50$

$\mathbf{k} = [0\ ,\ 0]$

Surface Energy per Unit Cell = $-45.0090\ J$

$i\mu$	$x_{i\mu}$	$y_{i\mu}$	$z_{i\mu}$	$\phi_{i\mu}$
$A\alpha$	0.9961	0.9961	0.0882	0.0409
$A\beta$	0.9961	0.9961	-0.0882	0.0409
$B\alpha$	0.9961	0.9961	0.0882	0.0409
$B\beta$	0.9961	0.9961	-0.0882	0.0409
$C\alpha$	-0.9993	-0.9993	0.0368	0.0409
$C\beta$	-0.9993	-0.9993	-0.0368	0.0409
$D\alpha$	-0.9993	-0.9993	0.0368	0.0409
$D\beta$	-0.9993	-0.9993	-0.0368	0.0409

Table 3.4

Surface Spins Typical of Region (IV)

$(K/J) = 3.00$ and $(L/J) = 4.00$

$\mathbf{k} = [0\ ,\ 0]$

Surface Energy per Unit Cell $= -30.5833\ J$

$i\mu$	$x_{i\mu}$	$y_{i\mu}$	$z_{i\mu}$	$\phi_{i\mu}$
$A\alpha$	0.9683	0.9683	0.2499	0.8872
$A\beta$	0.9683	0.9683	-0.2499	0.8872
$B\alpha$	0.9683	-0.9683	0.2499	0.8700
$B\beta$	0.9683	-0.9683	-0.2499	0.8700
$C\alpha$	0.9270	-0.9270	0.3751	0.0085
$C\beta$	0.9270	-0.9270	-0.3751	0.0085
$D\alpha$	0.9270	-0.9270	0.3751	0.0085
$D\beta$	0.9270	-0.9270	-0.3751	0.0085

Table 3.5

Surface Spins Typical of Region (iv)

$(K/J) = 2.25$ and $(L/J) = 2.25$

k = [0.0000 , 0.2445]

Surface Energy per Unit Cell = $-25.0471\ J$

$i\mu$	$x_{i\mu}$	$y_{i\mu}$	$z_{i\mu}$	$\phi_{i\mu}$
$A\alpha$	-0.7321	-0.7321	0.6812	0.0000
$A\beta$	-0.7321	-0.7321	-0.6812	-2.3734
$B\alpha$	-0.7321	-0.7321	0.6812	0.0000
$B\beta$	-0.7321	-0.7321	-0.6812	-2.3734
$C\alpha$	0.8369	0.8369	0.5474	-5.0965
$C\beta$	0.8369	0.8369	-0.5474	-1.1867
$D\alpha$	0.8369	0.8369	0.5474	-5.0965
$D\beta$	0.8369	0.8369	-0.5474	-1.1867

Table 3.6

Surface Spins of Region (iv)				
$(K/J) = 2.25$ and $(L/J) = 2.25$				
$\mathbf{k} = [0.2445 , 0.0000]$				
Surface Energy per Unit Cell = $-25.0471\ J$				
$i\mu$	$x_{i\mu}$	$y_{i\mu}$	$z_{i\mu}$	$\phi_{i\mu}$
$A\alpha$	-0.7321	-0.7321	0.6812	0.0000
$A\beta$	-0.7321	-0.7321	-0.6812	-2.3734
$B\alpha$	-0.7321	-0.7321	0.6812	-2.3734
$B\beta$	-0.7321	-0.7321	-0.6812	0.0000
$C\alpha$	0.8369	0.8369	0.5474	-1.1867
$C\beta$	0.8369	0.8369	-0.5474	-3.5600
$D\alpha$	0.8369	0.8369	0.5474	-3.5600
$D\beta$	0.8369	0.8369	-0.5474	-1.1867

Table 3.7

Surface Spins Typical of Region (v)

$(K/J) = 3.00$ and $(L/J) = 3.00$

k = [0.0000 , –0.3078]

Surface Energy per Unit Cell = –29.3888 J

$i\mu$	$x_{i\mu}$	$y_{i\mu}$	$z_{i\mu}$	$\phi_{i\mu}$
$A\alpha$	0.3654	0.3654	0.9308	0.0000
$A\beta$	0.8842	0.8842	0.5360	-4.1085
$B\alpha$	0.8442	0.8442	-0.5360	0.0000
$B\beta$	0.3654	0.3654	-0.9308	-4.1085
$C\alpha$	0.8800	0.8800	0.4750	2.0542
$C\beta$	0.8800	0.8800	-0.4750	-2.0542
$D\alpha$	0.8800	0.8800	0.4750	2.0542
$D\beta$	0.8800	0.8800	-0.4750	-2.0542

G. Figures for Chapter III

Figure 3.1 A schematic description of the superexchange interaction. The central dark circle in each picture is the p-orbital of the anion; the light circles represent the f-orbitals of the cations. The "propeller-like" structures represent the spatial extent of the anion p-orbital. Figure 3.1(a) is the initial configuration of spins. Figure 3.1(b) is the intermediate state. In this state, one of the anion electrons hops to the left cation, and the remaining anion electron undergoes a direct exchange with the electron on the the right cation. The dashed arrows indicate this exchange. Figure 3.1(c) is the final configuration. One electron from the doubly occupied cation ion has returned to the central anion.. Note that the net result of this process is the exchange of the electrons on the cations. The interaction is inherently antiferromagnetic and cannot proceed if the spins on the cations are aligned. Furthermore, the axial nature of the p-orbitals ensures that this interaction only operates when the three orbitals are spatially collinear. This process enters in second order perturbation theory and always reduces the energy.

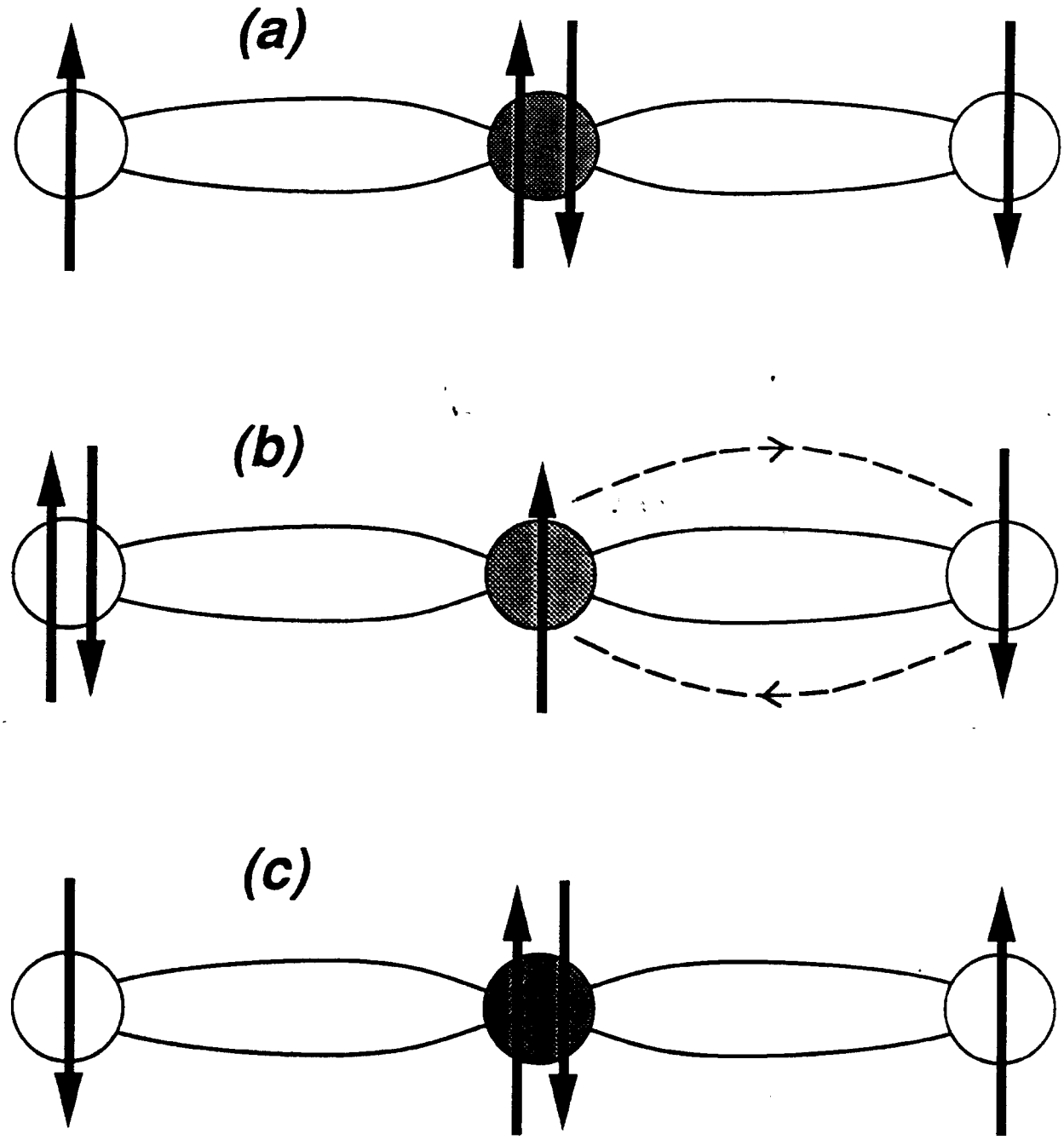

Figure 3.1

Figure 3.2 The observed stable magnetic structure of EuTe. The cation spins, which lie on an *fcc* lattice are pictured. The central "dumb-bell" structure represents one p-orbital of the central anion. The axial nature of these orbitals ensures that the superexchange mechanism is only operative between second-neighbor Eu atoms. The stable magnetic structure has each Eu spin aligned antiferromagnetically with its six second-neighbors. In this configuration, the spins in each (111) plane are aligned ferromagnetically, and then each (111) plane is aligned antiferromagnetically with its nearest-neighbor (111) planes.

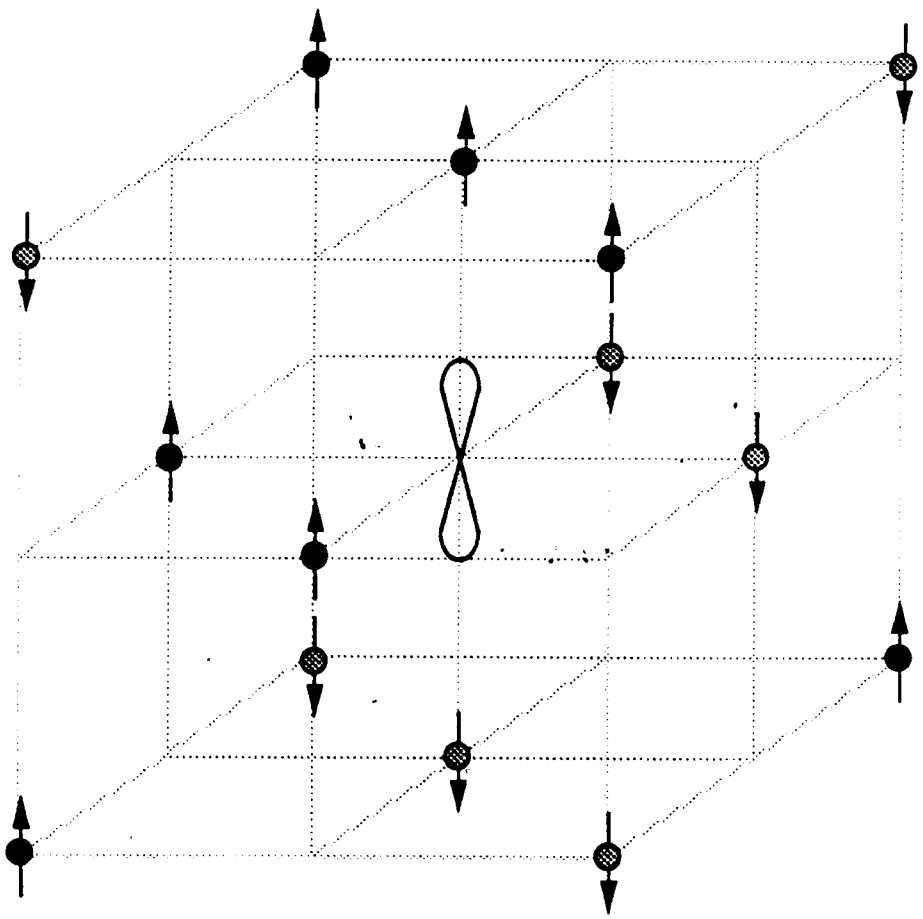

Figure 3.2

Figure 3.3 The Eu atoms of the (001) surface of EuTe. The spins of the europium atoms are indicated in stereographic projections, with dots pointing upwards and crosses pointing downwards. The spins are depicted in the chosen bulk configuration. The line labelled J represents the second-nearest-neighbor superexchange interaction, and the line labelled K represents the nearest-neighbor interaction, effective among surface atoms only. The nearest-neighbor interaction between a surface europium atom and its four nearest neighbors in the plane below (not shown) is represented by L.

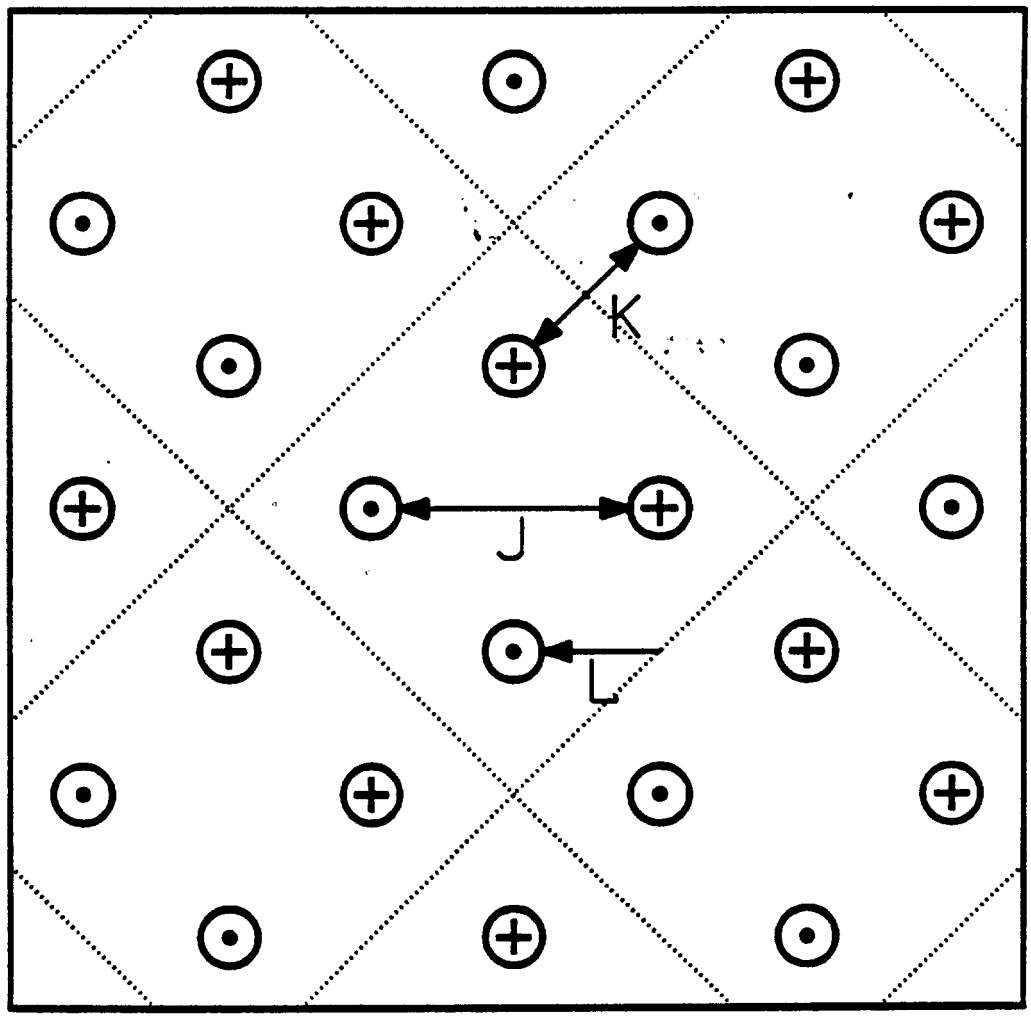

Figure 3.3

Figure 3.4 The unit cell and the Brillouin zone used for the calculation with all spins (indicated in stereographic projections as in figure 3.3) in the chosen bulk configuration. The unit cell has linear dimension b as shown. The first label on each atom refers to the simple cubic sublattice and the Greek label refers to the face-centered-cubic subsublattice to which that atom belongs. The shaded atoms lie in the plane immediately below the surface, the remaining pictured spins are in the surface plane. The Γ-point corresponds t possible commensurable structures. The points Y and Y′ are not equivalent because of the asymmetry of the bulk spin domain structure.

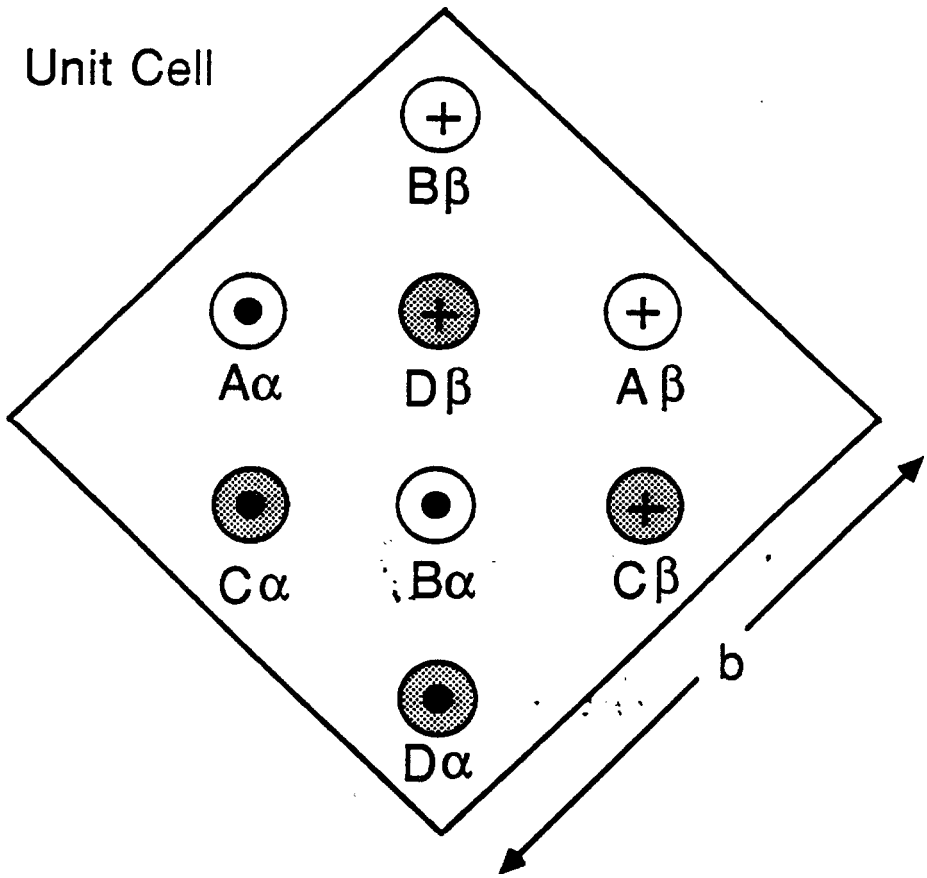

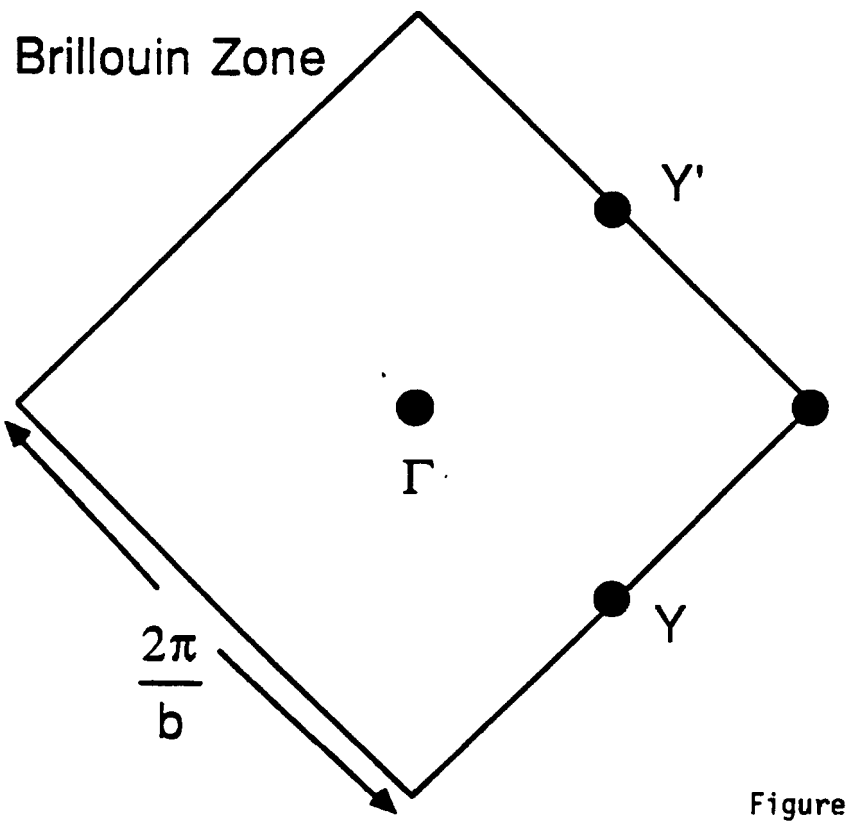

Figure 3.4

Figure 3.5 The phase-stability diagram for commensurable structures. Region (I) is the unreconstructed, bulk-like surface. In regions (II) the various spins acquire an xy-component and tilt away form their original $\pm z$ orientation. In the limit $(K/J) \rightarrow \infty$ the surface is a perfect nearest-neighbor square-antiferromagnet (NNSA), with surface spins aligned in the xy-plane and each surface spin aligned antiparallel to its four nearest neighbors in the surface layer. Region (III) is similar, but with the surface spins tilting toward a ferromagnetic surface configuration. Regions (IV_a) and (IV_b) correspond to a more complicated spiral-type arrangement of the spins., The contours are the energies per unit cell of the two surface layers of the commensurable states in units of J.

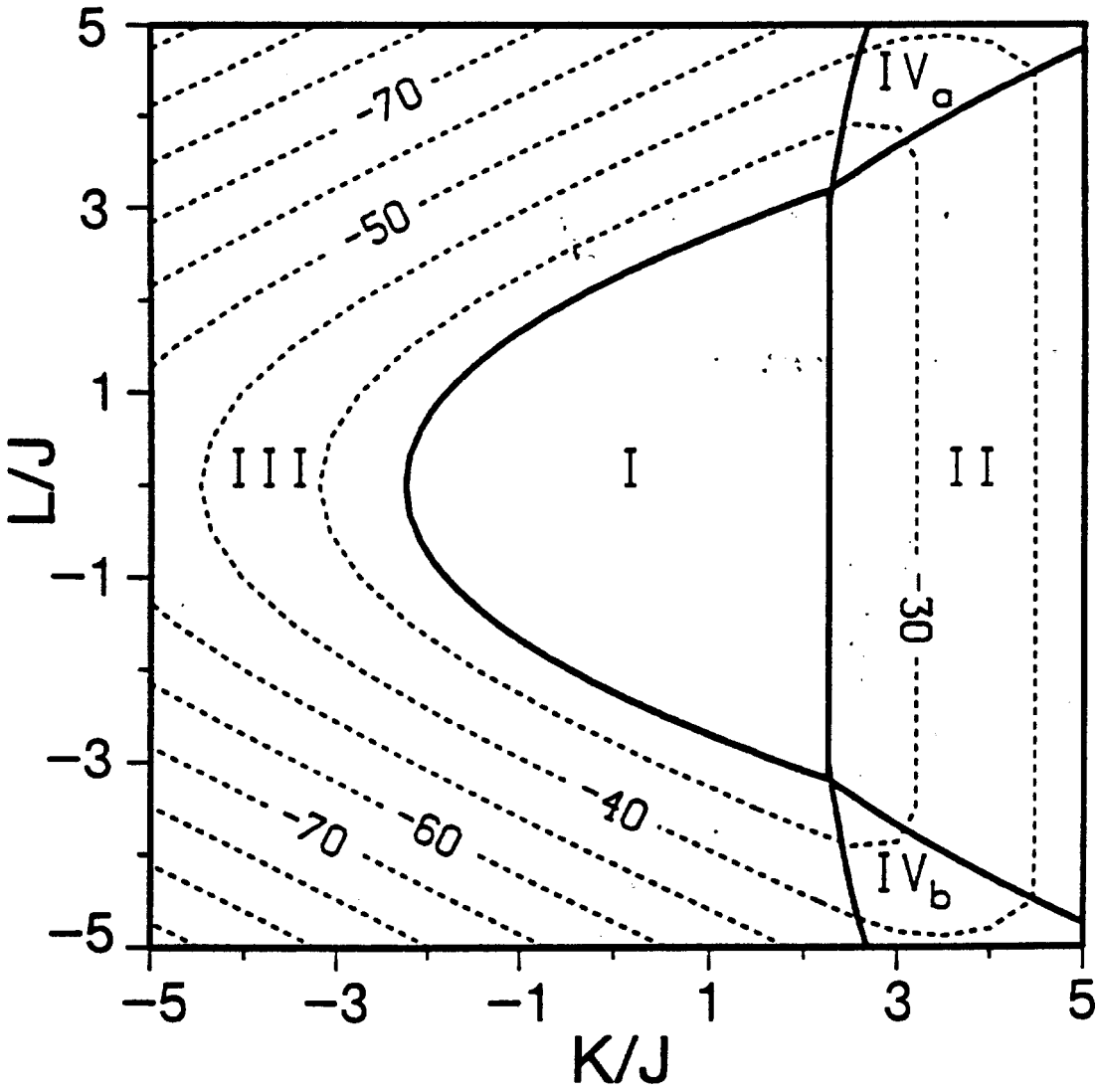

Figure 3.5

Figure 3.6 A stereographic projection of the surface spins for a structure typical of region (II) corresponding to the spin parameters in table 3.2. The dots denote spins pointing up and the crosses spins pointing down. The NNSA character of this state is clearly evident.

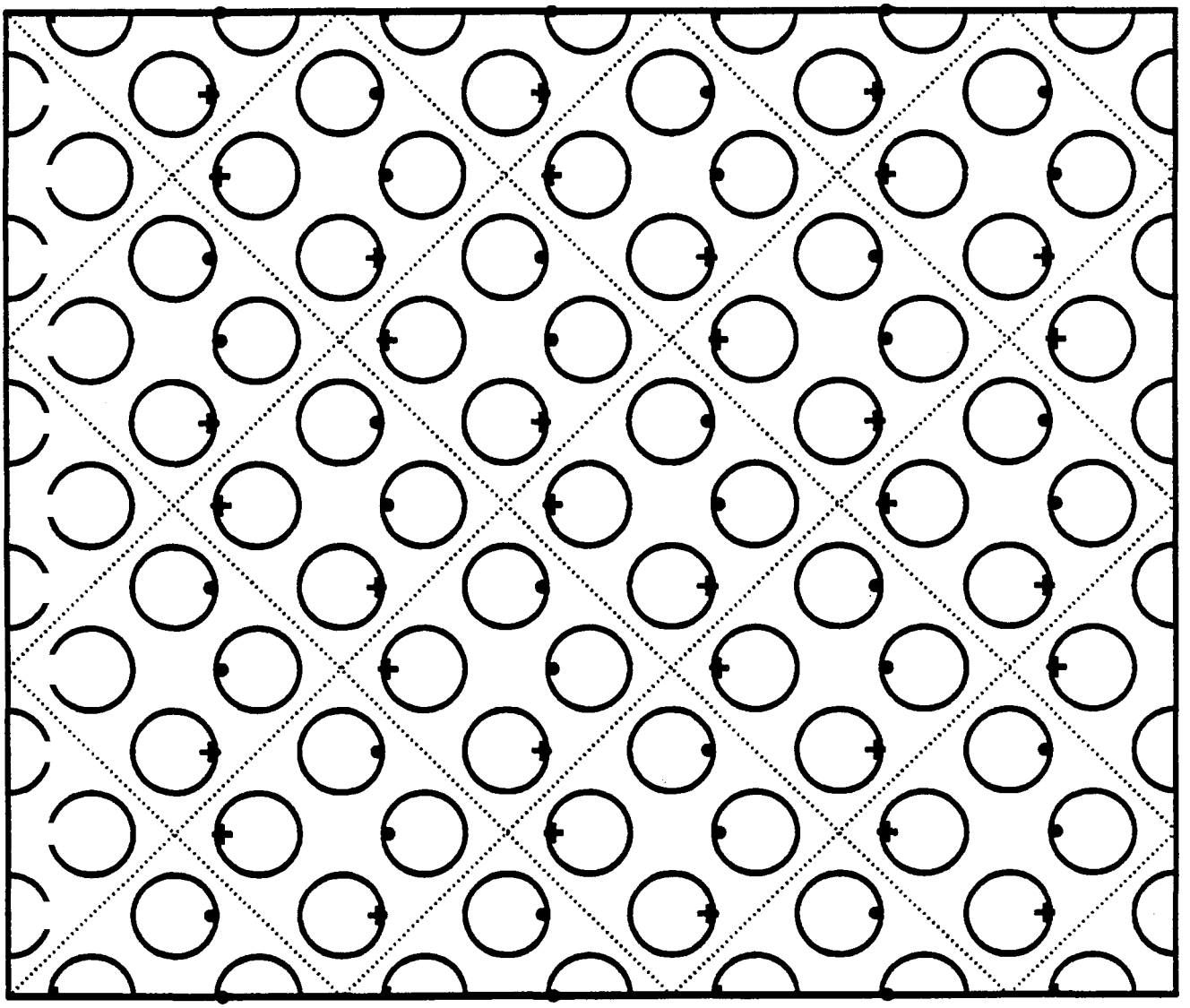

Figure 3.6

Figure 3.7 The phase-stability diagram for all examined structures. Regions (i), (ii), and (iii) are commensurable structures identical to the corresponding structures of figure 3.5. The shaded regions are incommensurable structures. The incommensurable structures all, as found, have a single **k**-vector. The regions (iv) have an extra degeneracy not present in regions (v).

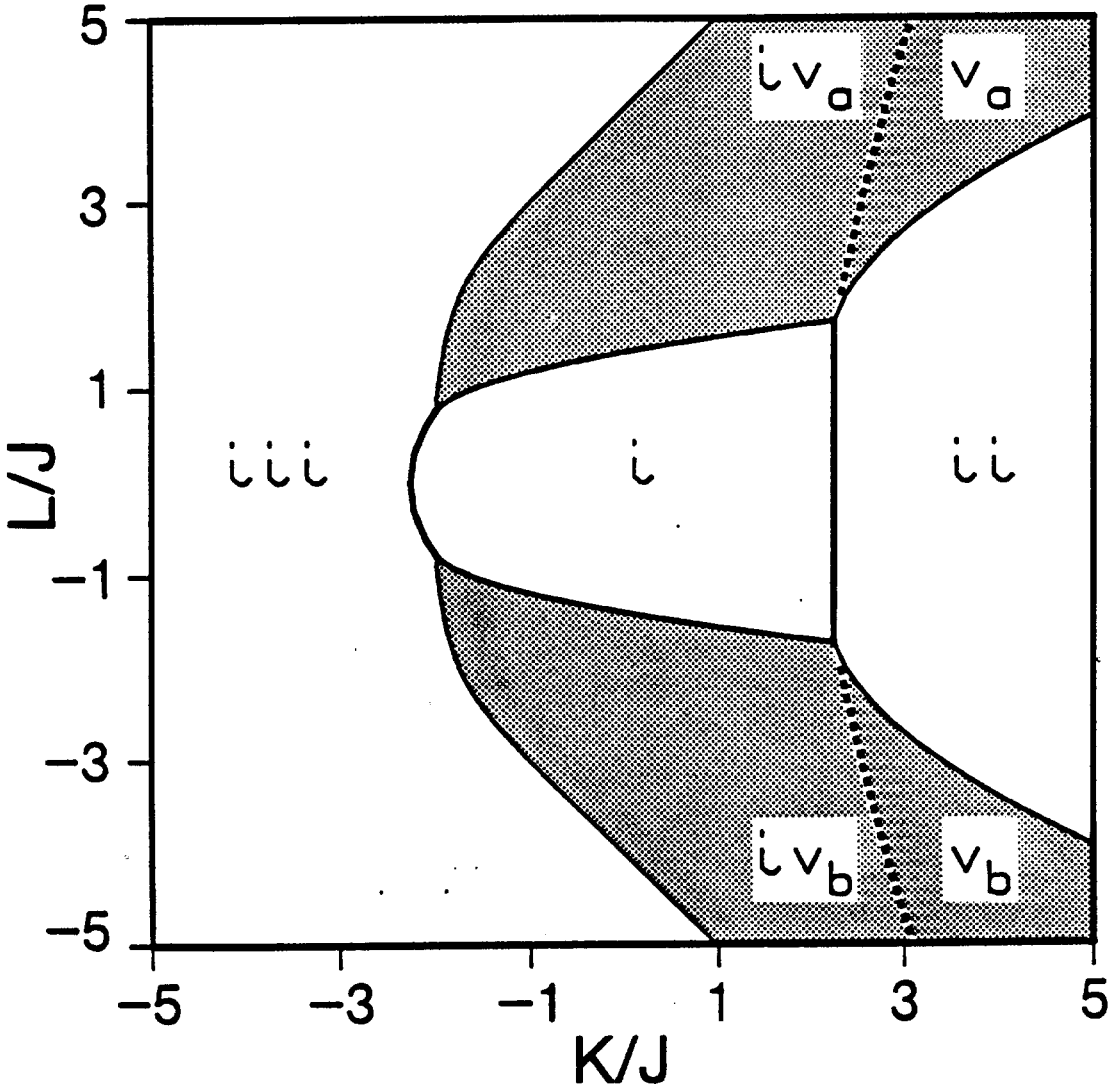

Figure 3.7

Figure 3.8 A stereographic projection of the surface spins for a structure typical of regions (iv) corresponding to the spin parameters in table 3.5. The dots denote spins pointing up and the crosses spins pointing down. The arrow indicates the direction of **k** for this state. This surface state has a character similar to the bulk configuration, and is degenerate with the state pictured in figure 3.9.

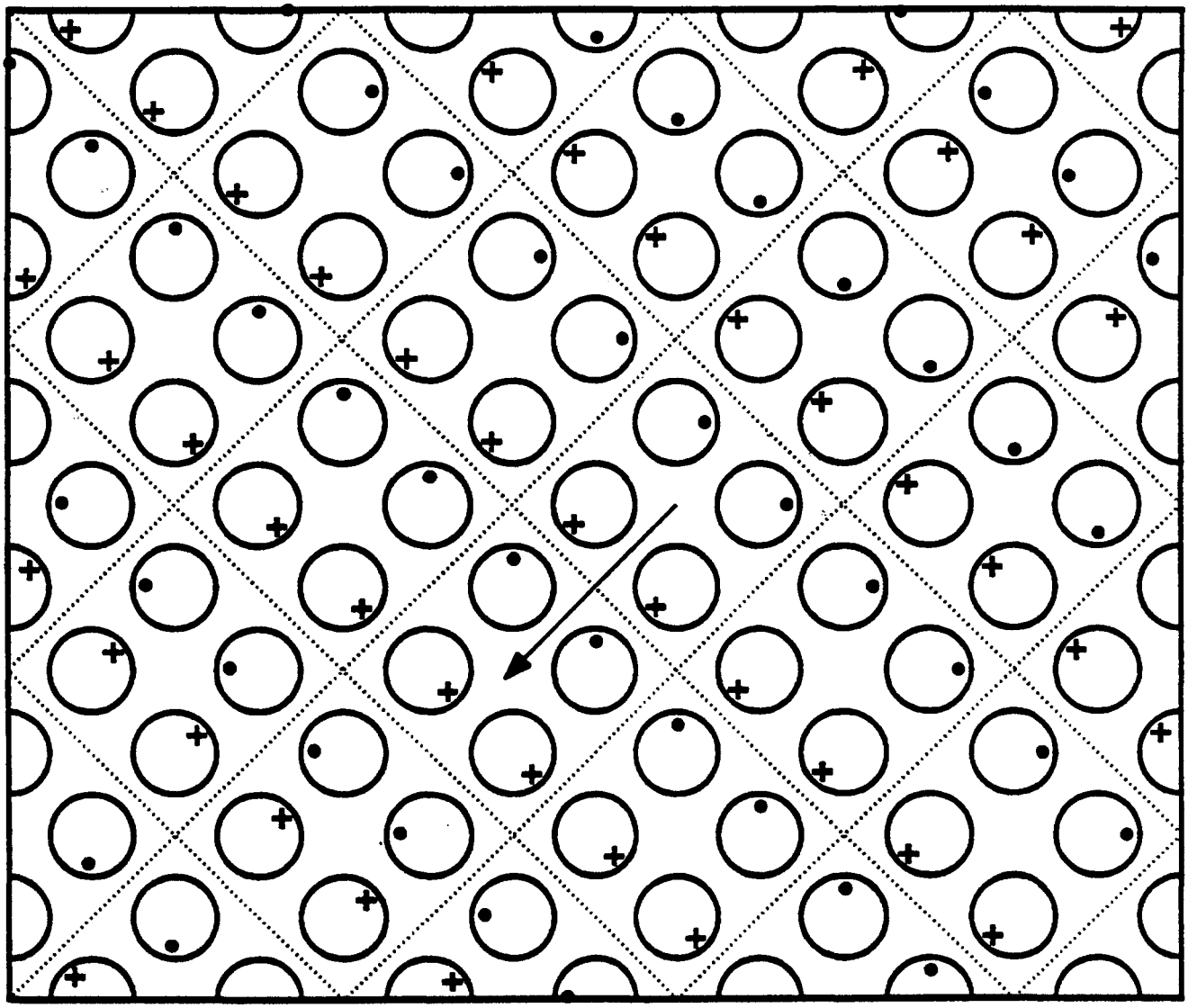

Figure 3.8

Figure 3.9 A stereographic projection of the surface spins for a structure typical of regions (iv) corresponding to the spin parameters in table 3.6. The dots denote spins pointing up and the crosses spins pointing down. The arrow indicates the direction of **k** for this state. This surface state has a character similar to the bulk configuration, and is degenerate with the state pictured in figure 3.8.

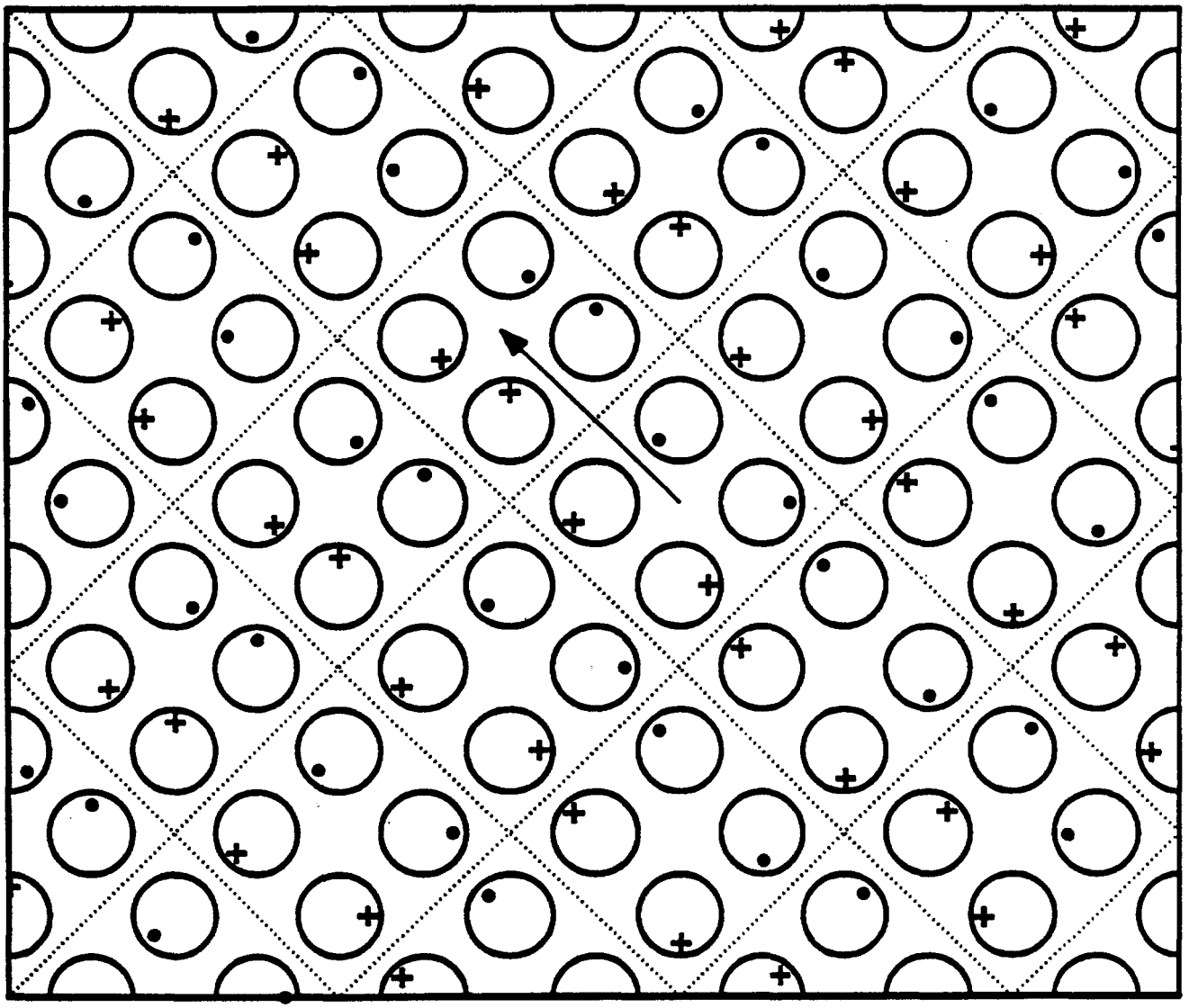

Figure 3.9

Figure 3.10 A stereographic projection of the surface spins for a structure typical of regions (v) corresponding to the spin parameters in table 3.7. The dots denote spins pointing up and the crosses spins pointing down. The arrow indicates the direction of **k** for this state. The nearest-neighbor square-antiferromagnetic (NNSA) character of this state is quite evident.

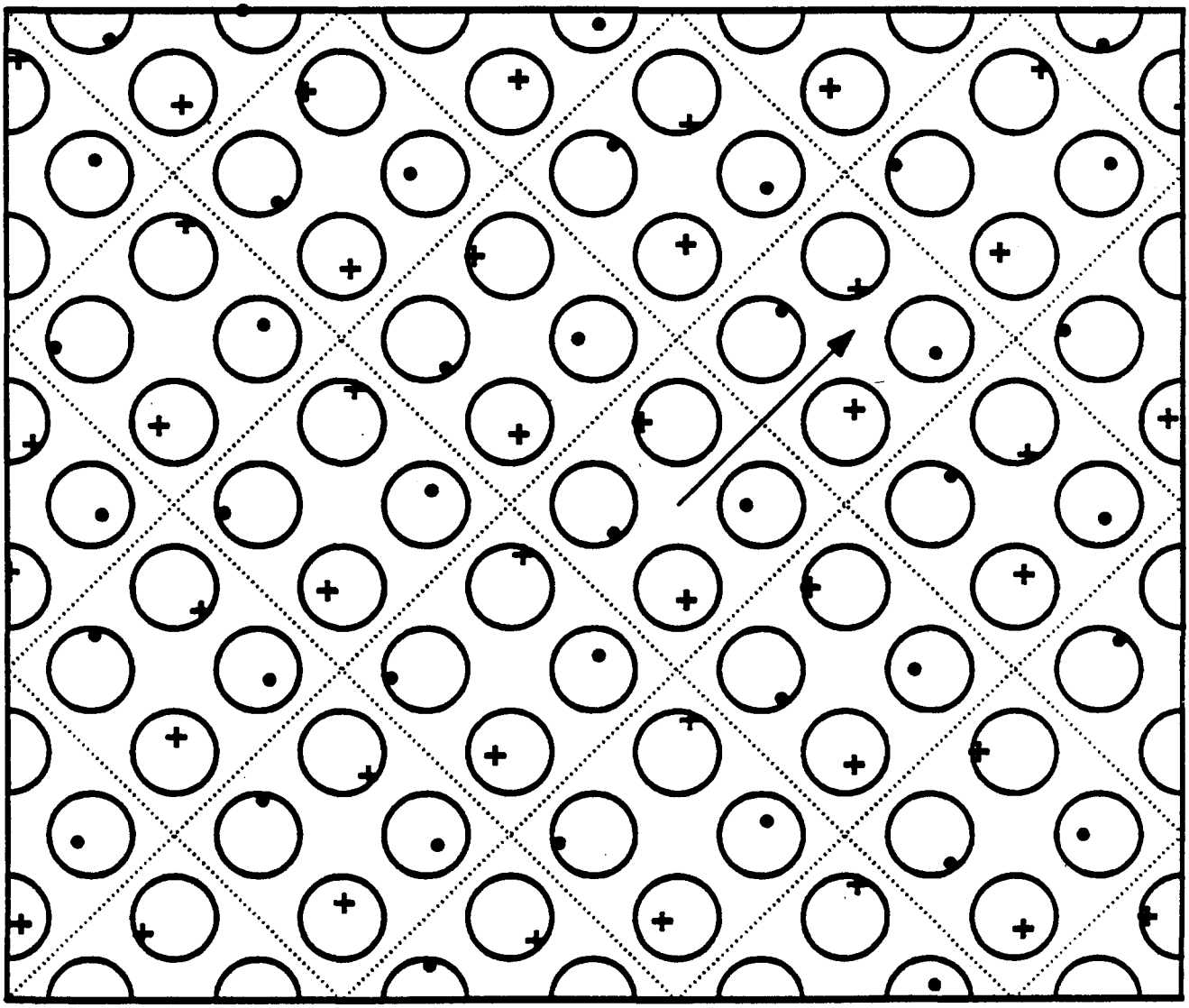

Figure 3.10

Figure 3.11 (a) The structure factor for the various diffraction beams as a function of (L/J) for $(K/J) = 0$. The solid line is the structure factor for one of the bulk-like antiferromagnetic spots, the chain-dot line is for the surface ferromagnetic structure, and the dotted line is the structure factor for the incommensurable spot. At $(L/J) = 4.00$, two incommensurable spots merge at the zone center. (b) A schematic drawing of the LEED pattern expected from surface for the structures corresponding to the structure factors of figure 3.11(a). The structure responsible for each of the peaks is indicated in the box. The arrows indicate that those LEED spots move as the exchange interactions are varied. Eventually, the incommensurable spots merge at the zone center as is described in the text.

(a)

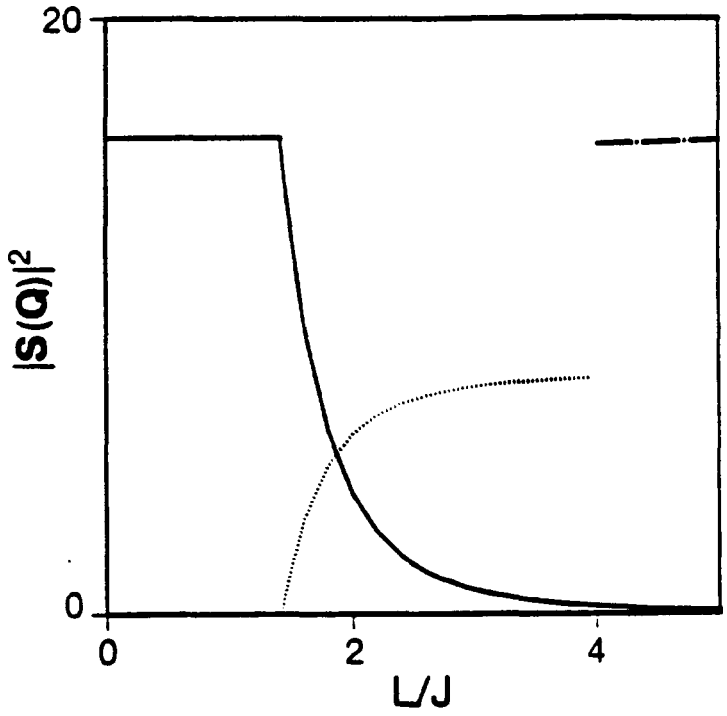

(b)

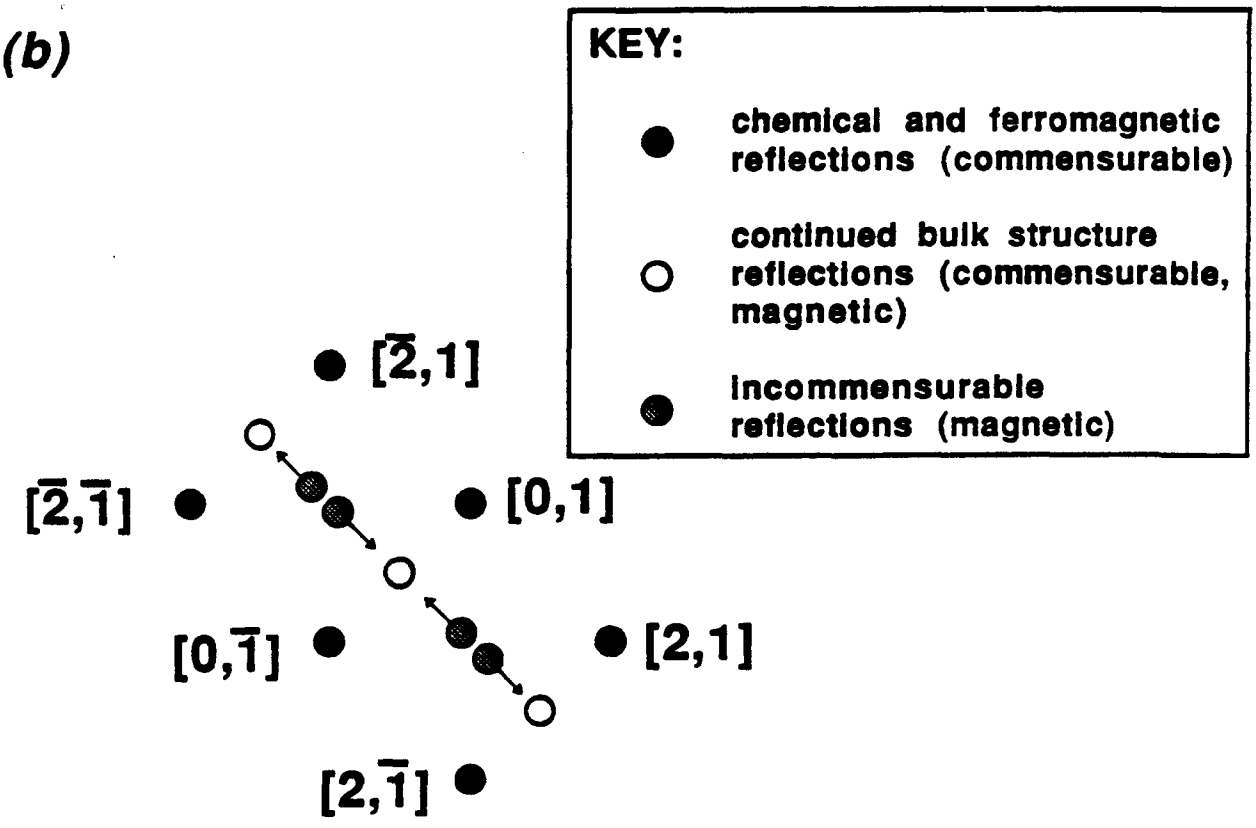

Figure 3.11

Figure 3.12 The **k**-vectors of the stable magnetic structures used to construct the plot in figure 3.11(a). The vectors originate at Γ and end at the indicated point along the Γ-to-Y line.

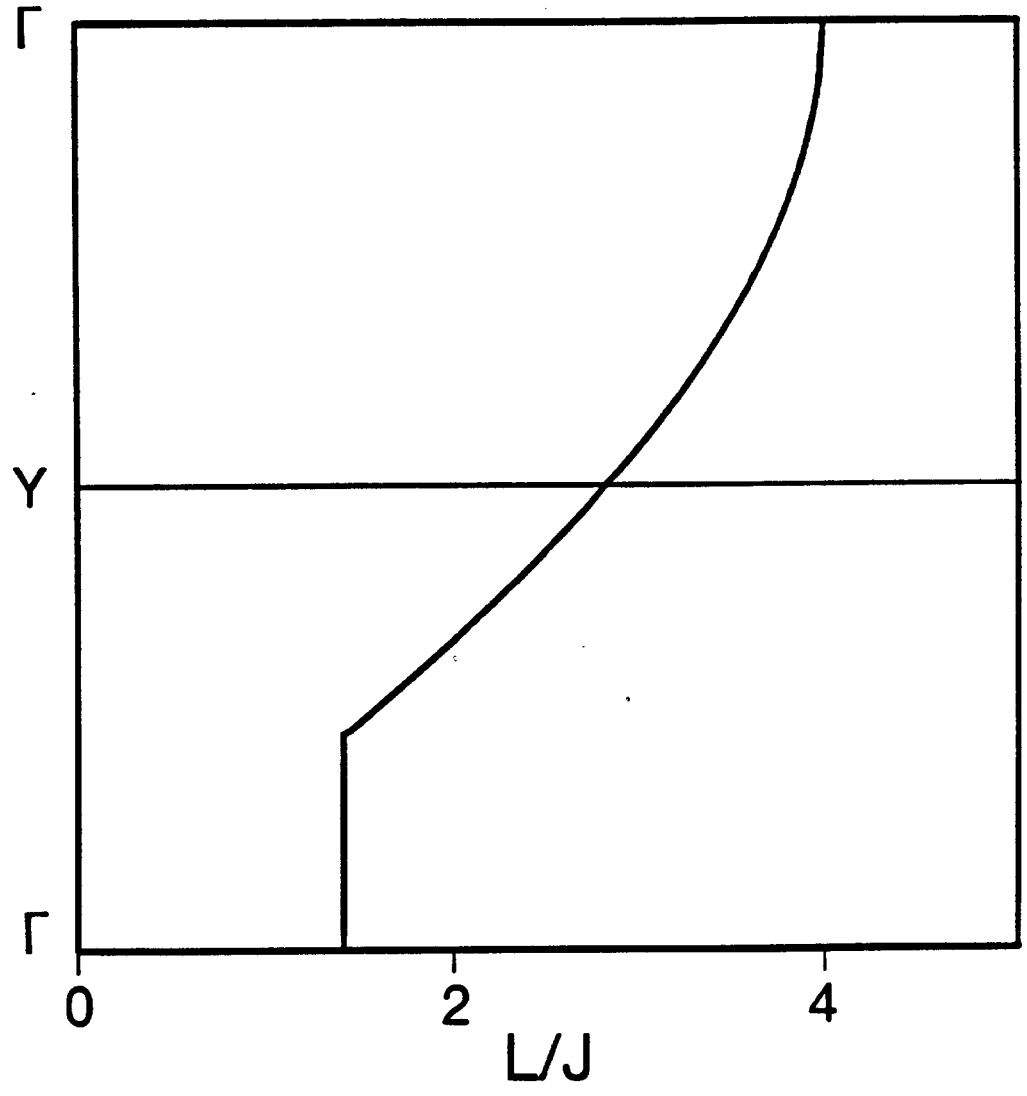

Figure 3.12

Figure 3.13 The magnetic structure factor for $(L/J) = 3.00$ as a function of (K/J) for the minimum energy state chosen to have **k** along the Γ-to-Y′ direction. The solid line is the structure factor for the bulk-like diffraction beams at $\mathbf{Q} = [2n\ ,\ 2m + 1]$, the dashed line is the structure factor for the nearest-neighbor square-antiferromagnet-like (NNSA-like) beams at $\mathbf{Q} = [2n + 1\ ,\ 2m + 1]$, the dotted line is the structure factor for incommensurable spots at $\mathbf{Q} = [2n\ ,\ 2m + 1] \pm \mathbf{k}$, and the chain-dash line is the structure factor for incommensurable spots at $\mathbf{Q} = [2n + 1\ ,\ 2m + 1] \pm \mathbf{k}$. The structural transition upon crossing the (iv_a)-(v_a) boundary at $(K/J) = 2.56$ is clearly evident.

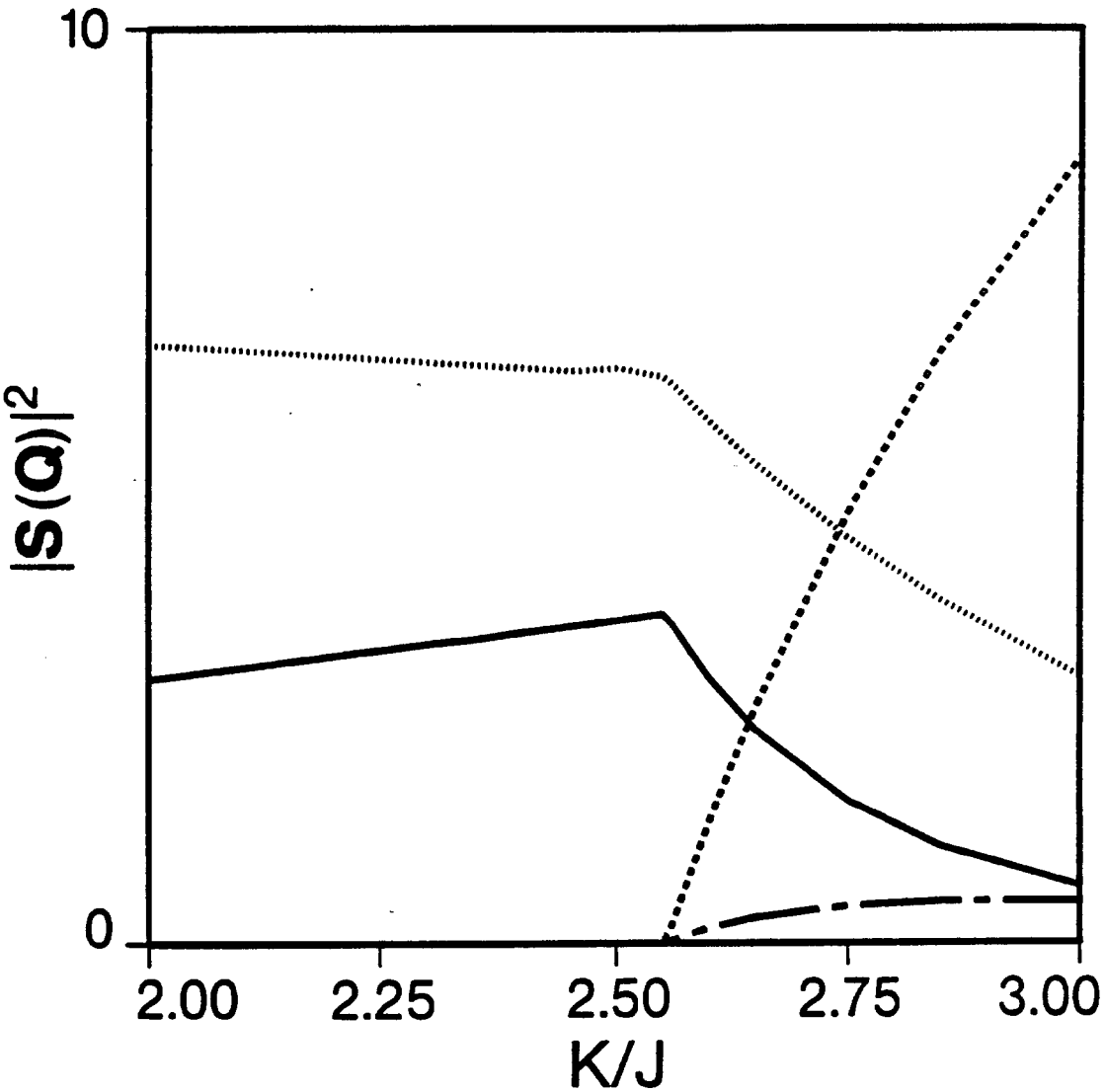

Figure 3.13

Chapter IV: Magnetic Properties of {111} Stacking Faults in Nickel

A. Introduction

The study of systems with complete translational invariance is dramatically simplified by judicious application of Bloch's theorem. Electronic structure calculations based on this theorem lead directly to accurate predictions of physical properties as diverse as the superconducting transition temperature or the expected spectrum of the electrons one should observe in a photoemission experiment.

"Real-world" systems, however, do not possess the full translational periodicity required for the direct application of Bloch's theorem. Even in a perfect crystal at zero temperature, there is no perfect periodicity; it is destroyed by zero-point motion. Nevertheless, Bloch's theorem holds in an approximate sense; on the average the crystal is periodic. The utility of Bloch's theorem originates in this observation.

There are systems, however, which are not even approximately periodic (e.g. liquids, glasses, and amorphous materials). The calculational techniques used for these materials cannot rely on translational invariance. Progress in this direction has been made. In particular, the newly developed real-space methods[1,2] for calculating electronic structure of solids and liquids are very promising.

This chapter is concerned with the electronic and magnetic structure of {111} stacking faults in nickel. For a {111} stacking fault, the periodicity within the (111) planes is unaltered, whereas the stacking fault eliminates translational invariance in the direction normal to the planes. Recent advances in electronic structure calculations permit the calculation of the physical properties of these defects, within the one-electron approximation, without imposing three-dimensional periodicity or the use of finite-sized slabs.

Considerable attention has been focused on the theoretical properties of transition-metal surfaces and interfaces.[3–10] Much of the excitement stems from the

prediction and observation of enhanced magnetic moments at surfaces[4,7–9], as well as the possibility of surface ferromagnetism or antiferromagnetism.[3,8]

The availability and application of surface-sensitive spectroscopy techniques, coupled with new techniques for producing high quality superlattices and interfaces,[11] provides the strongest stimulus to this theoretical interest. Spin-polarized photoemission,[12–14] inverse[15] and angle-resolved[16] photoemission, both spin-polarized[17] and unpolarized[18] low-energy-electron-diffraction, and spin-polarized electron energy-loss spectroscopy[19] have provided very interesting results which are not yet completely understood. In addition, these experimental methods are also used to study the thermodynamic properties of two-dimensional magnetic systems[20,21], which are of fundamental interest, through the experimental investigation of thin transition-metal films on nonmagnetic substrates.

The complete understanding of all these systems, however, requires a thorough understanding of the transition metals themselves, and the factors that influence their magnetic properties. For example, it is clear that in order fully to understand a "two-dimensional" transition-metal film, one must have some understanding of how the electronic states of the transition metal interact with states of the nonmagnetic substrate, which in turn, requires detailed knowledge of the transition-metal states. Additionally, the properties of structural defects in the pure materials must be fully understood so that one may distinguish between the effects of alloying and those of structural differences.

It is well known that near-neighbor coordination number affects the observed magnetic moments of transition metals. In general, a decrease in coordination number results in an increase in magnetic moment. This can be loosely understood in terms of the Stoner model in which a decrease in the ratio of bandwidth to electron-electron interaction results in an increase in magnetic moment. A decrease in coordination number results in a narrowing of the local density of states, thus enhancing the spin

polarization. The effect is most pronounced in magnetic systems such as chromium or iron which are not saturated (i.e. do not have a filled majority d-bands). Nickel is a saturated system, but its calculated total spin polarization is small [0.60 μ_B (calculated below)], which implies that any slight change in spin polarization represents a relatively large percentage change. Tight-binding calculations[7,8,22–24] predict a spin polarization enhancement of sixteen percent for the {111} surfaces of nickel, an enhancement from 2.12 μ_B to 2.90 μ_B at the {001} sufaces of iron, and an enhancement of the chromium spin polarization from 0.59 μ_B in the antiferromagnetic bulk to 2.5 μ_B on the ferromagnetic (001) surface. These studies, however, do not directly address the magnetic properties of stacking faults in the pure transition-metal alloys. For instance, in the {111} stacking faults of the *fcc* structure, the nearest- and next-nearest-neighbor coordination number of the atoms in the fault remain twelve and six, respectively, but the cubic symmetry of the environment is lost and the further-neighbor coordination numbers are altered.

There has been much less attention given to planar structural defects (other than surfaces) in pure transition metals. Yndurain and Falicov studied the properties of {111} stacking faults in nickel using an unpolarized tight-binding method[25] and found that localized electronic states appear at the interfaces, but did not consider their magnetic structure. Grise *et al.*[26] performed tight-binding calculations utilizing large unit-cells containing stacking faults and found localized states and a three percent change in spin polarization on the central layer of an extrinsic fault. This calculation was not performed self-consistently, nor was any attempt made to understand the source of the changes in electronic and magnetic structure near the faults.

Given the existence of localized states, and the apparent sensitivity of the magnetic configuration to coordination number and loss of three-dimensional symmetry, one might expect the magnetic properties of stacking faults to display interesting, possibly technologically important, behavior. The aim of the present study is the charac-

terization of {111} stacking faults in ferromagnetic nickel. The electronic and magnetic properties are calculated using a fully self-consistent, layered Korringa-Kohn-Rostoker (LKKR)[27] technique based on a local spin-density approximation to density-functional theory. LKKR does *not* require three-dimensional symmetry or the use of finite-sized slabs.

The spin polarizations and total energies for face-centered-cubic *(fcc)* nickel, hexagonal-close-packed *(hcp)* nickel, double-hexagonal-close-packed *(dhcp)* nickel, and several types of stacking defects are calculated and analyzed. The results are used to derive a very simple empirical expression for both the polarization and internal energy of any stacking configuration. It is argued that the small changes in spin polarization are the result of two subtle effects: 1) a symmetry induced rearrangement of the majority-spin states near the Fermi level and, 2) a local broadening and change in structure of the states derived from the minority-spin band which crosses the Fermi level near L along the Γ to L direction of the *fcc* Brillouin zone.

Part B of this chapter contains a brief description of the method of calculation. Section C presents the results of the calculations. Part D contains the analysis of the results, and simple empirical relations for the spin polarization and internal energy of any stacking sequence are derived and analyzed in section E. The conclusions are presented in section F.

B. Method of Calculation

In LKKR, the properties of a three-dimensional periodic solid are calculated by building it from two-dimensional periodic planes. The method proceeds by first calculating the T-matrix of an entire plane. This, in turn, is used to calculate the T-matrix of a two-plane unit. The T-matrix of the two-plane system is then used to generate the T-matrix of a four-plane unit. This process, referred to as layer-doubling[27], is repeated until the T-matrix of the bulk is generated. Layer-doubling provides an extremely efficient method for building the complete three-dimensional solid; seventy-five

doublings results in the T-matrix for a slab of nickel extending from the earth to the sun!

Once the T-matrix of the entire solid is known, the single particle Green's function is calculated from the Dyson equation

$$G = G_o + G_o\, T\, G_o \quad ,$$

where G_o is the free particle Green's function and T is the T-matrix for the complete solid. The Green's function can then be used to calculate the physical properties of the solid. For example, the spatial and energy-resolved density-of-states (DOS), $\rho(\mathbf{r},E)$, is given by

$$\rho(\mathbf{r},E) = -1/\pi\ \mathrm{Im}\ G(\mathbf{r},\mathbf{r},E) \quad ,$$

where $\mathbf{r}$ denotes the position and E denotes the energy. The spatial and energy-resolved DOS can then be used to calculate the charge density, Fermi energy, and electronic energy of the system, merely by integrating over the appropriate variable with the appropriate weighting factor.

In the self-consistent iterations, the charge density calculated from the Green's function is used to generate a new potential which includes contributions from both the Coulomb interaction with the other electrons (found from the solution of Poisson's equation using Weinert's method[28]) and the exchange-correlation potential in the local spin-density approximation (by means of the expression of Gunnarsson and Lundqvist[29] which is a spin-polarized version of that derived by Hedin and Lundqvist[30]). The generated potential is then converted to a muffin-tin form, which is known to produce good results for close-packed transition metals. The phase shifts of these potentials are calculated, including the semi-relativistic corrections of Koelling and Harmon,[31] and a new T-matrix is calculated. The entire process is then iterated to self-consistency.

The LKKR formalism easily adapts to a three-dimensional system containing a stacking defect. In calculating the properties of a stacking defect, the first step completely characterizes the bulk material. The second step is to embed N layers of material, containing the entire structure of the stacking fault, within the bulk system (figure 4.1). The self-consistent formalism described above is then applied to the N-layer region; the potentials of the atoms in the N layers are allowed to change but the potentials in the bulk regions are fixed to have their bulk values, as is the Fermi level of the complete (stacking fault and bulk) system. The constraint that the potentials be bulk-like outside of the N-layer region provides the boundary condition for the adjusted region. The positions of the atoms within the layers are not allowed to relax.

This procedure allows an exact calculation of the single-particle electronic properties of the a stacking fault within the local-spin-density and muffin-tin approximations as the number of layers containing the fault can be made arbitrarily large. In practice, it is found that only a few layers, usually less than required in the finite-sized slab calculation of the same system, are necessary to obtain convergence. This method does not suffer from the problems inherent in "supercell" or finite-sized slab calculations. The details of the calculational procedure can be found in the paper by MacLaren *et al.*[32].

The calculations presented below do not include the effects of spin-orbit coupling[33], and thus do not make any predictions concerning the anisotropy energy at a stacking fault. It is possible (although not likely) that the spin-orbit interaction could modify the results presented here, although it is difficult to assess spin-orbit coupling's importance without an explicit calculation. However, it is the intention of this work to investigate the effects of the changes in crystal field near a fault. Spin-orbit effects, which are usually smaller than the crystal-field effects, are probably only important in regions of reciprocal space where bands cross near the Fermi level. The crystal field effects on the band-structure are quite large, and it is hoped that the calculations

presented below provide a good idea of how the magnitude of the spin polarization varies throughout the stacking fault even though spin-orbit effects are not included in the self-consistency requirement. It is also certain that if spin-orbit effects were important, they would not completely cancel the effects of the changes in crystal field.

A mixed basis is used in LKKR. The multiple scattering equations in each plane are solved in a spherical-wave basis. The spherical-wave basis is then transformed into a plane-wave basis which is used to connect the separate planes. Many of the calculations are performed off the real axis in the upper-half complex plane; physical properties are then obtained using the analytic properties of G. For these calculations, only a small number of basis functions is needed. The spherical basis includes the $l = 0$ to $l = 2$ waves, and the connecting basis consists of thirteen plane-waves. The integrations in reciprocal space are carried out using six points in the irreducible two-dimensional Brillioun zone. The chosen lattice constant, 6.55 au, is the value used by Moruzzi, Janak and Williams.[34] For the bulk calculations (the *fcc*, *hcp* and *dhcp* structures), the potentials were iterated until the Fermi energy was stable to 10 microHartrees (μHa). The potentials of the interface calculations were iterated to obtain a similar accuracy. At this level of self-consistency, the spin polarizations are stable to at least ± 0.002 μ_B.

C. Results

The muffin-tin density-of-states (MTDOS), i.e. the DOS resulting from integrating $\rho(\mathbf{r},E)$ over the muffin-tin, for *fcc* nickel is displayed in figure 4.2. The calculated Fermi energy is 0.35198 Ha above muffin-tin zero (all remaining energies are quoted relative to muffin-tin zero) and the muffin-tin spin polarization, which is the polarization of the charge within the muffin-tin radius, is 0.614 μ_B, where μ_B is the Bohr magneton. The spin polarization of the Wigner-Seitz sphere is 0.597 μ_B, indicating that the charge in the interstitial region is polarized antiferromagnetically relative to the charge in the muffin-tin, a feature common to all the calculations below. A self-

consistent calculation utilizing twenty-five plane waves and eighteen **k**-points in the irreducible two-dimensional zone yielded a muffin-tin moment of 0.61 μ_B and a Fermi energy of 0.3525 Ha. Since the purpose of this study is to analyze trends, these minor differences were deemed unimportant, and the remaining calculations were carried out using the smaller basis set. While the calculations have not completely converged (with regards to the number of **k**-points) the quoted trends are most likely present in the completely converged calculations, although the magnitudes may change slightly. The exchange splitting, as measured by the peak in the MTDOS nearest the Fermi level, is 0.025 ± 0.001 Ha (0.68 eV), which agrees well with the value obtained by and Wang and Callaway,[35] 0.63 eV.

Figure 4.3 is the MTDOS of (hypothetical) bulk *hcp* nickel. (The nearest-neighbor distance is kept equal to that for the *fcc* calculation, and *c/a* is chosen to be ideal.) While this structure is not thermodynamically stable (in fact, hypothetical *hcp* nickel is ***unstable*** to local perturbations and would spontaneously form *fcc*-like stacking defects), the results of this calculation are very useful for analyzing stacking-fault results. Figure 4.3 shows a significant rearrangement (when compared to the *fcc* case) of the states near 0.3 Ha. Also, the MTDOS peak nearest the Fermi level is broadened. There is, in the *hcp* structure, a five-percent decrease, relative to the *fcc* structure, in the spin polarization. The polarization is 0.583 μ_B within the muffin-tin and 0.567 μ_B within the Wigner-Seitz sphere. The calculated Fermi energy of *hcp* nickel, 0.35294 Ha, is slightly higher than the *fcc* counterpart. The exchange splitting observed in the *hcp* structure, 0.024 ± 0.001 Ha (0.65 eV), is nearly identical to that in the *fcc* system. The total energy is 101 mJ/m^2 per (111)-plane larger in the *hcp* phase than in the *fcc* structure, which is consistent with the fact that the structure of nickel is observed to be *fcc*.

The "ABC" notation[36] is used to describe the stacking of the (111) planes (figure 4.4). Each (111) plane forms a triangular lattice as shown by the sites labelled A in

figure 4.4. There are two distinct sites on which the next (111) plane can be stacked; these are labelled B and C. The *fcc* structure is built by stacking the planes in the sequence ABCABC and the *hcp* structure is constructed by stacking the planes in the sequence ABABAB. In the notation used below, the *fcc* structure is denoted by (...<ABC>...) where the angular brackets indicate that the structure within them is repeated to infinity in the direction indicated by the bracket immediately adjacent to the "...". Hence the *hcp* structure is denoted by (...<AB>...). The five types of stacking faults investigated are shown in figure 4.5 and are referred to as (a) a twin boundary fault (...<BCA>B<ACB>...), (b) an intrinsic fault (...<CAB><ABC>...), (c) an extrinsic fault (...<CAB>A<CAB>...), and, for lack of established names, (d) the super-extrinsic fault (...<BCA>CB<ABC>...), and (e) the hyper-extrinsic fault (...<BCA>CBA<CAB>...). In addition, the spin polarization and the total energy of (f) *dhcp* (...<ABAC>...) nickel are calculated. (The letters in figure 4.5 are staggered to help in visualizing the structure of the stacking faults.) The number of layers allowed to readjust in each calculation is the number of pictured layers less two (the two end layers were constrained to be bulk-like).

The muffin-tin spin polarization of the layers for each of the stacking-fault structures are presented in table 4.1. The muffin-tin spin polarization of the A layers of *dhcp* nickel [figure 4.5(f)] is 0.592 μ_B and that of the B and C layers is 0.612 μ_B. Muffin-tin spin polarizations are the only ones quoted in this thesis (unless otherwise indicated) since full-cell polarizations are unavailable. Approximations to the full-cell spin polarization, in the form of the polarization of the Wigner-Seitz sphere charge, indicate trends identical to those in the muffin-tin spin polarizations. The labelling of the layers in table 4.1 corresponds to the labelling of figure 4.5, where the first entry under each structure is the uppermost layer in figure 4.5. Since the polarization is symmetric about the midpoint of the fault (indicated by arrows in table 4.1), the table contains the results for only the upper half of each fault. For the interface calcula-

tions, the first entry in the table represents the layer constrained to be bulk-like. The values of the spin polarization for the layer immediately adjacent to the bulk suggest that the redjusted regions are sufficiently large. As expected, there are small changes in spin polarization caused by the presence of the stacking faults.

Table 4.2 contains the energies of the various configurations measured relative to the *fcc* structure. The energies of the *hcp* and *dhcp* systems are quoted in mJ/m^2 per (111) atomic plane, and the quoted stacking-fault energies are the total energy, in mJ/m^2, for the entire stacking-fault region.

The energy of a single twin boundary is 105 mJ/m^2. The calculation gives the same energy by allowing the readjustment of the potentials for six and for eight layers, which indicates convergence with respect to the number of layers in the readjusted region. The energies of the other investigated stacking faults are roughly twice the twin-boundary energy. There are two types of layers which appear in the stacking sequences. One type, which has the local symmetry (i.e. nearest- and next-nearest-neighbors) of the *hcp* lattice, trigonal prismatic, is referred to as a P-layer (e.g. the apex layer of a twin boundary fault). The other type, whose sites have the local symmetry of the *fcc* lattice, octahedral, is referred to as an O-layer. In addition to the stacking-fault energies, table 4.2 also contains the values of the function $\Delta(n)$:

$$\Delta(n) = 2\,E_{twin} - E_n$$

where E_{twin} is the energy of an isolated twin boundary fault, and E_n is the energy of a stacking fault composed of two P-layers separated by n planes (e.g. E_1 is the energy of the extrinsic fault, E_2 the energy of the super-extrinsic fault, and E_3 the energy of the hyper-extrinsic fault). This function measures the energy gained through the "interaction" between two P-layers. When separated by three planes, the P-layers behave nearly as if isolated, as can be seen from the fact that $\Delta(3) = 10$ (mJ/m^2), and that the spin polarization on the middle layer of the hyper-extrinsic fault is only

slightly reduced relative to the bulk.

Figure 4.6(a) pictures the hexagonal two-dimensional Brillouin zone used for the calculation. The dashed line demarcates the irreducible wedge over which the integrations are performed. It is instructive to locate the points in the two-dimensional zone onto which the symmetry points L, K and X of the full three-dimensional zone are projected. The projection points in the irreducible zone are shown in figure 4.6(b) where they are labelled by their corresponding three-dimensional labels. The Γ-point and one of the four L-points project onto $\bar{\Gamma}$. The three remaining L-points and the three X-points project onto $\bar{M}$. The K-points project onto two points in the irreducible wedge of the zone: one on the line joining $\bar{\Gamma}$ to $\bar{M}$ at a point three-quarters of the way to $\bar{M}$, and the other at a point of the $\bar{M}$ to $\bar{K}$ line, three-quarters of the way towards $\bar{K}$. Hence the K-points do not fall on any of the symmetry points of the two-dimensional zone. The Fermi surface of nickel[35] has a minority hole pocket near the X-point of the Brillouin zone. The distorted spherical surface of the minority-spin d-states intersects the Γ–L line roughly three-quarters of the way to L, and also passes near the K-point.

Figure 4.7 is the two-dimensional projection of the three-dimensional band structure of *fcc* nickel, plotted along the two-dimensional symmetry directions. The shaded regions of this figure correspond to points (E , κ) for which band states exist (κ is the two-dimensional wavevector). The white regions are gaps in (E , κ) space for which there are no band-like states. (A band-like state is said to exist if, after twenty layer doublings, the calculation of the T-matrix has not converged.) Truly localized states could appear only in these gaps. Evidently, there is the possibility of finding localized states in the immediate vicinities of $\bar{\Gamma}$ and $\bar{K}$, but not about $\bar{M}$. The symmetry points $\bar{\Gamma}$ and $\bar{K}$ were scanned for localized states in the energy range 0.1 Ha to 0.4 Ha.

The layer-projected MTDOS for the stacking-fault configurations were calculated and plotted for both $\bar{\Gamma}$ and $\bar{K}$ of the two-dimensional Brillouin zone. Figure 4.8 con-

tains the results for $\bar{\Gamma}$ of the twin boundary fault. The layers are labelled as in figure 4.5(a), with the uppermost curve being the $\bar{\Gamma}$-projected MTDOS of *fcc* nickel. The dotted line represents the Fermi energy. It is evident that there are no localized states. There is, however, a resonant state which appears at 0.299 (0.322) Ha in the majority (minority) spin. The exchange splitting for that state is 0.023 Ha. The spectral weight of this resonance is largest on the planes adjacent to the P-layer of the fault, which are also the planes with the smallest spin polarization. Note that there is some rearrangement of the minority-states near the Fermi level, but there is no obvious explanation of the decrease in the moment.

Figure 4.9 is the layer-projected MTDOS at $\bar{K}$ of the twin boundary fault, and is labelled in the same manner as figure 4.8. In contrast to figure 4.8, three localized states appear; one at 0.204 (0.221) Ha, one at 0.287 (0.309) Ha, and the other at 0.306 (0.329) Ha in the majority (minority) spin. These states have their maximum spectral strength at the P-layer of the fault, which is the layer with the bulk magnetic moment.

Figures 4.10 and 4.11 are the MTDOS at $\bar{\Gamma}$ and $\bar{K}$ of the extrinsic fault, labelled according to figure 4.5(c). The resonant state at $\bar{\Gamma}$ is present as are the localized states at $\bar{K}$. The resonance at $\bar{\Gamma}$, which appears at 0.297 (0.320) Ha in the majority (minority) spin, has its maximum spectral strength on the central O-layer of the fault; this O-layer exhibits the smallest spin polarization. The states localized at $\bar{K}$ appear at 0.204 (0.221) Ha, at 0.287 (0.309) Ha and at 0.305 (0.329) Ha in the majority (minority) spin. The exchange splitting for the states is similar to that in the twin boundary fault.

Table 4.3 depicts the energies and exchange splittings for the $\bar{\Gamma}$ resonance and the $\bar{K}$ localized states for the twin boundary, intrinsic, extrinsic, super-extrinsic and hyper-extrinsic faults. In the intrinsic and hyper-extrinsic faults there are actually four states localized at $\bar{K}$. Since all of the stacking faults except the twin boundary fault contain two P-layers, one might expect to find six states localized at the faults (at $\bar{K}$,

only two localized states at $\bar{\Gamma}$); each P-layer (twin boundary fault) should result in three states localized at $\bar{K}$. Interference between the states localized near different P-layers should introduce splittings into the states, resulting in six distinct energies. The majority-spin states at 0.307 and 0.304 Ha in the hyper-extrinsic fault (figure 4.12) are the result of interference between states localized on different P-layers. There are many possible reasons that six localized states are not observed at any of the stacking faults. One explanation is that the two states do in fact split, but that the companion state to the observed localized state is pushed into the continuum. Another alternative is that the some of the states are strongly localized and do not interact with the states localized on the other P-layer. This is certainly the case for the hyoer-extrinsic majority-spin (minority-spin) states at $\bar{K}$ at energies of 0.204 (0.221) and 0.287 (0.309) Ha. In contrast the majority-spin (minority-spin) states at $\bar{K}$ which lie at an energy of 0.306 (0.329) Ha in the twin boundary fault, are more extended; figure 4.9 indicates that, in the twin boundary fault, these states have a finite spectral strength as far as three (111) planes away. One might therefore expect that the two states, corresponding to those at 0.306 Ha in the twin boundary fault, localized on different P-layers, should mix and result in a double peak structure. Symmetry dictates that the peak arising from the antisymmetric state should have zero spectral strength on the central layer of the fault, which is the observed behavior (figure 4.12).

Table 4.4 contains the angular-momentum resolved muffin-tin charges for *fcc*, *hcp*, and *dhcp* nickel, and table 4.5 contains these charges for the layer in each stacking fault with the smallest spin polarization (the layers are labelled as in figure 4.5). The tables also contain the total muffin-tin charges, and the quantity $\Delta q_{\sigma l}$ which is defined to be the difference:

$$\Delta q_{\sigma l} = q_{\sigma l} - q_{\sigma l}^{fcc}$$

where $q_{\sigma l}^{fcc}$ is the muffin-tin charge with spin σ and angular-momentum l for the *fcc*

lattice, and $q_{\sigma l}$ is the corresponding quantity for the other lattices or stacking-fault structures. The next section of each table is the angular-momentum resolved contribution to the change in spin polarization

$$\Delta m_l = \Delta q_{min.\ l} - \Delta q_{maj.\ l} \quad .$$

The last line of each of the tables displays the total change in muffin-tin charge. A +(-) sign indicates that charge has gone in (out) of the muffin-tin compared to the muffin-tin charge in *fcc* nickel.

D. Analysis

It is important to determine the mechanism by which the stacking faults alter the spin polarization. Without an adequate explanation for the results it is difficult to determine whether or not the observed differences are indicative of real trends or merely a consequence of the numerical method used to obtain them. Moreover, a complete physical picture of stacking faults in nickel can be used to assess the importance of stacking faults in other systems.

It is argued below that the observed changes in spin polarization are physical. The calculated magnitudes of the changes, based on spin-density-functional theory, are not guaranteed to be given correctly, but the trends are most likely real.

The argument rests on three points. First, the change in spin polarization stems directly from a transfer of charge from the majority d-states to the minority d-states within the muffin tin. Second, the minority states at the fault partially responsible for the shifts in spin polarization are derived from band states with k directed along the Γ to L line of the three-dimensional *fcc* Brillouin zone, and are locally broadened and shifted by the close proximity of neighboring atoms in the [111] direction at the faults. And third, there is a symmetry induced rearrangement of the majority states nearest the Fermi level, whose changed filling, when combined with the changes that take place in the minority states, accounts for the decrease in spin polarization.

The first point of the argument can be established by inspection of tables 4.4 and 4.5. The angular-momentum resolved changes in spin polarization indicate that a major portion of the shift in polarization arises from the shift in occupation of the *d*-states. Furthermore, this shift in occupation far outweighs the total change in muffin-tin charge, $\Delta q_{muffin\ tin}$, indicating that the shift in polarization is not the result of a change in the amount of charge within the muffin-tin. For example, in going from the *fcc* to the *hcp* structure, the total change in spin polarization is 0.031 μ_B, while the change in the polarization of the *d*-states is 0.032 μ_B. (The combined change in polarization of the *s*- and *p*-states is -0.001 μ_B.) In contrast, the change in muffin-tin charge can only account for a change in spin polarization of 0.001 μ_B. Even in the intrinsic stacking-fault, which shows the largest change in muffin-tin charge, $\Delta q_{muffin\ tin}$ can only account for one-third of the shift in the reported muffin-tin spin polarization. Further comparisons of tables 4.4 and 4.5 show that in all cases the change in spin polarization arises almost entirely from shifts in *d*-electron occupation.

Careful inspection of table 4.1 reveals an important fact. The symmetry of the potential from the nearest- and next-nearest neighbors has little influence on the spin polarization. For example, the nearest- and next-nearest neighbors of atoms in the P-layer of the twin boundary fault [i.e. layer B in the stacking (...<BCA>B<ACB>...)] all occupy the positions they would occupy in the *hcp* lattice but the atoms on this layer all have the spin polarization of the *fcc* bulk. The atoms on the layers immediately adjacent to the the P-layer [i.e. the O-layer A in the stacking (...<BCA>B<ACB>...)] have their first- and second-neighbors in the positions they would occupy in the *fcc* lattice, but the spin polarization on these layers is reduced relative to the bulk *fcc* value. Hence the spin polarization behaves in a fashion exactly the opposite of what one would naively expect from local-structure arguments.

A dependence of the spin polarization on the disorder in the [111] direction is expected. It is not, however, obvious that the positions of the nearest- and next-

nearest-neighbor atoms would play no role in determining the magnitude of the polarization. The physical interpretation of this result is that in this close-packed configuration, the potential from these neighbors is so nearly spherical that their exact positions do not matter. It may be argued that, because spherical potentials form the very premise of the muffin-tin approach, the calculations are merely internally consistent. While a full potential calculation may slightly alter the results presented here, it seems unlikely that inclusion of non-spherical terms in the potentials would significantly change the observed trends.

Table 4.1 contains further clues to the origins of the changes in spin polarization. Consider the orientations of the third-neighbor sites of an atom near the stacking-fault. In the *fcc* lattice, the third-neighbors are located at the twenty-four sites equivalent to $a/\sqrt{2}$ [211], where a is the nearest-neighbor spacing. (None of these sites lie in the [111] direction.) In the *hcp* lattice, there are only two third-nearest neighbors: one at $a\sqrt{(8/3)}$ [0001] and the other at $a\sqrt{(8/3)}$ [000$\bar{1}$]. Both of these sites lie in the direction equivalent to the [111] direction of the *fcc* lattice.

The polarization of a layer is strongly correlated with the distance to the nearest-neighbors in the [111] direction. Consider the structure of the nearest-neighbors, in the [111] direction, of the twin boundary fault (...<BCA>B<ACB>...). For the central B layer, the P-layer with the bulk *fcc* spin polarization, the nearest-neighbors in the [111] direction are at a distance of $a\sqrt{6}$, the distance at which they would be found in the *fcc* lattice. For the adjacent O-layers labelled A, one of the neighbors in the [111] direction lies at a distance of $a\sqrt{6}$, but the other is thirty-three percent closer, lying at a distance of only $a\sqrt{(8/3)}$. The spin polarization on this layer is smaller than the *fcc* bulk value. In the stacking sequence of the extrinsic fault, the central A layer has its two nearest-neighbors in the [111] direction in the positions they would occupy in *hcp* lattice [at a distance $a\sqrt{(8/3)}$], and the spin polarization of this layer is essentially that found for the bulk *hcp* calculation.

The dependence on the distance to the nearest neighbor in the [111] direction can be understood physically using the following arguments. In general, keeping all other factors constant, a decrease in lattice spacing results in an increase in bandwidth. While the nearest-neighbor lattice spacing is unchanged when going from the *fcc* to the *hcp* lattice, the spacing of atoms in the [111] direction ([000$\bar{1}$]-direction of the *hcp* lattice) decreases. One might therefore expect that the band formed of states with **k** along the Γ to L direction of the *fcc* Brillouin zone should be broadened by the effective increase in density of cores in this direction. (The corresponding decrease in effective density in other directions should also lead to band narrowing, but unless the bands near the Fermi level are altered, the spin polarization would not be affected.) The Stoner model, in which magnetism arises from the competition between electron-electron interactions and single-particle bandwidths, and the simple rules suggested in reference 20, imply that this broadening would be accompanied by a smaller spin polarization.

Figure 4.13(a) is the MTDOS at $\overline{\Gamma}$ for the *fcc* (dashed line) structure and the *hcp* (solid line) structure. The vertical dotted line represents the Fermi level of *hcp* nickel; the Fermi level of *fcc* nickel is almost indistinguishable at this scale. There are two important observations to be made. First, the minority-spin peak nearest the Fermi level lies *above* the Fermi level in the *fcc* structure and completely *below* the Fermi level for the *hcp* case. This rearrangement of states would certainly contribute to the calculated decrease in spin polarization in *hcp* nickel, although there must be a corresponding rearrangement of majority-spin states. The second observation, that the band nearest the Fermi level is broadened in the *hcp* structure, is consistent with the simple discussion above. This broadening suggests that the new equilibrium point in the trade off between electron-electron interactions and bandwidth has a smaller spin polarization.

Since the spin polarization decreases in the *hcp* structure, majority-spin states

must be pushed above the Fermi level. Figure 4.13(b) is the MTDOS at $\overline{M}$ for the *fcc* and *hcp* systems. The most important feature of this figure is the strong peak in the majority-spin states of the *hcp* structure which lies well above the Fermi level, and is absent in the MTDOS of the *fcc* structure. In addition, a gap has opened in the majority-spin states at the Fermi level. As shown in figure 4.6, the points X and L of the three-dimensional *fcc* Brillouin zone project onto $\overline{M}$.

It is useful to understand the symmetries of the states responsible for the majority-spin peak above the Fermi level. Figure 4.14 is a plot of the band structure of *fcc* nickel plotted along a line parallel to the [111] direction and passing through $\overline{M}$. The majority-spin bands are indicated by a solid line and the minority-spin bands indicated by a dashed line. The X and L symmetry points are clearly visible. The source of the minority-spin Fermi surface hole pockets near X are also visible. The majority d-states nearest the Fermi level lie along the X to W line. The small group[37] of the X-point is D_{4h}; three of the d-states transform according to one-dimensional representations, and the remaining d-states transform according to the only two-dimensional representation of this group. The small group of the L-point is D_{3d}; there are two sets of doubly degenerate d-bands, and one nondegenerate d-band.

The band structure of *hcp* nickel plotted along the line L-M-L of the three-dimensional *hcp* Brillouin zone is shown in figure 4.15. The majority-spin band responsible for the peak above the Fermi level in the *hcp* MTDOS at $\overline{M}$ is clearly visible. The small group of the states along the L-M direction (not at the symmetry points) is C_{2v}; all the representations of this group are one-dimensional.

While it is not possible to make a precise comparison between the two band structures, it is possible to do a rough analysis of the effects of change in symmetry on going from the *fcc* to the *hcp* lattice. Since the span of the *hcp* Brillouin zone in the [0001] direction is exactly one-half the span of the *fcc* zone in the [111] direction, the band structures can be "compared". The majority states above the Fermi level at $\overline{M}$

are derived from the mixing of states at L and X of the *fcc* Brillouin zone, a mixing which is induced by the change in symmetry on going from the *fcc* structure to the *hcp* structure.

Group theoretical arguments can be used to understand further the changes taking place. Consider the two majority-spin bands nearest the Fermi level. When the structure goes from *fcc* to *hcp,* these two bands become four, because the size of the unit cell doubles. At the same time, however, the degeneracies imposed by the symmetry of the *fcc* structure are lifted; the formerly doubly-degenerate states are now split. Three of the four majority bands now lie completely below the Fermi level, but the fourth has moved completely above it. This is the source of the decreased occupation of the majority d-states.

Hence the difference in spin polarization between *fcc* and *hcp* nickel results from complex changes in symmetry and the proximity of atoms in the [111] direction (of the *fcc* crystal). Since stacking faults are essentially *hcp*-like structures embedded in an *fcc* medium, it is possible to extend the above arguments to the stacking fault configurations.

The spin polarization on any layer of a stacking fault is influenced by the same environmental factors that drive the decrease in spin polarization on going from *fcc* to *hcp* nickel. The proximity of atoms in the [111] direction results in a local broadening of the states (derived from the band states of the perfect crystal with **k** along the Γ to L directions) and a corresponding decrease in the spin polarization. The local broadening of the states nearest the Fermi level at $\overline{\Gamma}$ is clearly shown in both figures 4.8 and 4.10 (the $\overline{\Gamma}$-resonance adds considerably to the width). The increased occupation of the minority states is also clearly visible in the lowest panel of figure 4.10, which corresponds to the central layer of the extrinsic fault (the layer with a spin polarization very close to that of the *hcp* calculation). This increase is not as visible in the remaining layers of the fault, nor is it as visible in the twin boundary fault,

probably because the changes are very small.

Figure 4.16 is the layer-projected MTDOS at $\overline{M}$ for the extrinsic fault. It is clear that there is a significant rearrangement of the states near the fault over the displayed range of energy. Of particular interest is the rearrangement of the majority-spin states above and near the Fermi level. The lowest panel of this figure, which show the MTDOS for the central layer of the extrinsic fault, contains a pronounced "bump" in the majority states which corresponds to the peak above the Fermi level in the *hcp* case (figure 4.13). The fact that this "bump" is more sharply defined on this layer than on any other suggests that, for the states which compose this peak, the structure in the [111] direction is important, particularly the proximity of other atoms. The enhancement of the "bump" on the layers of type A, which have one neighbor in the [111] direction at the *hcp* distance, is consistent with this conclusion.

The calculated effects are very small, partly because the defect itself represents a subtle change in local structure and symmetry, and not a chemical change. The small size of the effects requires examination of the approximations entering the calculation. A brief discussion of the effects of the muffin-tin approximation and of the neglect of the spin-orbit interaction has already been given above. There is another source of uncertainty; the positions of the sites in the interface were not allowed to relax to minimize the internal energy. Since the arguments above are based on the fact that a stacking fault brings the atoms situated along the [111] direction closer, and that this results in the change in spin polarization, a relaxation of the lattice could be effective in reducing the calculated effects. However, it is unlikely that relaxation can completely cancel the thirty-three percent change in spacing, and the calculated trends most likely indicate the physical reality. On the other hand, the decrease in moment at a stacking-fault represents a shift towards a "wider bandwidth" at the expense of exchange-correlation energy; relaxation should shift the system back towards a "narrower bandwidth" (i.e. the relaxation should result in an expansion, along the [111]

direction, of the solid near the stacking fault). This relaxation, if real, could be observed by diffraction methods.

The argument presented above makes, qualitative, definite predictions for other stacking sequences. The electronic structures of the stacking sequences shown in figure 4.17 were calculated as a test for the analysis. [The potentials of all the pictured layers were allowed to readjust (not relax) for the presence of the fault.] Both of these structures are based on hypothetical *hcp* nickel. These structures have been calculated only for comparison of the spin polarizations the atomic positions have been fixed. (The *hcp* system is highly *unstable* and will spontaneously form the types of defects shown here; *hcp* nickel is *not* a metastable state.) Each of these stacking sequences contains a layer of atoms that do not have any neighbors, at any distance, along the [111] and $[\overline{111}]$ directions, the layers labelled C in the figure. The previous discussion indicates that the states on these layers should be very narrow, and that the spin polarizations should be enhanced. These results are indeed borne out by the calculations. The muffin-tin spin polarization of the layer C of the structure 4.17(a) is 0.622 μ_B and that of layer C of the structure 4.17(b) is 0.635 μ_B.

Figure 4.18 is the layer-projected MTDOS at $\overline{\Gamma}$ of the structure shown in figure 4.17(b). There is a state, localized at the defect, split off from the top of the minority-band states that appears *above* the Fermi level. The apparent width of the states is noticeably narrower on the singular layer C. This is physically reasonable since there are no states in the [111] direction which can couple to the states on the central layer (C).

Figure 4.19 is the layer-projected MTDOS at $\overline{M}$ for the same structure as in figure 4.18. The pronounced peak above the Fermi level in the majority-spin states of bulk *hcp* nickel (a smaller peak does appear at the fault) is substantially reduced on the central layer (the peak in the minority-spin states is also markedly reduced). The absence of the majority-spin peak, coupled with the appearance of a localized

minority-spin state above the Fermi level at $\bar{\Gamma}$, suggests that the spin polarization on layer C should be noticeably enhanced. In fact, the calculated spin polarization is enhanced by eight percent over the value calculated for *hcp* nickel.

The mechanism described above depends sensitively on the details of the electronic structure of nickel. For example, if the minority-spin band broadened by the proximity of atoms in the [111] direction did not cross the Fermi level, the stacking fault may not influence the magnetic properties of the fault. However, the band structure of cobalt has some of the features responsible for the shifts in spin polarization predicted in nickel. Figure 4.20 is the band structure of cobalt, taken from Papaconstantopoulos' book,[38] plotted along the *M*-*L* and the Γ-*A* directions of the *hcp* Brillouin zone. The band structure of the majority spin along *M*-*L* is very similar to that of *hcp* nickel. The band structure of the minority spin along Γ-*A* differs slightly from that of nickel: there is an almost completely empty band. It is not clear how stacking faults would affect the spin polarization in this system, but if the result of the stacking fault is to narrow the local bandwidth of the states along the Γ-*A* direction, and to shift the average energy to a higher value (these are the effects expected from the nickel calculation), the changes in spin-polarization could be similar in absolute magnitude to those calculated for nickel. These changes, however, represent a small percentage change, and would probably be more difficult to detect experimentally.

The decrease in spin polarization of the layers near a stacking fault implies that stacking faults interact with magnetic domain boundaries, since the energy of these domain boundaries depends directly on the magnitude of the spins.[39] The calculations presented here give little information about the details of this interaction, because the anisotropy energy is not included.

E. Simple Empirical Relations

As discussed in section D, the spin polarization density of a stacking fault is most sensitive to the distribution of atoms along the preferred [111] direction, and is not

very sensitive to the orientation of nearest- and next-nearest-neighbor pairs. This dependence can be described quantitatively. The spin polarization of any layer can be fitted to an expression of the form:

$$\mu = M_o + \sum_{i=2}^{3} \eta_i \ \alpha_i$$

where μ is the spin polarization on the layer under consideration, η_i is the number of layers, i layers away, which are identical to the layer under consideration (e.g. for the *fcc* structure, $\eta_2 = 0$ and $\eta_3 = 2$ while for the *hcp* case, $\eta_2 = 2$ and $\eta_3 = 0$). From structural considerations $\eta_1 = 0$ always. The parameters M_o, α_2 and α_3 are fitted to the results of all calculations based on the *fcc* bulk structures [figures 4.5(a)-(e)] and their values are contained in table 4.6. The results of this formula are compared with the LKKR values in figures 4.21 and 4.22. The fit accurately reproduces the trend in spin polarization for all the faults. The fit places the moment for *fcc* nickel at 0.610 μ_B.

The energy of the stacking faults can also be modelled by a simple linear fitting scheme. The energy of the stacking faults is fitted to the following expression

$$E = \sum_{layers} \left\{ E_L + \sum_{i=2}^{i=4} \xi_i \ \gamma_i \right\}$$

where E_L takes the value $E_O = 0$ for an octahedral layer, and E_P for a trigonal prismatic layer; ξ_i is the number of planes located at a distance of i planes away which are different from what they would be in the *fcc* case (e.g. $\xi_2 = 2$, $\xi_3 = 2$, and $\xi_4 = 2$ for the *hcp* lattice). The parameters E_P and the various γ_i are energies to be fitted to the complete calculation. The values of the fitting parameters, calculated by fitting to the energies of the *fcc* based structures in figure 4.5(a)-4.5(e) are contained in table 4.7. Table 4.8 shows the results of the fit. The fits are reasonable approximations to the energies of the respective faults. This simple expression for the energy

may be useful for quick, "back-of-the-envelope" thermodynamic calculations.

F. Conclusion

The electronic and magnetic properties of [111] stacking faults in nickel are calculated utilizing a fully self-consistent LKKR formalism which does not require finite-sized slabs or periodic boundary conditions. Localized states are found at all the faults studied.

The spin polarization depends on the structure of the fault and shows roughly a five percent change in going from *fcc* stacking to *hcp* stacking. The exact positions of the nearest- and next-nearest neighbors is not important for determining the spin polarization on a site; the near spherical structure of the close-packed configuration assures that this is the case. Rather, the spin polarization depends most strongly on the distance to the nearest atom in the [111] direction, and decreases as this distance is decreased.

The dependence of the spin polarization is analyzed through a comparison between the electronic and magnetic structures of *fcc* nickel and (hypothetical, *unstable*) *hcp* nickel (with the identical nearest-neighbor spacing). The difference in spin polarization between these two structures is the result of two major effects. The first is a broadening of the band formed of states with **k** along the Γ to L line of the *fcc* Brillouin zone on transforming form the *fcc* to the *hcp* structure. This broadening is linked to the higher density of atoms in the [0001]-direction (equivalent to the [111] direction of the *fcc* system). The second effect is the loss of cubic symmetry which results in the splitting of formerly degenerate bands. The resulting rearrangement of the states results in the movement of a portion of the majority spin band to above the Fermi level, while the broadened minority band moves completely below. The net effect of this rearrangement of states is to shift electrons from d-like majority states to d-like minority states.

It is further argued that the spin polarization of the stacking faults can be understood by analogy with the results of the *fcc* and *hcp* calculations. The presence of neighbors in the [111] direction results in a local broadening of the density of states, which is accompanied by a local decrease in spin polarization. Even though the effects are small, the trends are believed to be real and will remain even after the lattice is allowed to relax.

It is also suggested that the same type of phenomena might be present in cobalt stacking faults. This system represents a significantly different physical situation because the ground state of cobalt is the *hcp* structure. Nevertheless, the band structure of cobalt, as calculated by Papaconstantopoulos, shows features similar to those which determine the spin polarization of hypothetical *hcp* nickel.

Since the energy of a Bloch wall depends on the magnitude of the spins, it is likely that magnetic domain walls will couple to stacking defects. However, since the anisotropy energy of the faults is not included, no attempt has been made to analyze this interaction.

Finally, simple empirical formulas are developed to describe both the spin polarization and the internal energy of any stacking configuration. The very simple formula for the spin polarization gives quantitatively reasonable results. A similar formula applied to the internal energy yields a reasonable fit for all structures tested. It should provide a simple means for doing thermodynamic calculations of the concentrations of various stacking configurations.

G. References for Chapter IV

1 R. M. Stratt and B.-C. Xu, Phys. Rev. Lett. 62 , 1675 (1989).

2 X.-G. Zhang and A. Gonis, Phys. Rev. Lett. 62 , 1161 (1989).

3 S. Blügel, M. Weinert, and P.H. Dederichs, Phys. Rev. Lett. 60 , 1077 (1988).

4 C. L. Fu, A. J. Freeman, and T. Oguchi, Phys. Rev. Lett. 54 ,2700 (1985).

5 C. L. Fu and A. J. Freeman, Phys. Rev. B 33 , 1611 (1986).

6 Roy Richter, J. G. Gay, and John R. Smith, Phys. Rev. Lett. 54 , 2704 (1985).

7 J. Tersoff and L. M. Falicov, Phys. Rev. B 26 , 6186 (1982).

8 R. H. Victora and L. M. Falicov, Phys. Rev. B 31 , 7335 (1985).

9 A. J. Freeman and C. L. Fu, J. Appl. Phys. 61 , 3356 (1987).

10 J. G. Gay and Roy Richter, J. Appl. Phys. 61 , 3362 (1987).

11 C. H. Lee, Hui He, F. Lamelas, W. Vavra, C. Uher, and Roy Clarke, Phys. Rev. Lett. 62 , 653 (1989).

12 H. C. Siegmann, Physics Reports 17 , 37 (1975).

13 M. Campagna, D. T. Pierce, F. Meier, K. Sattler, and H. C. Siegmann, Adv. Electron. Electron Phys. 41 , 113 (1976).

14 M. Stampanoni, A. Vaterlaus, D. Pescia, M. Aeschlimann, F. Meier, W. Dürr, and S. Blügel, Phys. Rev. B 35 , 10380 (1988).

15 W. Drube and F. J. Himpsel, Phys. Rev. B 35 , 4131 (1987).

16 D. E. Eastman, F. J. Himpsel, and J. A. Knapp, Phys. Rev. Lett. 40 , 1514 (1978).

17 *Magnetic Properties of Low-dimensional Systems,* edited by L. M. Falicov and J. Moran-Lopez, (Springer Verlag, Heidelberg, 1986).

18 R. E. De Wames, Phys. Stat. Sol. 39 , 445 (1970).

19 D. L. Abraham and H. Hopster, Phys. Rev. Lett. 62 , 1157 (1989).

20 W. Dürr, M. Taborelli, O. Paul, R. Germar, W. Gudat, D. Pescia, and M. Landolt, Phys. Rev. Lett. 62 , 206 (1989).

21 D. Mauri, D. Scholl, H. C. Siegmann, and E. Kay, Phys. Rev. Lett. 62 , 1900 (1989).

22 L. M. Falicov, R. H. Victora, and J. Tersoff, in *The Structure of Surfaces,* edited by M. A. Van Hove and S. Y. Tong, (Springer Verlag, Heidelberg, 1985), p. 12.

23 L. E. Klebanoff, R. H. Victora, L. M. Falicov, and D. A. Shirley, Phys. Rev. B 32 , 1997 (1985).

24 L. M. Falicov and G. A. Somorjai, Proc. Natl. Acad. Sci. 82 , 2207 (1985).

25 Felix Yndurain and L. M. Falicov, Phys. Rev. Lett. 37 , 928 (1976).

26 W. R. Grise, Leonard Kleinman, and Kenneth Mednick, Phys. Rev. B 22 , 1729 (1980).

27 J. B. Pendry, *Low Energy Electron Diffraction,* (Academic Press, London, 1974).

28 M. Weinert, J. Math. Phys. 22 , 2433 (1981).

29 O. Gunnarsson and B. I. Lundqvist, Phys. Rev. B 13 , 4274 (1976).

30 L. Hedin and B. I. Lundqvist, J. Phys. C: Solid State Phys. 4 , 2064 (1971).

31 D. D. Koelling and B. N. Harmon, J. Phys. C: Solid State Phys. 10 , 3107 (1977).

32 J. M. MacLaren, S. Crampin, D. D. Vvedensky, and J. B. Pendry, Phys. Rev. B, in press.

33 C. S. Wang and J. Callaway, Phys. Rev. B 9 , 4897 (1974).

34 V. L. Moruzzi, J. F. Janak, and A. R. Williams, *Calculated Electronic Properties of Metals* (Pergamon Press Inc., New York, 1978).

35 C. S. Wang and J. Callaway, Phys. Rev. B 15 , 298 (1977).

36 C. Barrett and T. B. Massalski, *Structure of Metals* (McGraw-Hill, New York, 1965), 3rd. ed., pp. 387 - 390, 440-453.

37 G. F. Koster, in *Solid State Physics*, edited by F. Seitz and D. Turnbull, (Academic Press, New York, 1957), p. 173.

38 D. A. Papaconstantopoulos, *Handbook of the Band Structure of Elemental Solids*, (Plenum Press, New York, 1986).

39 C. Kittel, *Introduction to Solid State Physics*, (Wiley, New York, 1986).

H. Tables for Chapter IV

Table 4.1

Muffin-Tin Spin-Polarization (μ_B)									
twin		int.		ext.		sup. ext.		hyp. ext.	
lay.	pol.	lay.	pol.	lay.	pol.	lay.	pol.	lay.	pol.
A	0.614	A	0.614	A	0.614	A	0.614	A	0.614
B	0.611	B	0.609	B	0.610	B	0.609	B	0.607
C	0.611	C	0.609	C	0.607	C	0.596	C	0.599
A	0.603	A	0.597	A	0.595	A	0.606	A	0.608
→B	0.614	B	0.594	B	0.598	C	0.595	C	0.600
		→		→A	0.582	→		→B	0.604

Table 4.2

system	energy (mJ/m^2)	n	$\Delta(n)$ (mJ/m^2)
hcp	101		
dhcp	54		
twin	105		
intrinsic	176	0	34
extrinsic	161	1	49
super-extrinsic	160	2	50
hyper-extrinsic	200	3	10

Table 4.3

Energies and Exchange Splitting of Interface States

all energies are in Ha and are accurate to ±0.001 Ha

	Γ			*K*		
fault	maj.	min.	split.	maj.	min.	split.
twin	0.299	0.322	0.023	0.204	0.221	0.017
				0.287	0.309	0.022
				0.306	0.329	0.023
intrinsic	0.296	0.320	0.024	0.202	0.219	0.017
				0.285	0.306	0.021
				0.292	0.315	0.022
				0.311	0.335	0.024
extrinsic	0.297	0.321	0.024	0.204	0.221	0.017
				0.287	0.309	0.022
				0.305	0.329	0.024
super-extrinsic	0.299	0.322	0.023	0.204	0.221	0.017
				0.287	0.309	0.022
				0.306	0.329	0.023
hyper-extrinsic	0.299	0.322	0.023	0.204	0.221	0.017
				0.287	0.309	0.022
				0.304	0.328	0.024
				0.307	0.330	0.023

Table 4.4

Muffin-Tin Charges (electrons)

	l	*fcc*	*hcp*	*dhcp*	
layer				A	B
majority	s	0.2401	0.2403	0.2398	0.2405
spin	p	0.2369	0.2353	0.2355	0.2381
	d	4.4735	4.4601	4.4635	4.4719
minority	s	0.2447	0.2433	0.2442	0.2440
spin	p	0.2533	0.2521	0.2516	0.2549
	d	3.8387	3.8572	3.8514	3.8393
total	s	0.4848	0.4836	0.4840	0.4845
	p	0.4902	0.4874	0.4871	0.4930
	d	8.3122	8.3173	8.3149	8.3112
total		9.2872	9.2883	9.2860	9.2887
$\Delta q_{maj.\ l}$	s	0.0000	0.0002	-0.0003	0.0004
	p	0.0000	-0.0016	-0.0014	0.0012
	d	0.0000	-0.0134	-0.0100	-0.0016
$\Delta q_{min.\ l}$	s	0.0000	-0.0014	-0.0005	-0.0007
	p	0.0000	-0.0012	-0.0017	0.0016
	d	0.0000	0.0185	0.0127	0.0006
Δm_l	s	0.0000	-0.0016	-0.0002	-0.0011
	p	0.0000	0.0004	-0.0003	0.0004
	d	0.0000	0.0319	0.0227	0.0022
$\Delta q_{muffin\ tin}$		0.0000	0.0011	-0.0012	0.0015

Table 4.5

Muffin-Tin Charges (electrons)

layer	l	twin A	int. B	ext. A	sup. ext. C	hyp. ext. C
majority	s	0.2400	0.2340	0.2398	0.2400	0.2400
spin	p	0.2358	0.2358	0.2338	0.2352	0.2359
	d	4.4689	4.4647	4.4595	4.4657	4.4662
minority	s	0.2444	0.2438	0.2440	0.2443	0.2443
spin	p	0.2528	0.2532	0.2522	0.2534	0.2525
	d	3.8445	3.8493	3.8547	3.8477	3.8466
total	s	0.4844	0.4778	0.4838	0.4843	0.4843
	p	0.4886	0.4890	0.4860	0.4886	0.4884
	d	8.3134	8.3140	8.3142	8.3134	8.3128
total		9.2864	9.2808	9.2840	9.2863	9.2855
$\Delta q_{maj.\ l}$	s	-0.0001	-0.0061	-0.0003	-0.0001	-0.0001
	p	-0.0011	-0.0011	-0.0031	-0.0017	-0.0010
	d	-0.0046	-0.0088	-0.0140	-0.0078	-0.0073
$\Delta q_{min.\ l}$	s	-0.0003	-0.0009	-0.0007	-0.0004	-0.0004
	p	-0.0005	-0.0001	-0.0011	0.0001	-0.0008
	d	0.0058	0.0106	0.0160	0.0090	0.0079
Δm_l	s	-0.0002	0.0052	-0.0004	-0.0003	-0.0003
	p	0.0006	0.0010	0.0020	0.0018	0.0002
	d	0.0104	0.0194	0.0300	0.0168	0.0152
$\Delta q_{muffin\ tin}$		-0.0008	-0.0064	-0.0032	-0.0009	-0.0017

Table 4.6

spin polarization Fitting Parameters based on the fcc structures (in μ_B)	
M_o	0.604
α_2	-0.010
α_3	0.003

Table 4.7

Energy Fitting Parameters (mJ/m^2)	
E_P	55
γ_2	9
γ_3	-9
γ_4	11

Table 4.8

system	LKKR energy (mJ/m^2)	fitted energy (mJ/m^2)
twin	105	101
intrinsic	176	180
extrinsic	161	180
super-extrinsic	160	158
hyper-extrinsic	200	202

I. Figures for Chapter IV

Figure 4.1 A schematic diagram depicting the embedding procedure used in calculating the electronic structure of stacking faults. The lines represent planes of atoms. The light grey areas represent the bulk, which extends to infinity both above and below the stacking fault. The dark grey area is the region of space containing the stacking defect in which the potentials are allowed to readjust. This region is restricted by the boundary condition that it have the structure of the bulk at the light-grey dark-grey interface. Although this restriction represents an approximation, the approximation can be made as accurate as one would like by merely allowing the dark region to grow.

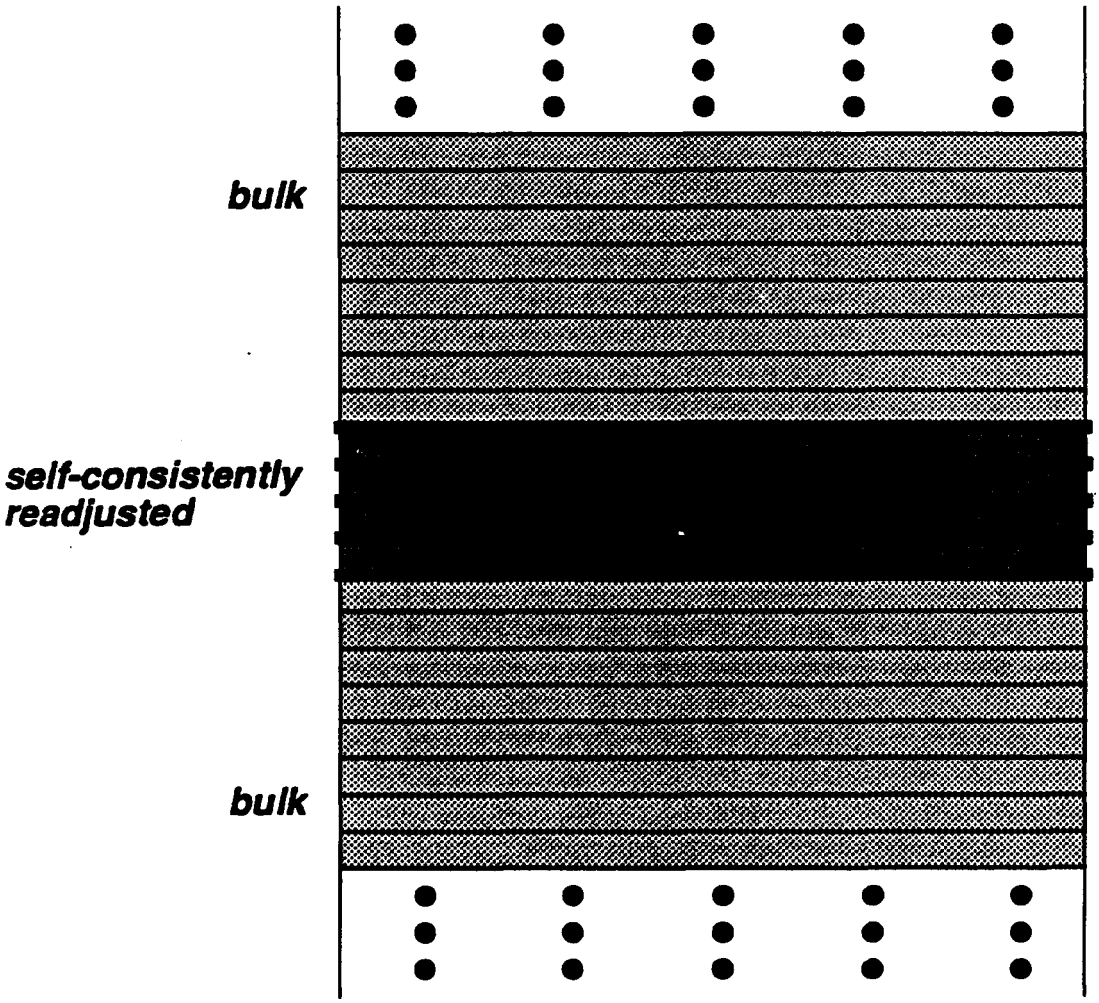

Figure 4.1

Figure 4.2 The muffin-tin density of states (MTDOS) for bulk nickel for both minority and majority states. The dashed vertical line represents the Fermi energy.

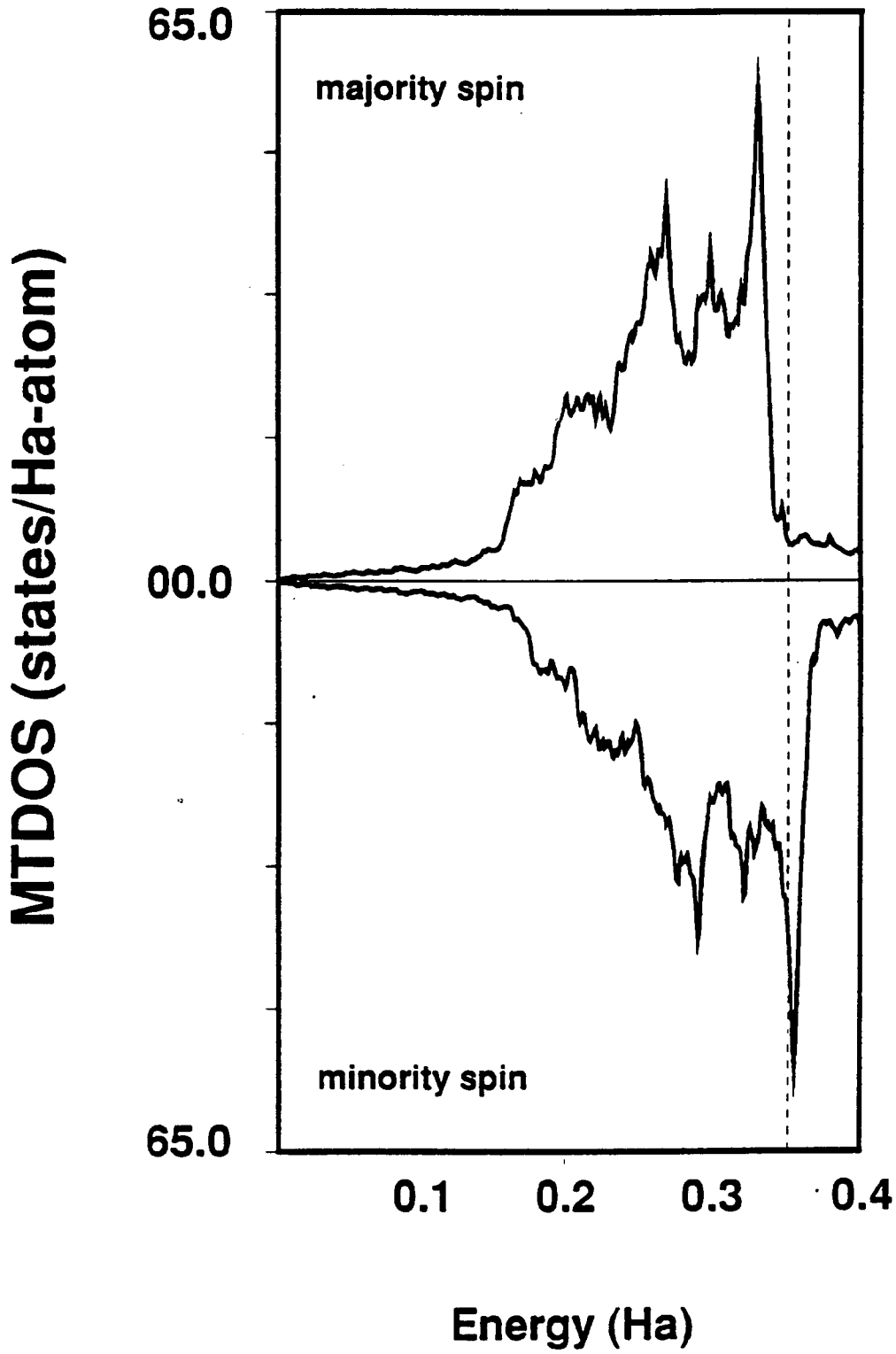
65.0
majority spin
00.0
minority spin
65.0
0.1
0.2
0.3
0.4
MTDOS (states/Ha-atom)
Energy (Ha)

Figure 4.2

Figure 4.3 The muffin-tin density of states (MTDOS) for hypothetical *unstable hcp* nickel. The dashed vertical line represents the Fermi energy. There are several differences between this MTDOS and that of figure 4.2. There is a significant rearrangement of the state near 0.3 Hartrees and the peak nearest the Fermi level is broadened in the *hcp* structure.

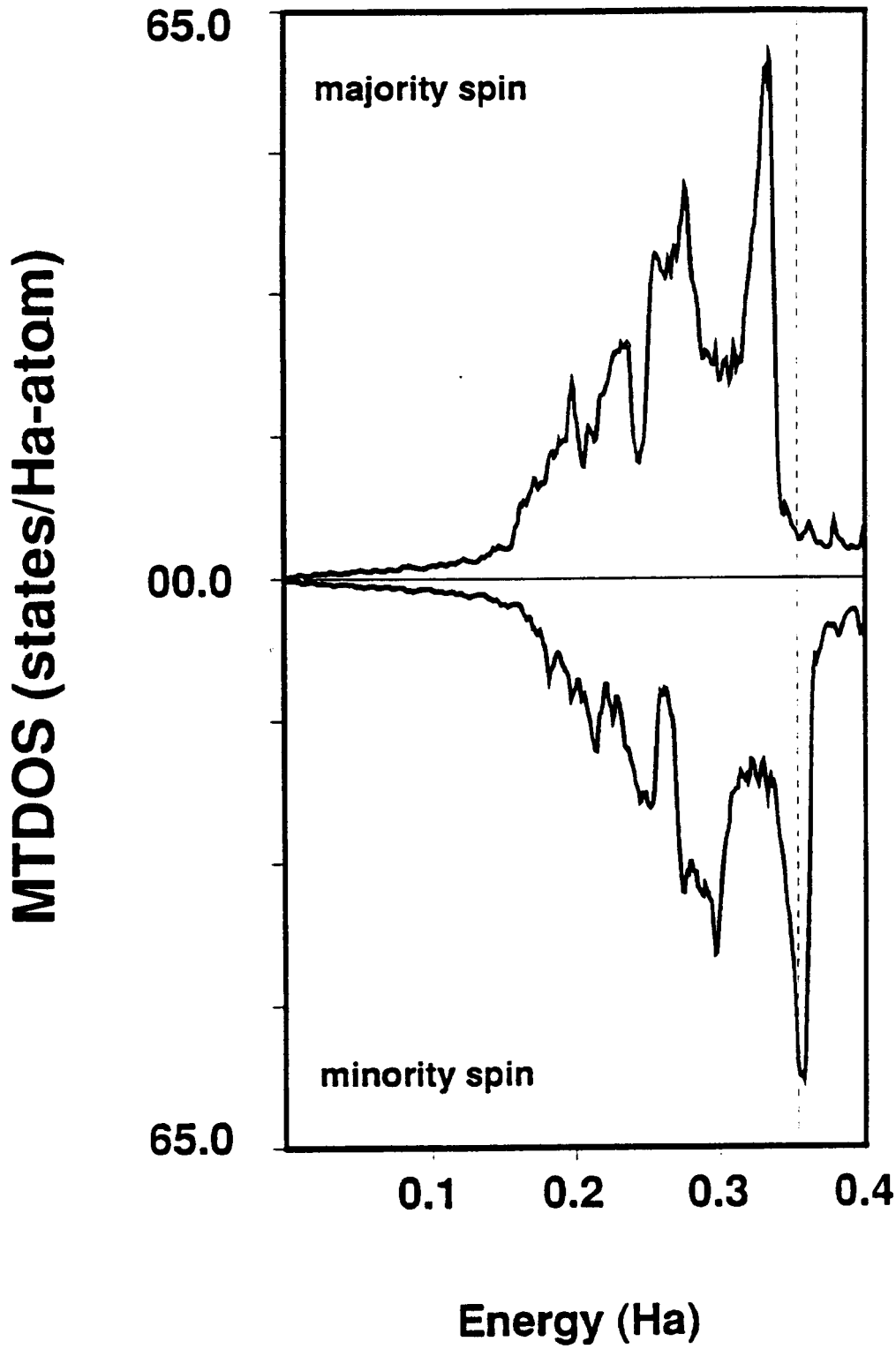
65.0
majority spin
00.0
minority spin
65.0
0.1
0.2
0.3
0.4
MTDOS (states/Ha-atom)
Energy (Ha)

Figure 4.3

Figure 4.4 A diagram depicting the sites A, B, and C for the stacking notation. In this figure, the grey circles are sites labelled A. They form the simple triangular lattice of the {111} planes of the *fcc* structure. When stacking another plane on this one (in the close-packed configuration) there are two possible sites, represented by the grey squares labelled B and the white triangles labelled C. The layers can be stacked in any random order as long as they satisfy the constraint that no layer is stacked immediately above a layer of its own type. The *fcc* lattice is created by stacking the layers ABCABC..., and the *hcp* lattice is created by stacking the layers ABABAB....

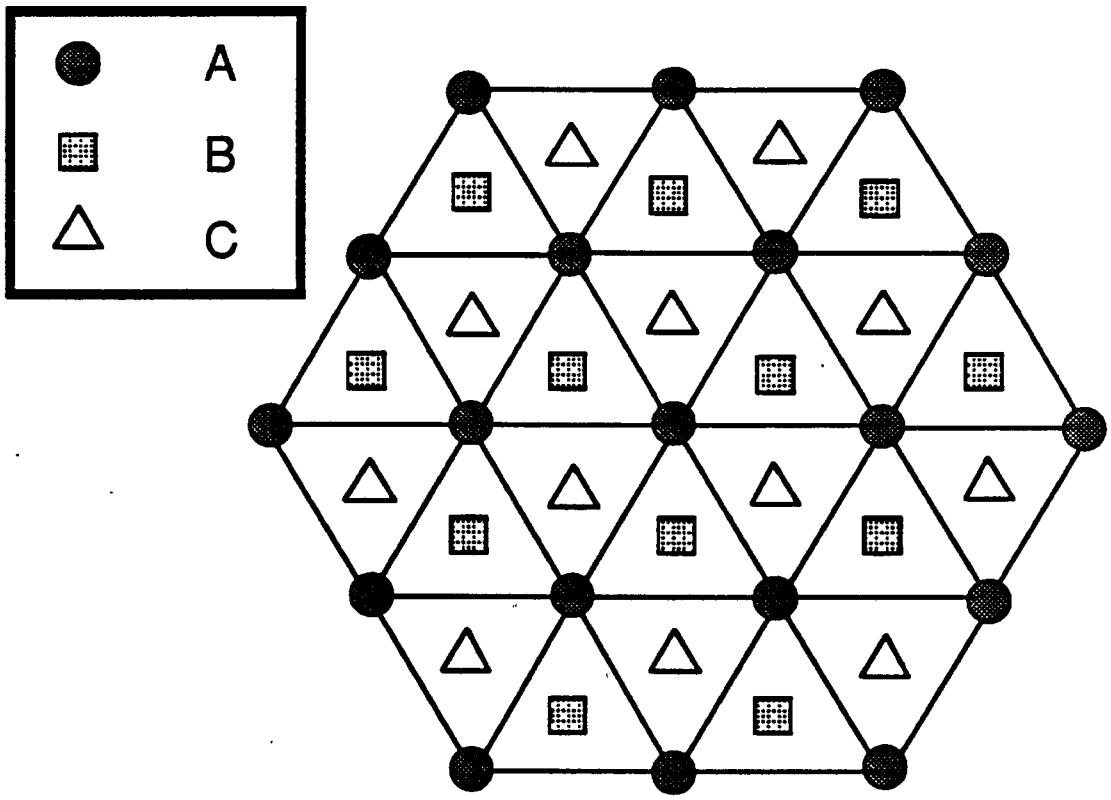

Figure 4.4

Figure 4.5 The stacking sequences investigated in this paper. The "..." in (a)-(e) indicates that the *fcc* stacking sequence continues to infinity. The "..." for (f) indicates that the stacking sequence shown is repeated to infinity. The structure in (a) is referred to as a twin boundary fault; (b) an intrinsic fault; (c) an extrinsic fault; and for lack of established names, (d) a super-extrinsic fault, and (e) a hyper-extrinsic fault. The structure (f) is the double-hexagonal-close-packed *(dhcp)* structure. For the stacking faults, the number of layers on which the potentials were allowed two relax is the number of layers pictured less two.

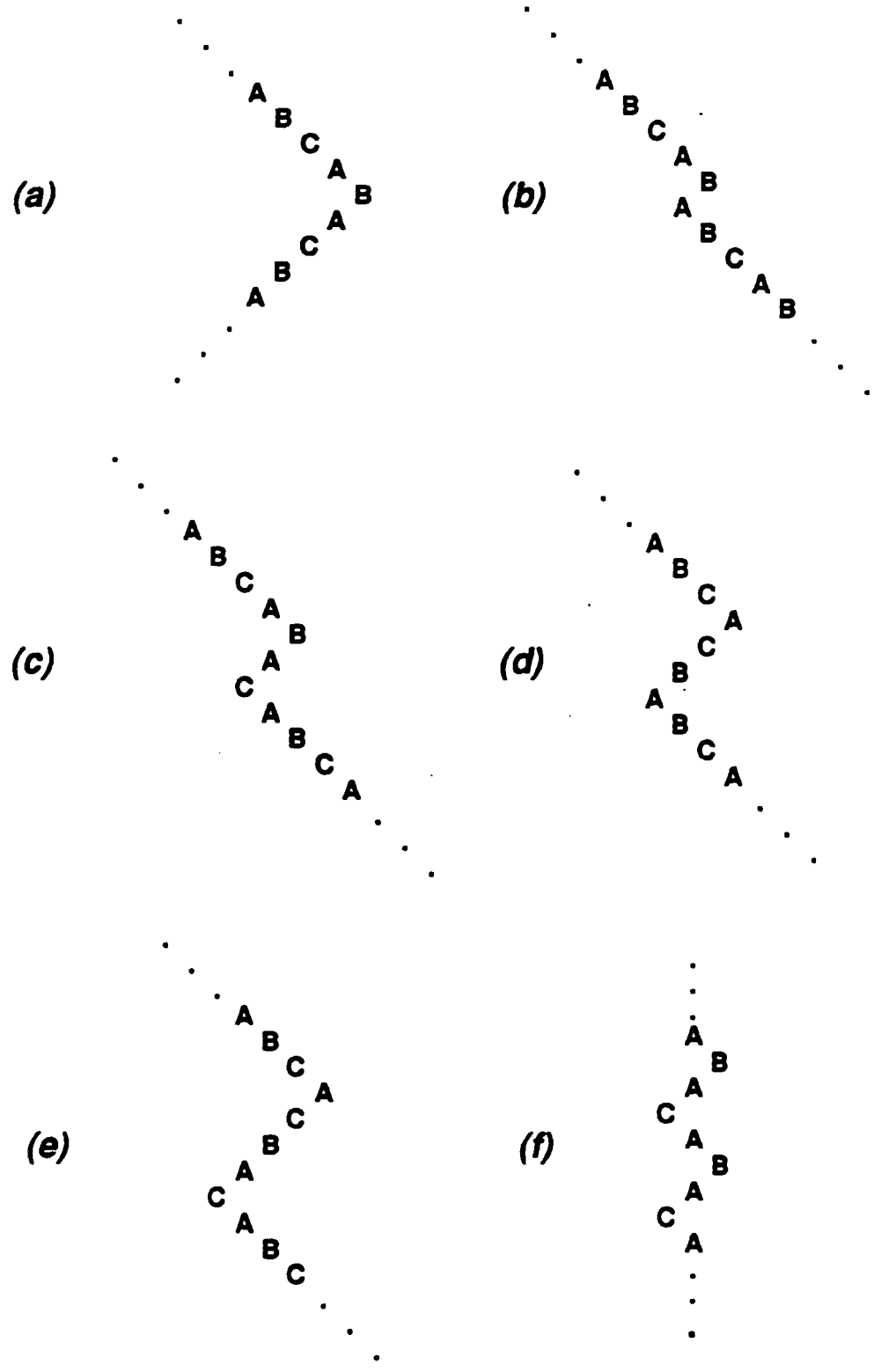
(a)
A B C A B A C B A
(b)
A B C A B A B C A B
(c)
A B C A B A C A B C A
(d)
A B C A C B A B C A
(e)
A B C A C B A C A B C
(f)
A B A C A B A C A

Figure 4.5

Figure 4.6 (a) The two-dimensional Brillouin zone used for the calculation. (b) The projection points of the three-dimensional *fcc* Brillouin zone onto the two-dimensional zone used in the calculations. The points are labelled by their corresponding three-dimensional labels. The Γ and L points of the three-dimensional zone project onto the center of the two-dimensional zone. The remaining L-points and the X-points project onto $\overline{M}$. The K-points project onto the nonsymmetry points indicated in the figure.

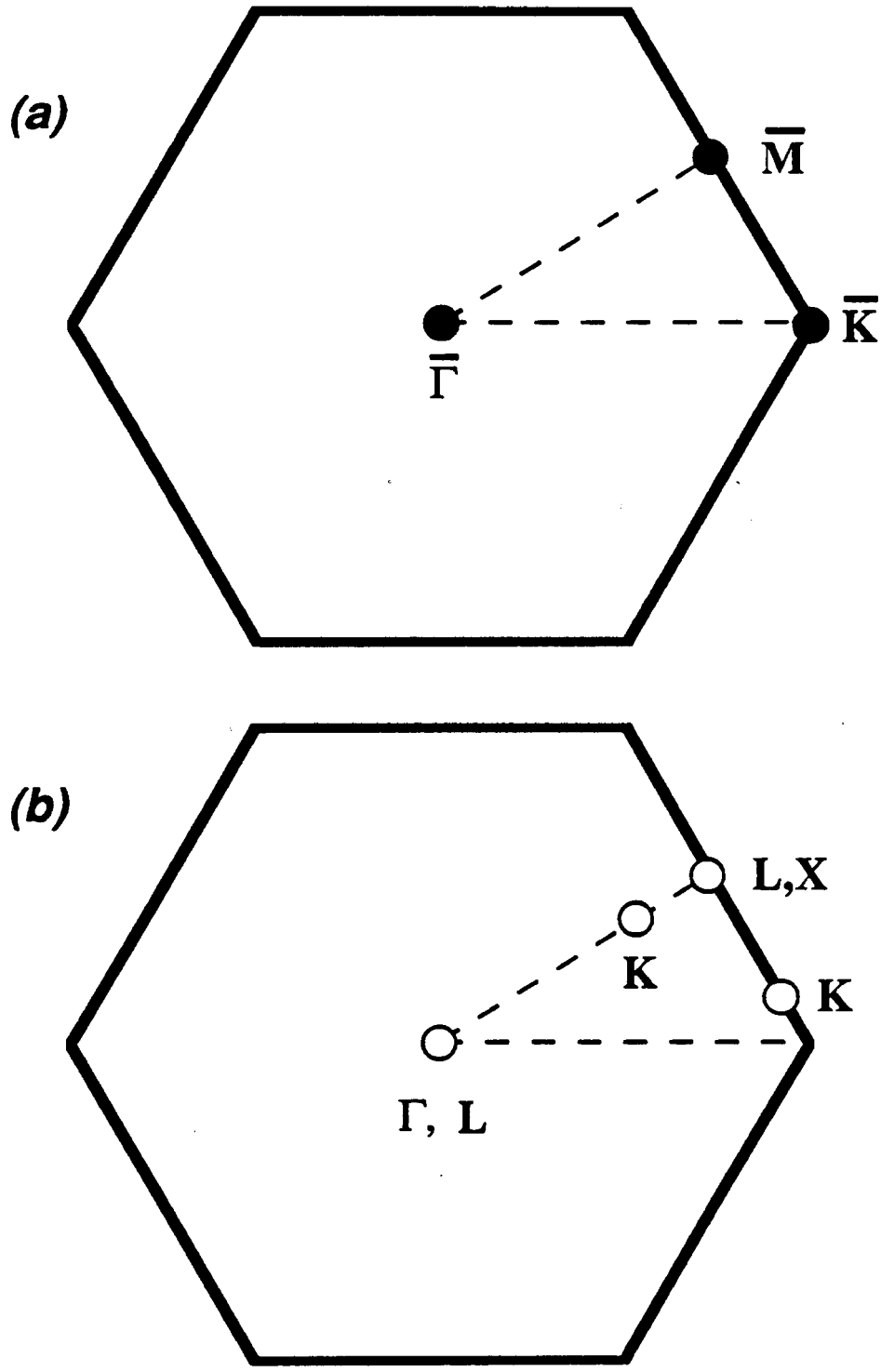

Figure 4.6

Figure 4.7 The projection of the three-dimensional band structure of *fcc* nickel onto the two-dimensional Brillouin zone of figure 4.6. The shaded regions are those for which three-dimensional band states exist, the white regions represent gaps in the spectrum. It is in the white regions that one looks for localized states. From the figure it is clear that there is a possibility of finding states localized in teh vicinities of $\overline{K}$ and $\overline{\Gamma}$, but not about $\overline{M}$. The projected band structures for both spins are similar, suggesting that in an approximate sense, the magnetism can be thought of in terms of a Stoner shift.

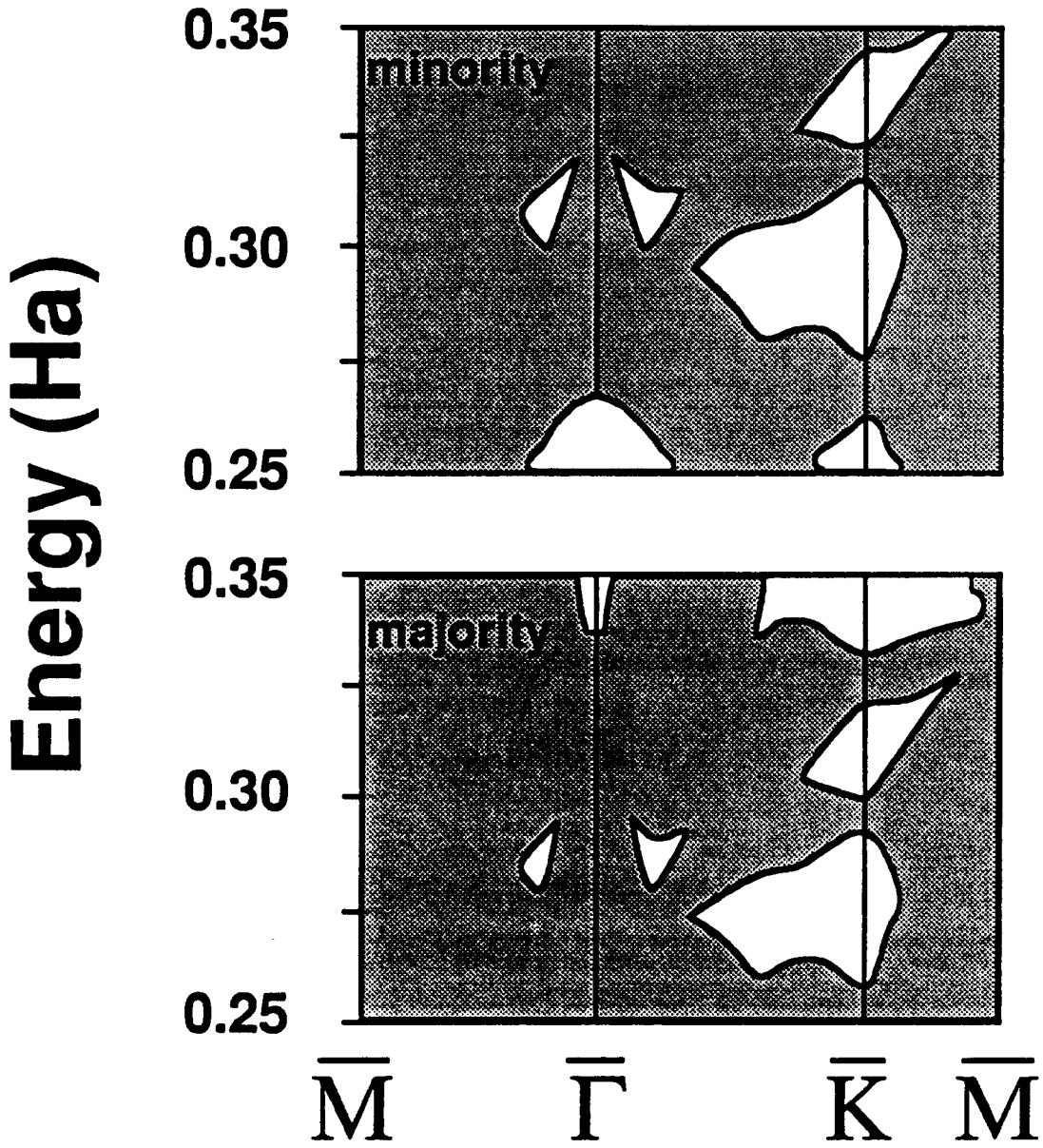

Figure 4.7

Figure 4.8 The **k**-resolved layer projected MTDOS for the $\bar{\Gamma}$-point of the twin boundary fault (in arbitrary units). The solid lines are the majority-spin states and the dashed lines are the minority-spin states. The layers are labelled as in figure 4.5. The dotted vertical line represents the Fermi level of *fcc* nickel. There is a resonant state, in bothe spin polarizations, which splits off from the upper *d*-band (the majority-spin localized states are indicated by the arrows). The energies of the resonances are given in table 4.3.

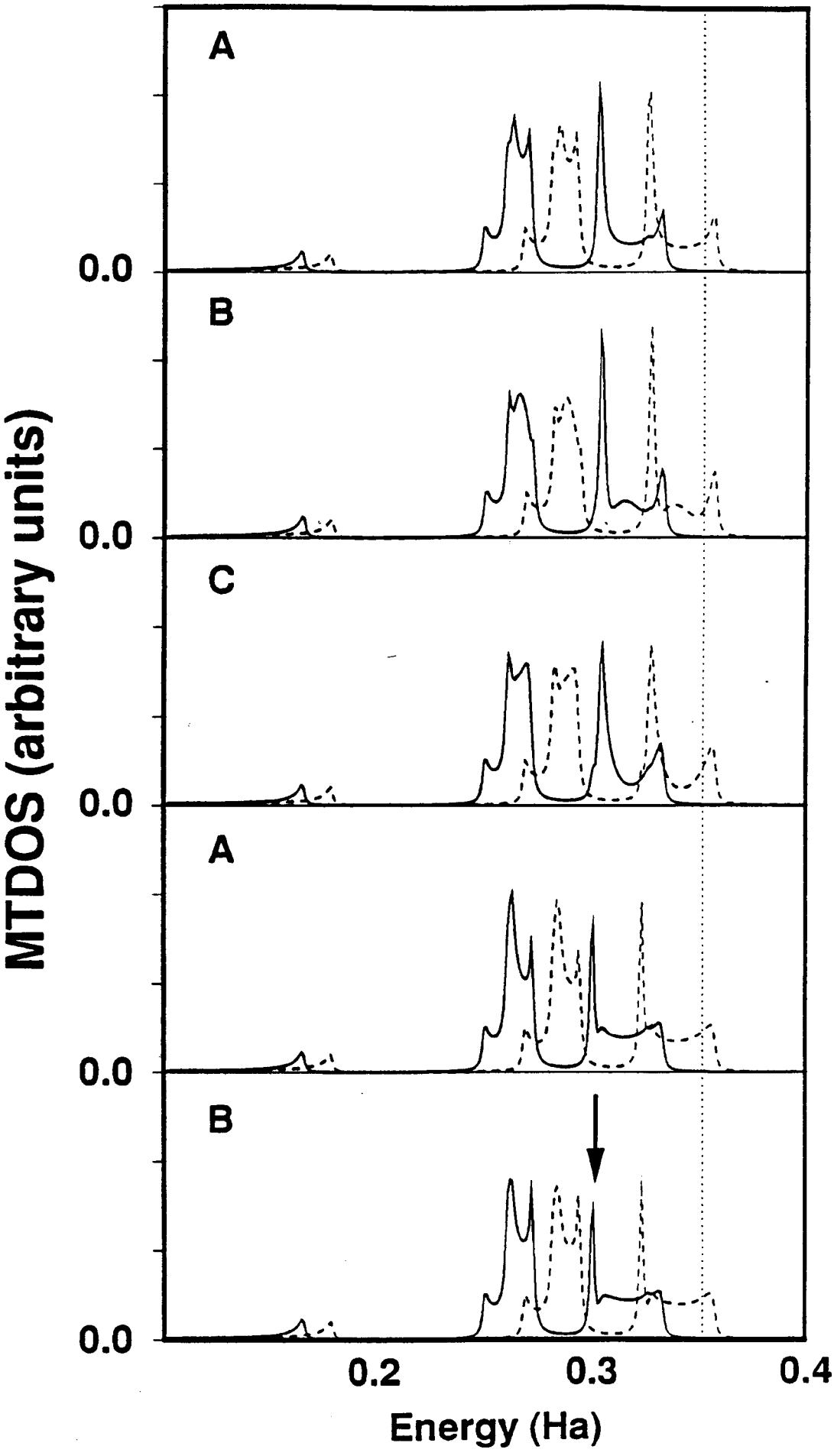

Figure 4.8

Figure 4.9 The **k**-resolved layer projected MTDOS for the $\overline{M}$-point of the twin boundary fault (in arbitrary units). The solid lines are the majority-spin states and the dashed lines are the minority-spin states. The layers are labelled as in figure 4.5. The dotted vertical line represents the Fermi level of *fcc* nickel. There are three localized states for each spin polarization (the majority-spin localized states are indicated by arrows). The energies of the states are given in table 4.3.

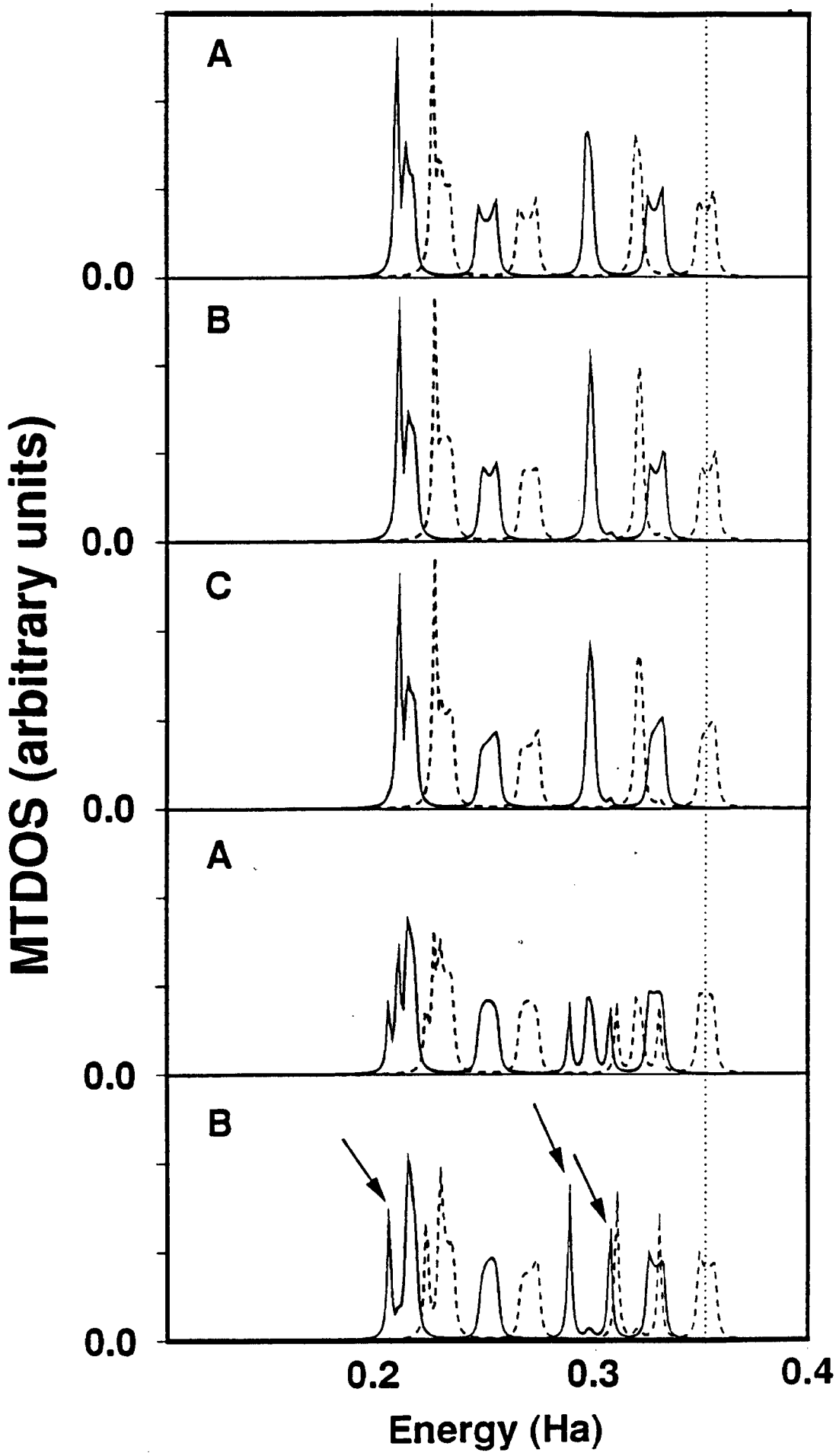

Figure 4.9

Figure 4.10 The **k**-resolved layer projected MTDOS for the $\overline{\Gamma}$-point of the extrinsic fault (in arbitrary units). The solid lines are the majority-spin states and the dashed lines are the minority-spin states. The layers are labelled as in figure 4.5. The dotted vertical line represents the Fermi level of *fcc* nickel. There are resonant states in both spin polarizations which split off from the upper d-band and (the majority-spin localized states are indicated by arrows). The energies of the resonances are given in table 4.3. There is also a noticeable shift of minority-spin states from above the Fermi level to below, thus contributing to the decrease in spin polarization of the central layer (lowest panel) of this fault.

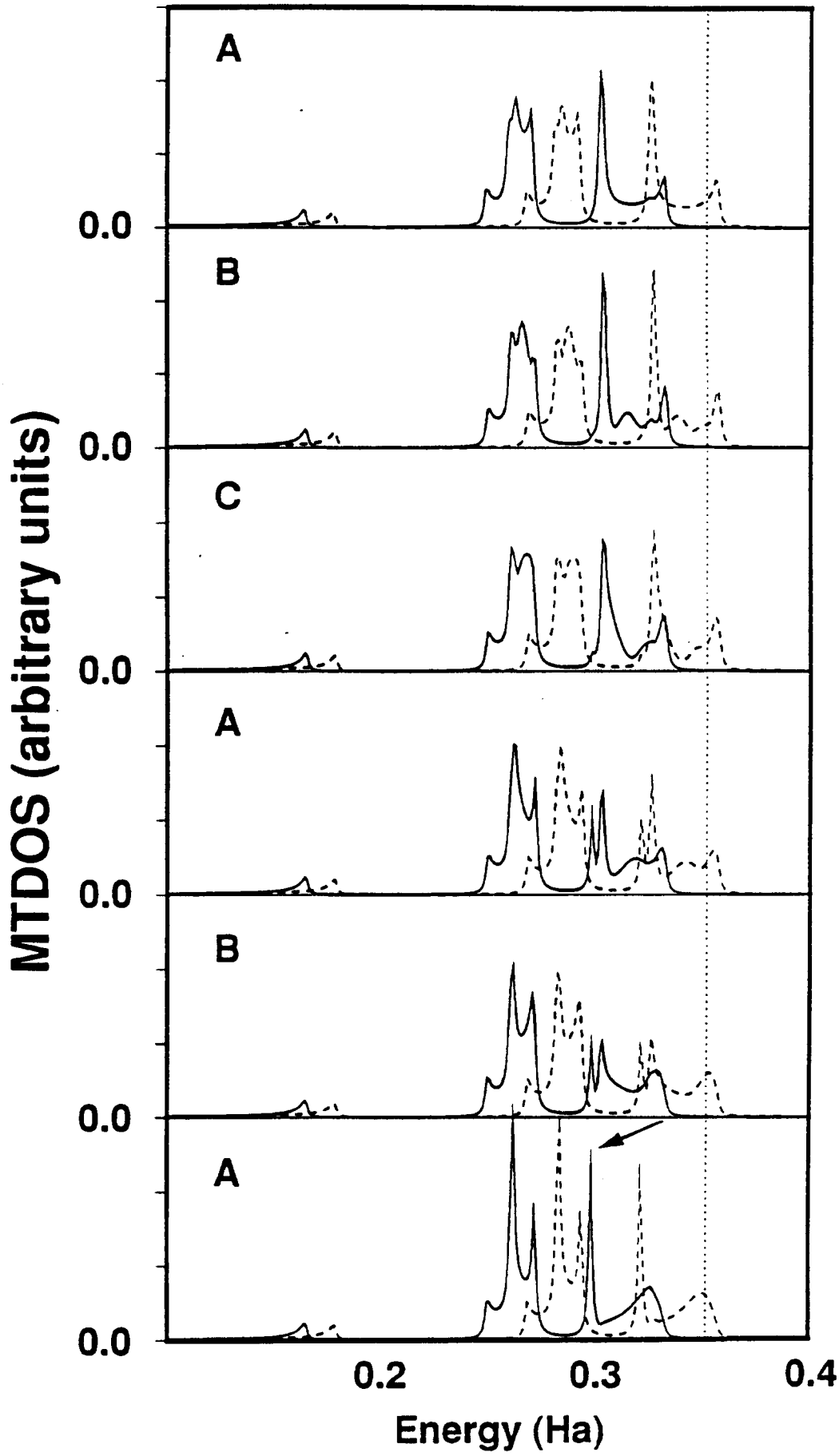
A
B
C
A
B
A
0.0
0.0
0.0
0.0
0.0
0.0
MTDOS (arbitrary units)
0.2
0.3
0.4
Energy (Ha)

Figure 4.10

Figure 4.11 The **k**-resolved layer projected MTDOS for the $\bar{K}$-point of the extrinsic fault (in arbitrary units). The layers are labelled as in figure 4.5. The solid lines are the majority-spin states and the dashed lines are the minority-spin states. The dotted vertical line represents the Fermi level of *fcc* nickel. There are three localized states present in each spin polarization (the majority-spin states are indicated by arrows). The energies of the states are given in table 4.3.

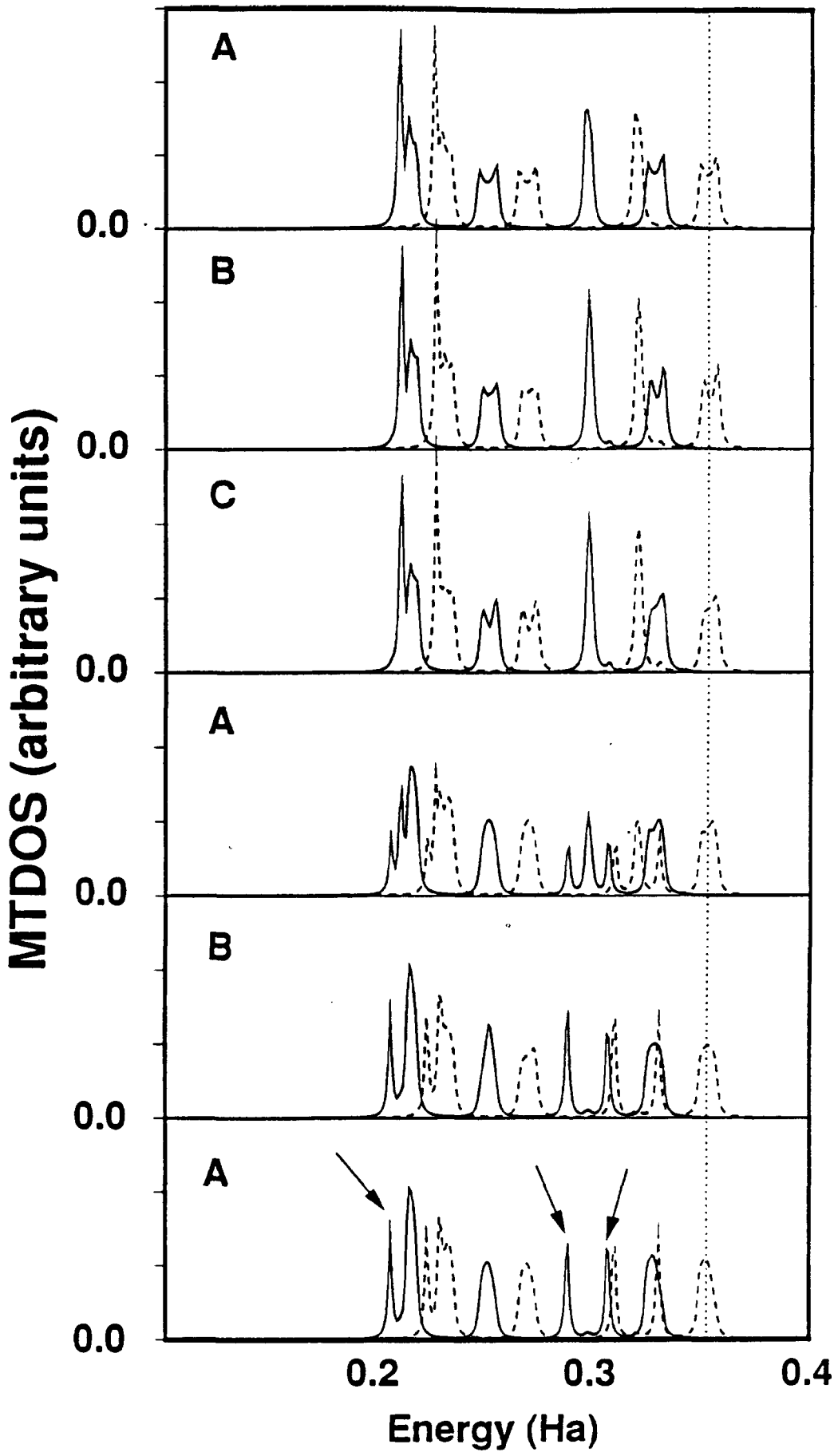
A
B
C
A
B
A
0.0
0.0
0.0
0.0
0.0
0.0
MTDOS (arbitrary units)
0.2
0.3
0.4
Energy (Ha)

Figure 4.11

Figure 4.12 The **k**-resolved layer projected MTDOS for the $\overline{K}$-point of the hyper-extrinsic fault (in arbitrary units). The solid lines are the majority-spin states and the dashed lines are the minority-spin states. The layers are labelled as in figure 4.5. The dotted vertical line represents the Fermi level of *fcc* nickel. There are four localized states for each spin polarization (the majority-spin localized states are indicated by arrows). The energies of the states are given in table 4.3. The strongly localized states at lower energies do not mix with their counterparts on the other P-layer of the fault. In contrast, the two localized states at higher energy result from the mixing between localized states centered on different P-layers. This mixing results in a symmetric state and an antisymmetric peak. The spectral strength of the peak from the antisymmetric state goes to zero on the central layer of the fault.

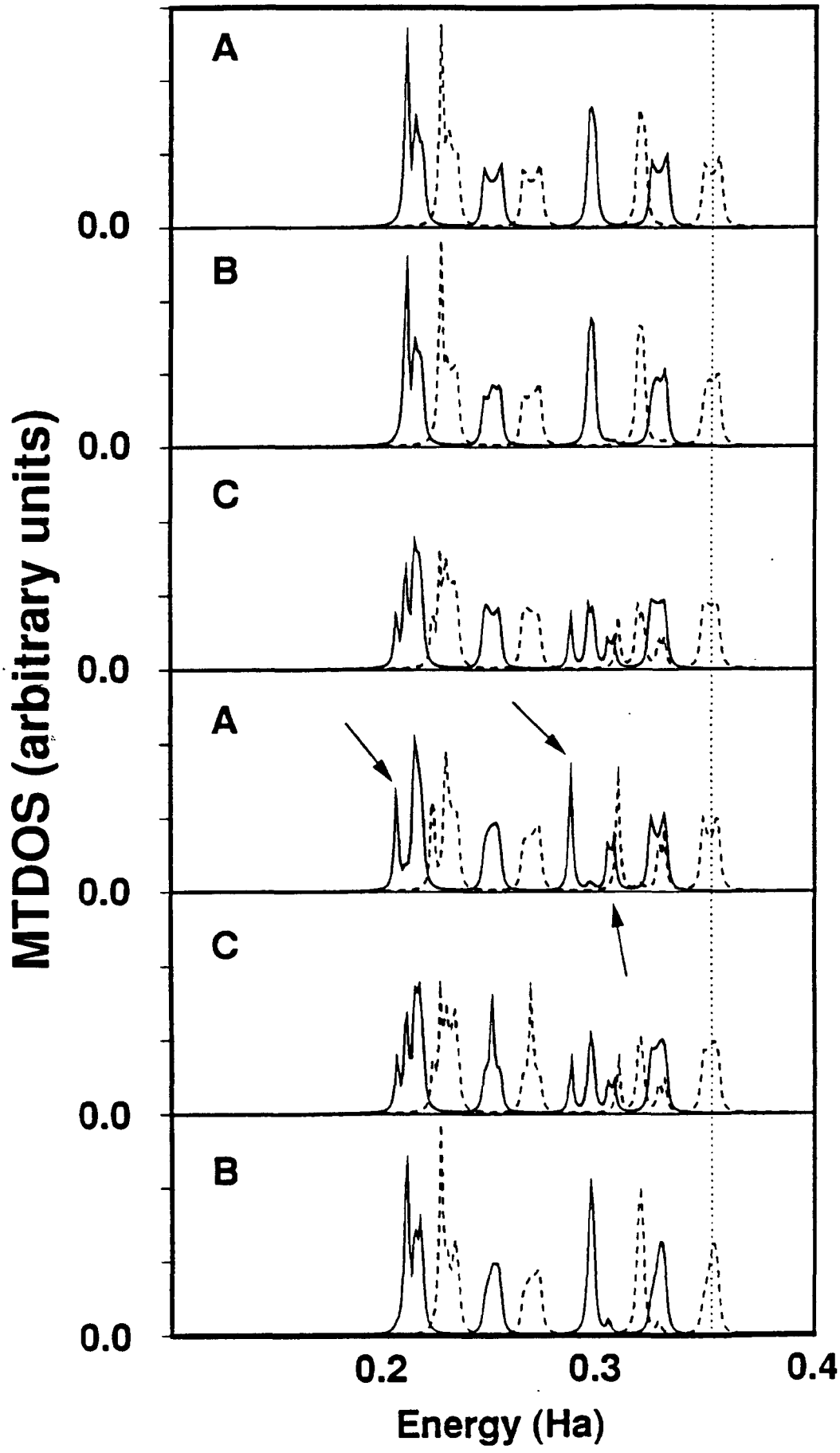
A
B
C
A
C
B
0.0
0.0
0.0
0.0
0.0
0.0
MTDOS (arbitrary units)
0.2
0.3
0.4
Energy (Ha)

Figure 4.12

Figure 4.13 A comparison of the **k**-resolved MTDOS for the *fcc* and *hcp* structures (in arbitrary units). The dashed lines are the *fcc* results, and the solid lines are the result for the *hcp* structure. The upper panel in each frame is the minority-spin, the lower the majority-spin. There are two features of the $\overline{\Gamma}$-point MTDOS pictured in panel (a) which are relevant to the the current arguments. First, the minority spin peak at highest energy lies above the Fermi level in the *fcc* case, and lies below it in the *hcp* result. The second feature is that the bandwidth of the states nearest the Fermi level is broadened in the *hcp* structure relative to its width in the *fcc* system. The MTDOS at $\overline{M}$ [panel (b)] also display important differences. The most obvious is the presence of a peak in the majority-spin states of bulk *hcp* nickel which lies completely above the Fermi level, and is not present in the *fcc* MTDOS. Also, a gap in the majority-spin MTDOS has opened at the Fermi level. It is also clear from this panel that the *hcp* system is no longer adequately described by a simple Stoner shift. The majority-spin peak above the Fermi level at $\overline{M}$ and the minority spin states at $\overline{\Gamma}$ which move below the Fermi level contribute to the decrease in spin polarization.

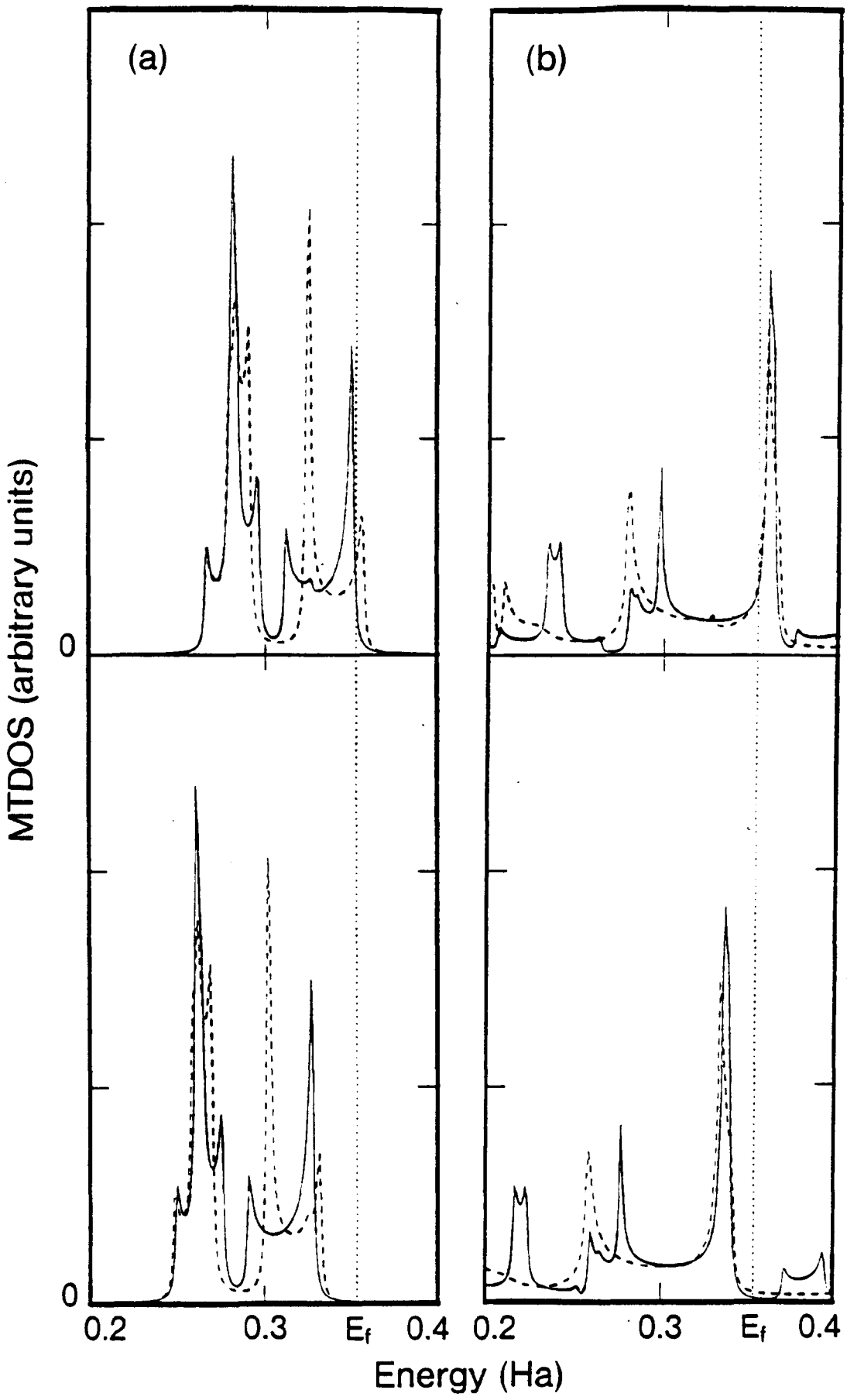

Figure 4.13

Figure 4.14 The band structure of *fcc* nickel plotted along a line parallel to the [111] direction passing through $\overline{M}$. The majority-spin bands are the solid line and the minority-spin bands are given by the dashed line. The line along which this band structure is calculated passes through the X-point and the L-point of the three-dimensional Brillouin zone. The source of the minority-spin hole-pocket at X is clearly visible. (The second, experimentally unobserved, hole-pocket at X is also present.) There is a minority-spin d-like band which lies almost completely above the Fermi level, and a majority-spin s-like band which crosses the Fermi level.

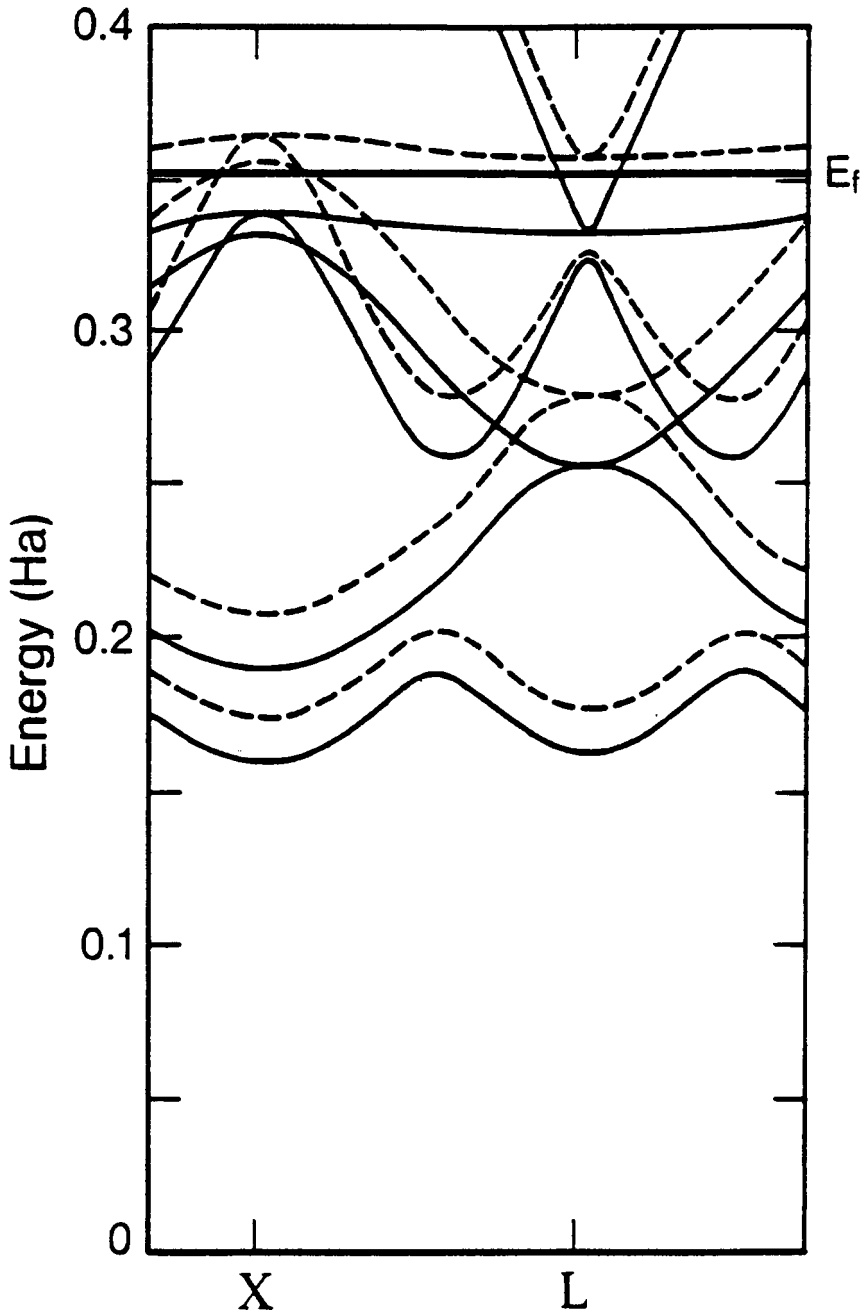

Figure 4.14

Figure 4.15 A plot of the band structure of hypothetical *hcp* nickel along the line L-M-L, which is the direction equivalent to that plotted in figure 4.14. The solid lines are the majority-spin bands, and the dashed lines are the minority-spin bands. The states responsible for the peak in MTDOS of the majority spin are clearly visible. There is one majority-spin band which lies completely above the Fermi level (in the pictured range of reciprocal space).

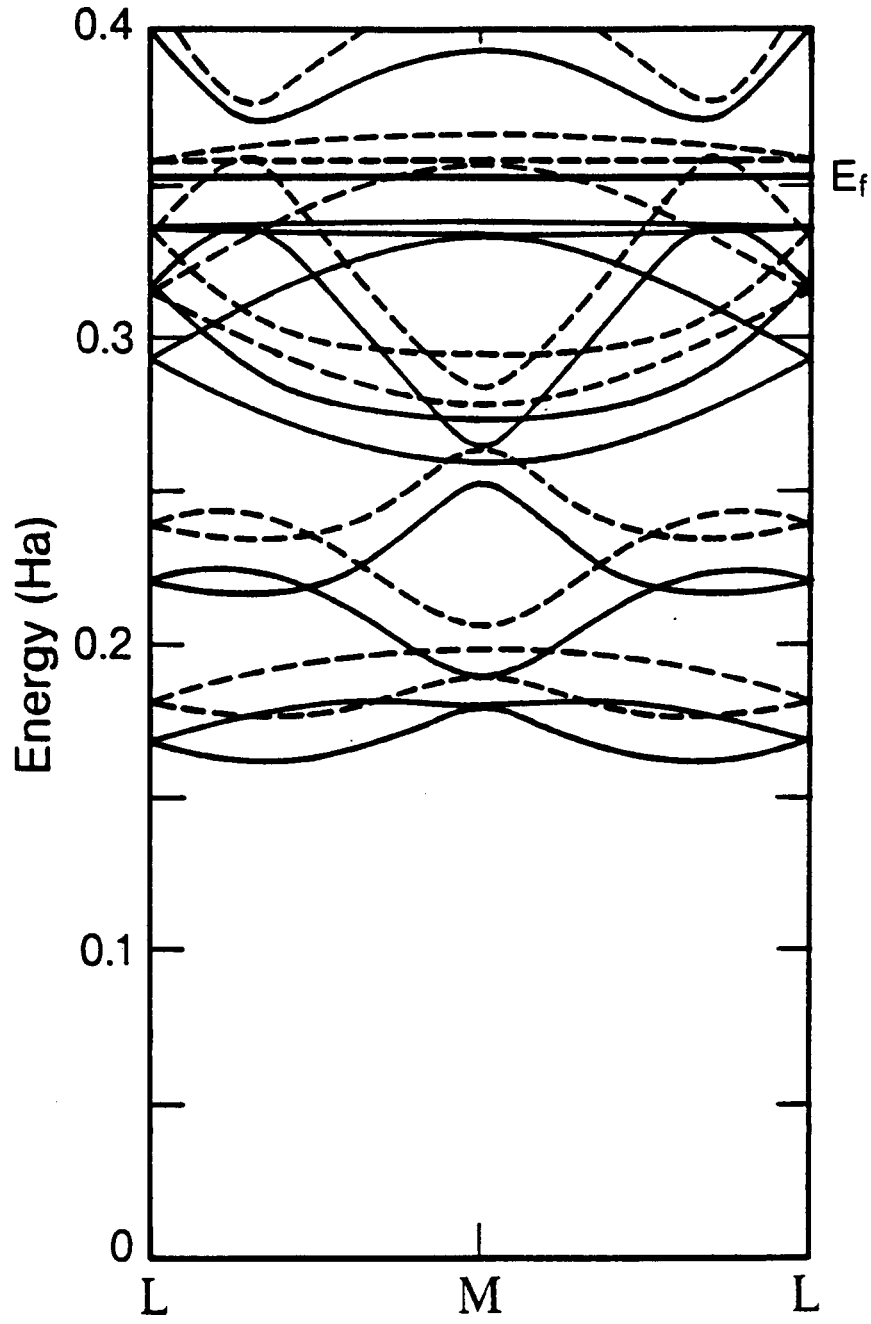

Figure 4.15

Figure 4.16 The **k**-resolved MTDOS for the $\overline{M}$-point of the extrinsic fault, labelled as in figure 4.5. The solid lines represent the majority-spin states and the dashed lines represent the minority-spin states. The dotted vertical line is the Fermi level. The most interesting feature of this plot is the "bump" in the majority-spin MTDOS which appears above the Fermi level on the layer in which the spin polarization is most reduced (i.e. the central layer of the fault).

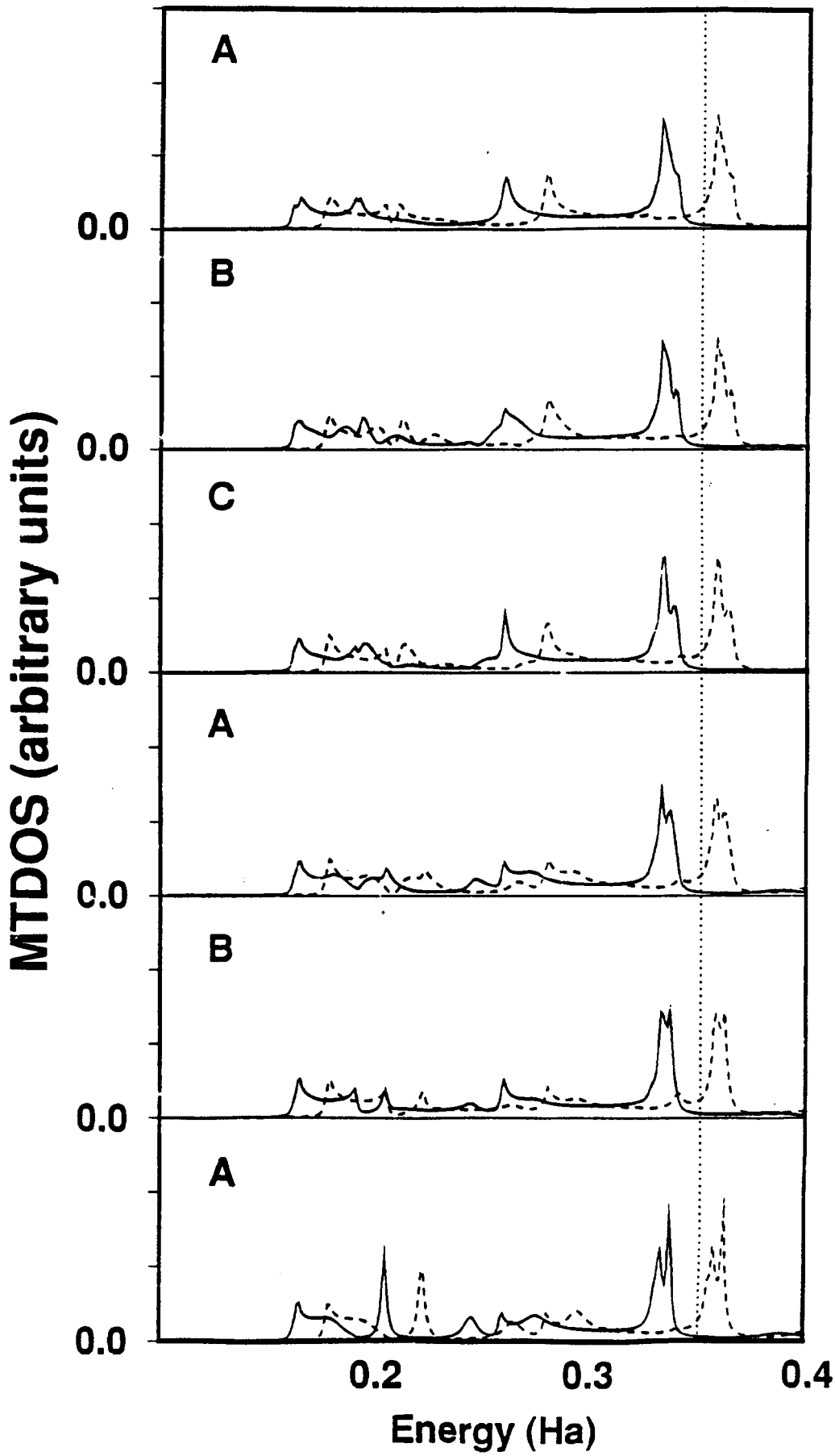
A
B
C
A
B
A
0.0
0.0
0.0
0.0
0.0
0.0
MTDOS (arbitrary units)
0.2
0.3
0.4
Energy (Ha)

Figure 4.16

Figure 4.17 The stacking sequences for the stacking faults based on hypothetical *unstable hcp nickel.* (These defects would form *spontaneously.)* The potentials on all of the layers pictured were allowed to relax. The interesting feature of these structures is that they both contain layers (labelled C) which do not have neighbors at any distance along the [111] direction. This isolation should lead to a narrowing in the widths of the states on layers C, as well as an increase in spin polarization. which is the calculated result.

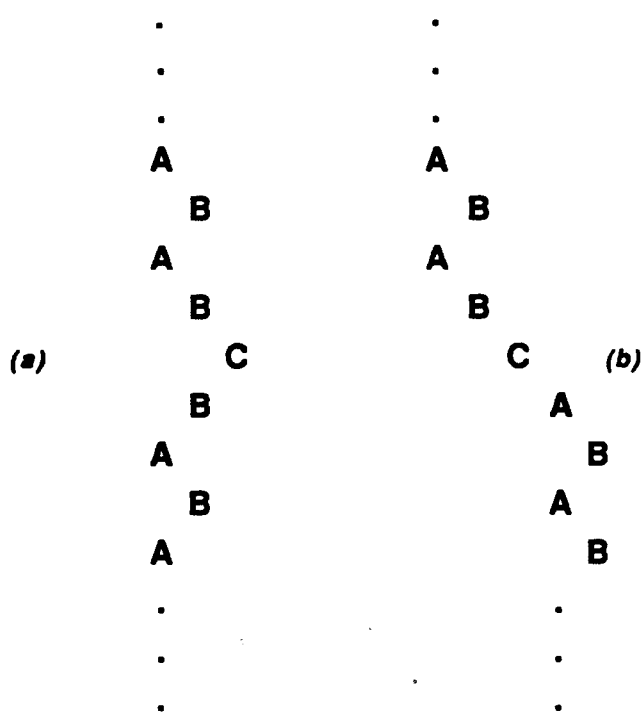

Figure 4.17

Figure 4.18 The **k**-resolved layer projected MTDOS for the stacking sequence pictured in figure 4.17(b) plotted at $\overline{\Gamma}$. The solid lines represent the majority-spin states and the dashed lines represent the minority-spin states. The dotted vertical line is the Fermi level of *hcp* nickel. The most striking feature of this plot is the minority-spin localized state which splits off from the top of the *d*-like band and moves above the Fermi level. In addition, the apparent widths of the states is significantly decreased on the isolated layer. This is consistent with the expected behavior; the muffin-tin spin polarization on the central layer is increased by eight percent over the bulk *hcp* value of 0.583 μ_B to 0.635 μ_B.

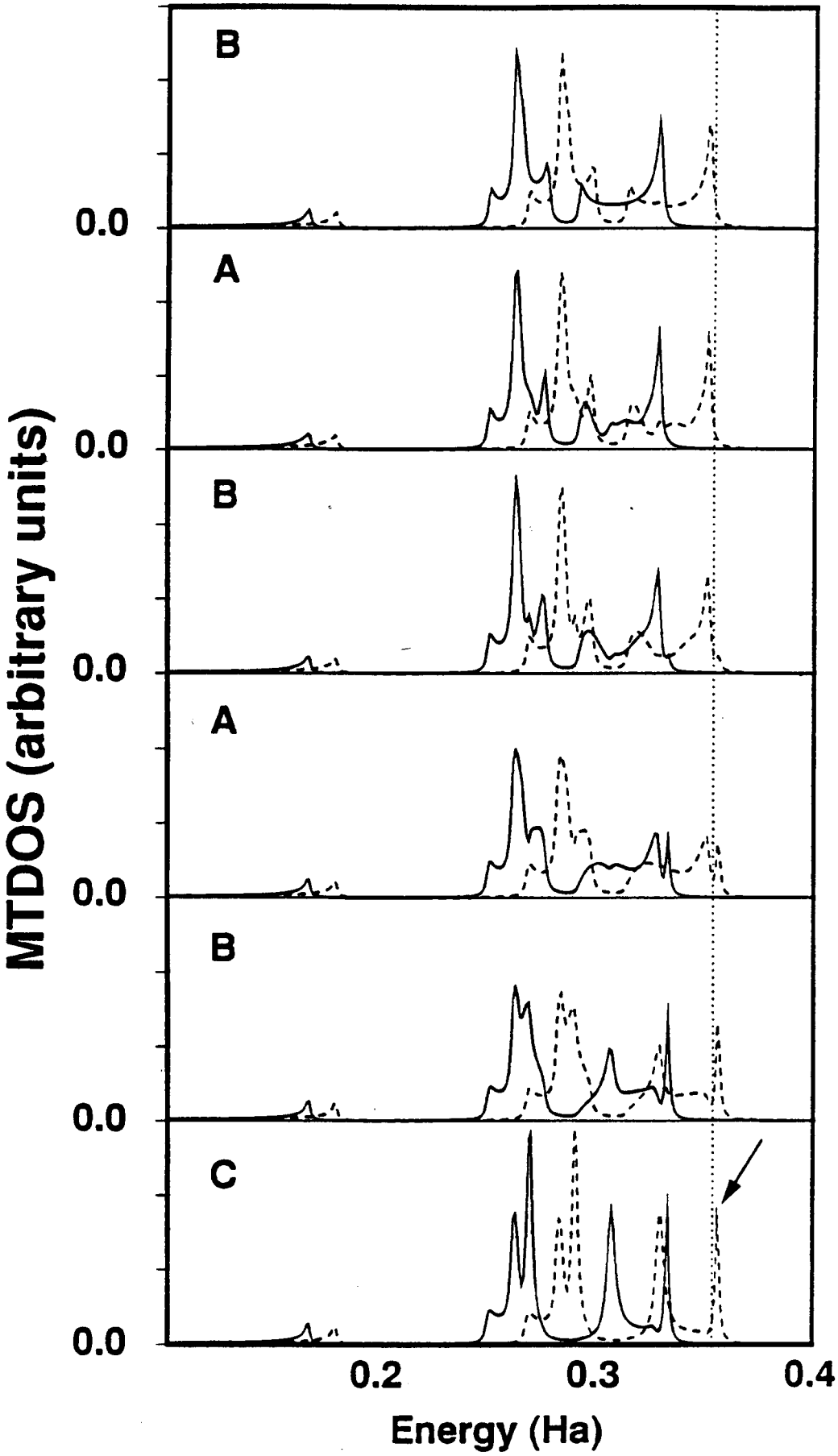
B
A
B
A
B
C
0.0
0.0
0.0
0.0
0.0
0.0
MTDOS (arbitrary units)
0.2
0.3
0.4
Energy (Ha)

Figure 4.18

Figure 4.19 The **k**-resolved layer projected MTDOS for the stacking sequence pictured in figure 4.17(b) plotted at $\overline{M}$. The solid lines represent the majority-spin states and the dashed lines represent the minority-spin states. The dotted vertical line is the Fermi level of *hcp* nickel. The most striking feature of this plot is that the majority-spin peak above the Fermi level completely disappears on the central layer of the stacking defect.

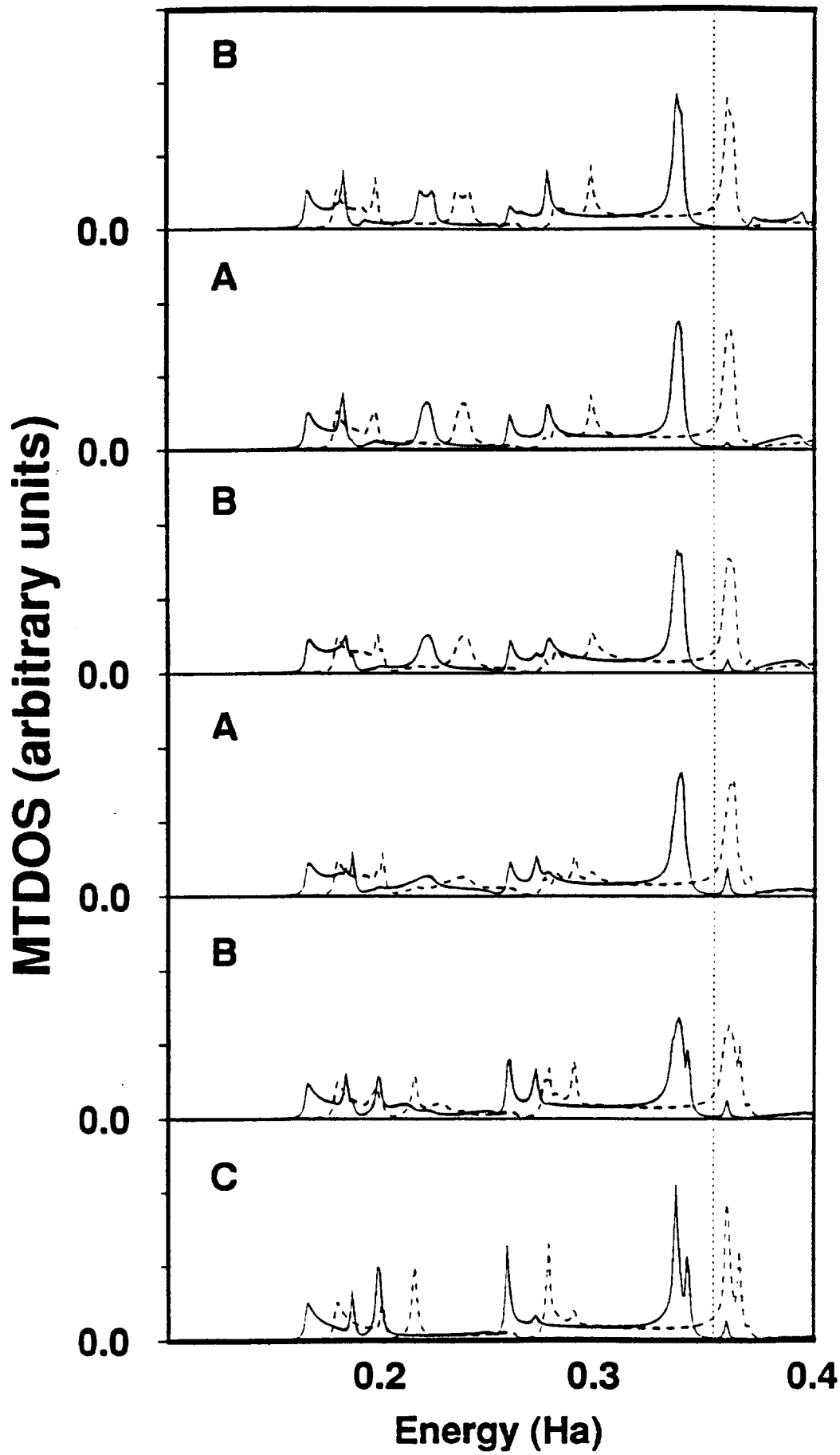
B
A
B
A
B
C
0.0
0.0
0.0
0.0
0.0
0.0
MTDOS (arbitrary units)
0.2
0.3
0.4
Energy (Ha)

Figure 4.19

Figure 4.20 The band structure of cobalt taken from Papaconstantopolous' book, plotted along three directions. While the exact details of the changes in spin polarization of nickel reported here depend on the specific properties of the band structure of nickel, there is reason to believe that similar effects will occur in cobalt. The band structure along Γ to A of cobalt is very similar to that of nickel plotted along Γ to L, except that the Fermi level crosses near the bottom of the minority-spin band in cobalt, not the top as in nickel. The band structure of cobalt plotted along the M to L direction is very similar to that of *hcp* nickel plotted along this same direction. It is not clear how stacking faults will affect the spin polarization of this system, but if the result of a fault is narrow the local "bandwidth" of states along the Γ to A direction and to shift the average energy of the states up, which are the effects observed in the nickel calculation, the change in spin polarization could be similar in magnitude to that calculated for nickel. This change, however, would most likely represent a small percentage change in spin polarization and would be difficult to detect experimentally.

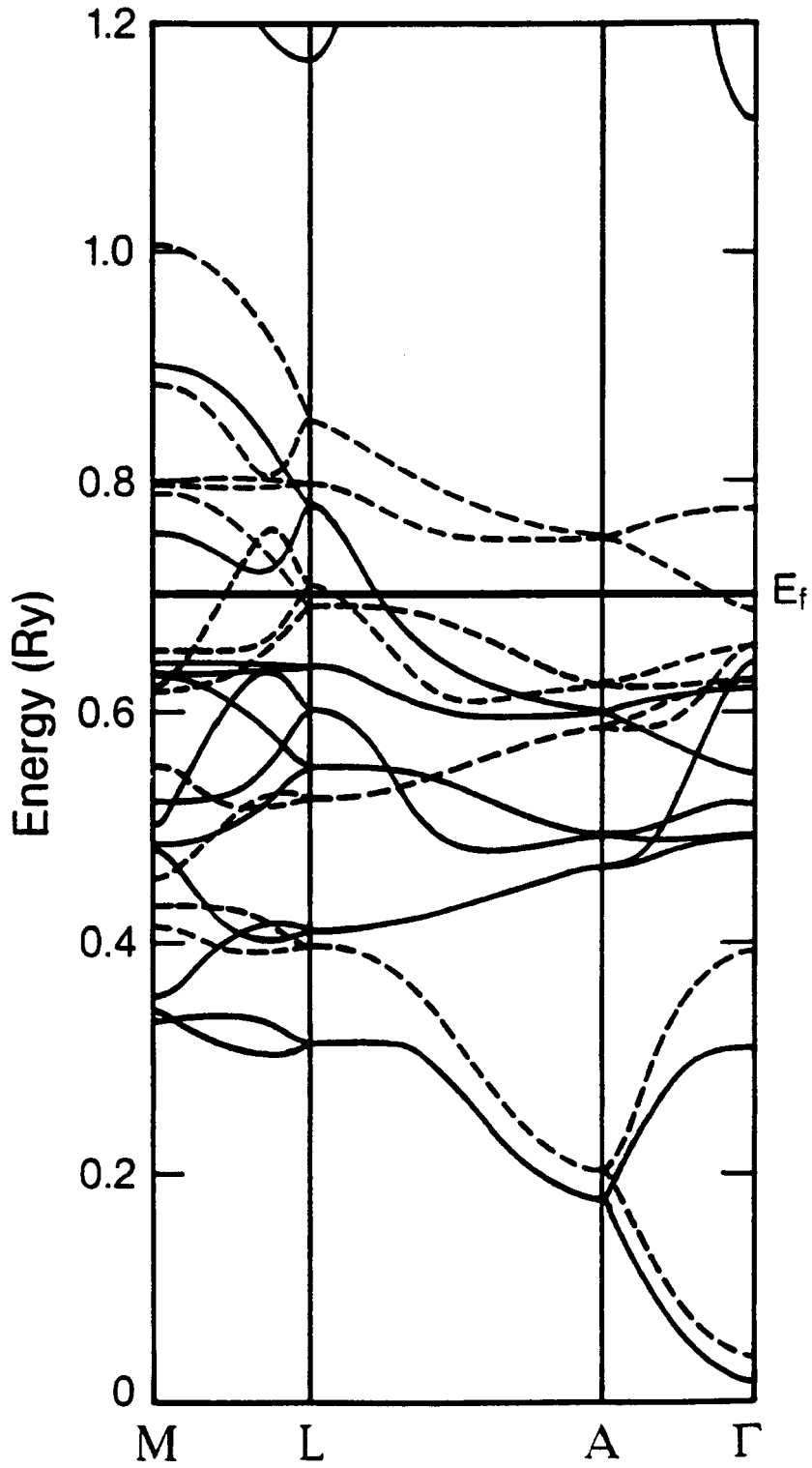

Figure 4.20

Figure 4.21 A comparison of the spin polarizations calculated with the simple fitting procedure outlined in the text and the LKKR values. The lines are guides for the eye. The fitting parameters are those in table 4.6. The plot labelled (a) is for the twin boundary fault, (b) is for the intrinsic fault, and (c) is for the extrinsic fault. The abcissae are labelled as in figure 4.5. In all cases the trends in spin polarization are adequately predicted by this simple fitting method.

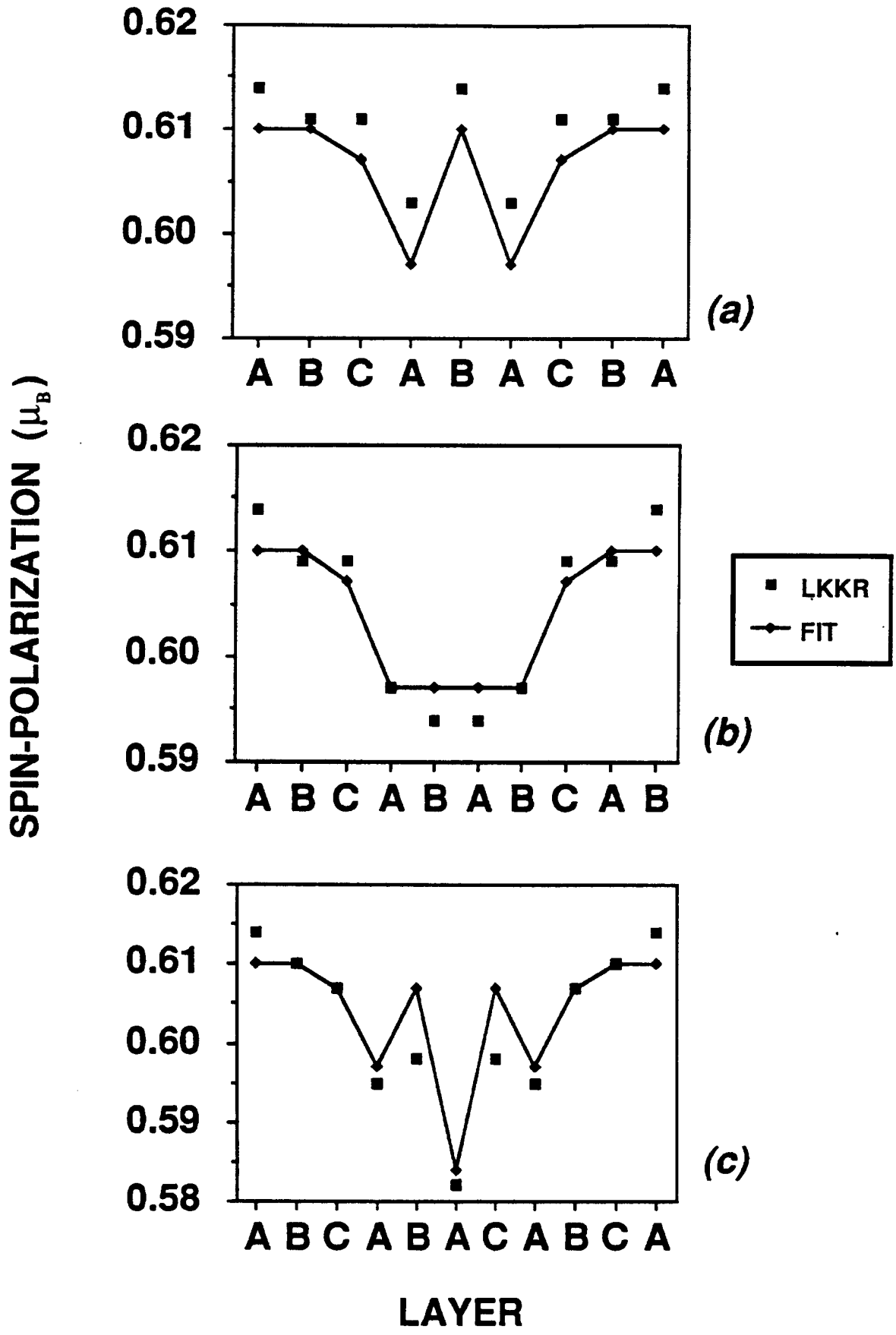
SPIN-POLARIZATION (μ_B)
0.62
0.61
0.60
0.59
A B C A B A C B A
(a)
0.62
0.61
0.60
0.59
A B C A B A B C A B
(b)
LKKR
FIT
0.62
0.61
0.60
0.59
0.58
A B C A B A C A B C A
(c)
LAYER

Figure 4.21

Figure 4.22 A comparison of the spin polarizations calculated with the simple fitting procedure outlined in the text and the LKKR values. The lines are guides for the eye. The fitting parameters are those of table 4.6. The plot labelled (e) is for the super-extrinsic fault and (f) is for the hyper-extrinsic fault. The abcissae are labelled as in figure 4.5. In all cases the trends in spin polarization are adequately predicted by this simple fitting method.

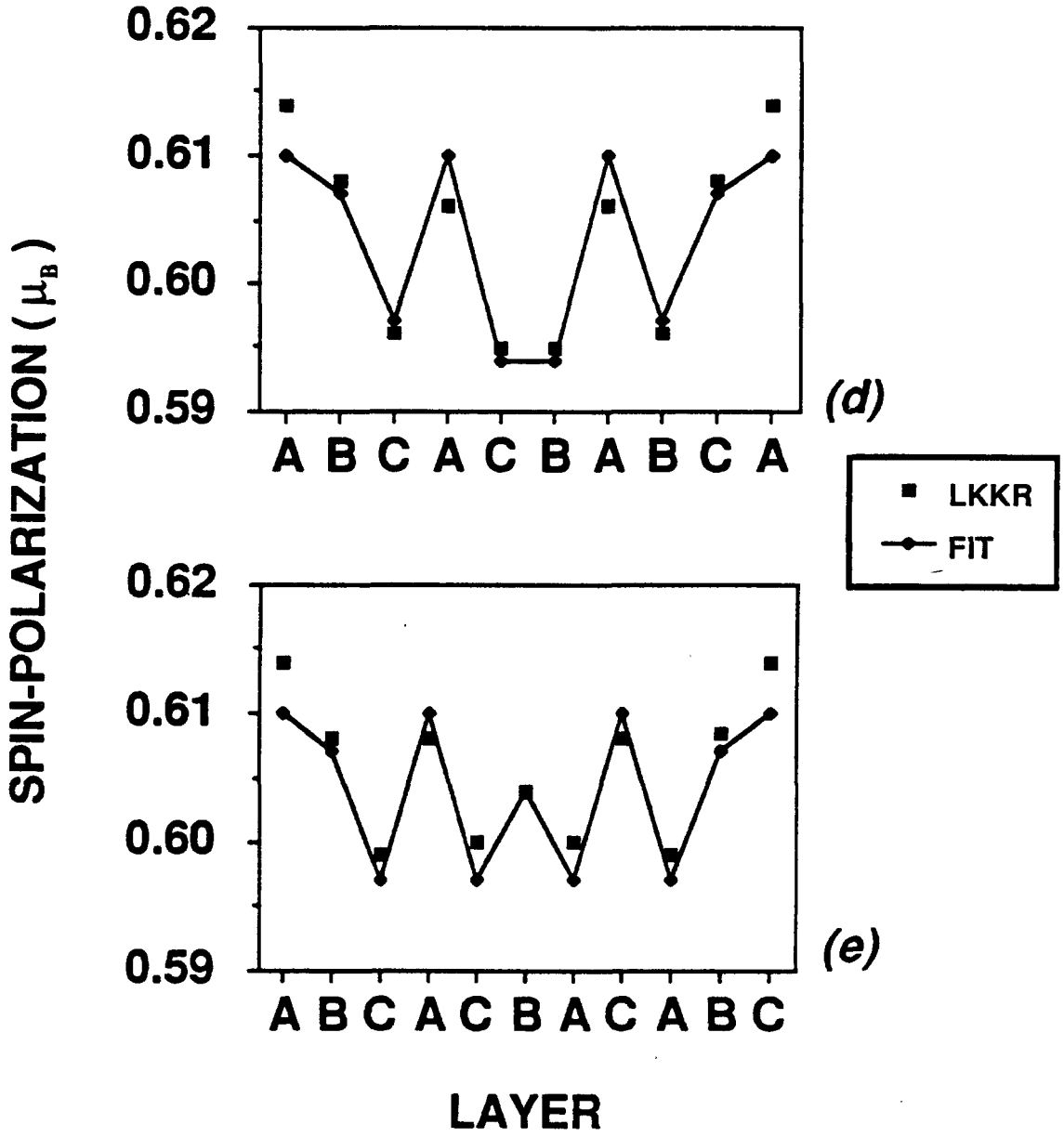
0.62
0.61
0.60
0.59
A B C A C B A B C A
(d)
LKKR
FIT
0.62
0.61
0.60
0.59
A B C A C B A C A B C
(e)
SPIN-POLARIZATION (μ_B)
LAYER

Figure 4.22